論文 / 著書情報
Article / Book Information

題目(和文)	時分割X線画像検出器マイクロストリップガスチェンバーの研究
Title(English)	Study of microstrip gas chamber as a time-resolved x-ray area detector
著者(和文)	越智敦彦
Author(English)	Atsuhiko Ochi
出典(和文)	学位:博士(理学), 学位授与機関:東京工業大学, 報告番号:甲第3649号, 授与年月日:1998年3月26日, 学位の種別:課程博士, 審査員:
Citation(English)	Degree:Doctor (Science), Conferring organization: Tokyo Institute of Technology, Report number:甲第3649号, Conferred date:1998/3/26, Degree Type:Course doctor, Examiner:
学位種別(和文)	博士論文
Type(English)	Doctoral Thesis

Study of MicroStrip Gas Chamber as a Time-Resolved X-ray Area Detector

Atsuhiko Ochi

December 26, 1997
Revised version, March 3, 1998

Doctoral thesis

Abstract

A two-dimensional MicroStrip Gas Chamber (MSGC) with a 10cm square detective area has been developed. The fine position resolution of $\sim 100\mu$m using digital readout and the excellent capability for high counting rate of up to 2×10^7cps have been attained. The breakdown problem has been overcome by the cathode passivation technique, and the gain variation problem has been solved by tuning the operation voltage and the substrate thickness ($\sim 20\mu$m), which were determined through simulation. A fast data acquisition system has also been developed specifically for MSGC readout to obtain time-resolved X-ray images. The signals of 1024 channels are encoded to position information of 20 bits using a CPLD (Complex Programmable Logic Array). The signals can be processed every 100ns, and a data taking rate of 3.2 Mcps has been attained for real X-ray event taking. In order to study the performance of the time-resolved property, changes of the X-ray diffraction pattern were measured using the photo excitation effect of metal complexes. The diffraction peek movement of 0.02 degree has been observed with the time constant of 2 seconds for the first time in the world. An X-ray rotation photograph including the rotation angle information was also taken, which makes it possible to analyze the crystal structure in a very short (a few minutes) time. An X-ray imaging detector with micro second timing resolution is now available for the first time in the world, opening versatile fields of applications.

Contents

Chapter 1

Introduction

Some of major breakthroughes in science have been brought by inventions of new devices or new methods of observation. Detectors with the gas-amplification process are widely used for detections of γ(X)-rays, charged particles and neutrons, and its technology appears to have been established.

However a new idea on gas detector was recently proposed in 1988[1]. MicroStrip Gas Chamber (MSGC) has very narrowly spaced conductor strips which are printed on a substrate instead of wires. The spacing between the strips can be much smaller than the smallest wire spacing in Multi-Wire Proportional Chamber (MWPC), and the strong field which is necessary for a gas amplification is generated between neighboring strips. Excellent performances such as a fine position resolution of $30 \sim 100\mu$m and a weak space charge effect which is ~ 1000 times superior to that of wire chambers can be achieved. Therefore MSGC has been studied intensively in lots of fields.

One of the most expectant fields for MSGCs is the high-energy physics. The largest group developing MSGC is the GDD (Gas Detector Development) group in CERN. They plans to apply MSGC to the high luminosity colliding-beam experiments at LHC (Large Hadron Collider: at CERN) and HERA-B (B-factory in HERA: at DESY). Since a tremendous amount of charge particles will be produced at the colliding point in these experiments, wire chambers will not be operated well due to the space charge effect. MSGCs are expected to replace them as tracking devices. (See also [2, 3]). The Institute Laue-Langevin (ILL) group, who at first invented a MSGC, has developed MSGCs for a thermal neutron area detector. By filling a ^{3}He which has a large cross section for neutron, MSGC can detect thermal neutrons. In the field of the space research, the X-ray astronomy group in NASA

is developing a large area MSGC (30cm×30cm) for detecting X-rays up to $\sim$ 100keV [4]. Although MSGCs are expected to become a new type of an X-ray detector in the condensed matter physics, the biological and medical science, etc., no groups have succeeded in obtaining an X-ray image of good quality yet. The groups developing MSGCs are summarized in table 1.1.

Group	Area(mm^2)	Pitch	Readout	Application	Features	Ref.
ILL	127 × 127	1mm	charge div.	neutron	2-dimensional	[5]
CERN	100 × 100	0.2mm	direct	charged particle	1D	[6]
Pisa Univ.	100 × 250	0.2mm	direct	charged particle	1D	[7]
NIKHEF, IIHE	100 × 100	0.2mm	direct	charged particle	1D	[8]
T.I.T.	100 × 100	0.2mm	direct	X-ray	2D, fast DAQ	this thesis
NASA	300 × 300	2mm	direct	hard X-ray	2D, Xe gas	[4]
Yamagata Univ.	40 × 40	1mm	direct	X-ray	1D, polarimeter	[9]
Purdue Univ.	28 × 40	1mm	charge div.	neutron(?)	1D	[10]
Fermi Lab.	32 × 64	0.2mm	direct	charged particle	cathode readout	[11]

Table 1.1: Groups developing MSGCs in the world

In the early developments of MSGC, glass substrate with the thickness of 100 $\sim$ 500μm was used [12, 13, 14, 15]. However, glass substrate is weak against mechanical tension, which limits the area of MSGC to be less than $(10cm)^2$, and it seems difficult to make a thinner substrate than 100μm. MSGC made on 50μm thick polyimide foils had been developed [16], and MSGCs on various plastic supports had been studied by the CERN group [17]. Our group has studied MSGC on the poly-imide substrate since 1991, and MSGC having very thin substrate with thickness of 8μm was able to be operated [18, 19].

A two-dimensional MSGC can be realized using backstrips formed behind the substrate. Although a two-dimensional MSGC using back-electrodes (backstrips) was proposed at the beginning of development [1], small pulses obtained from the backstrips made difficult further developments. However Pisa University group succeeded in obtaining an X-ray transmission image using 1.8μm thick SiO_2 layer between the surface electrodes and the backstrips in 1cm square MSGC [20]. Our group also obtained an X-ray image by using 16μm thin poly-imide substrate [21]. Nevertheless, the application of MSGCs has hardly been realized yet because of unstable operation and of the necessity of huge amount of readout electronics for a large detection area.

There still remain some difficulties for a stable operation of MSGC. Since the electrodes of MSGCs are attached to the dielectric substrate, ions generated in an avalanche are

accumulated on the surface of the substrate between the strips, and cause the decrease of the gain. In general, in order to reduce this effect, the surface conductivity of the substrate has to be increased. The CERN GDD group has tested many materials of substrate with bulk resistivities of $10^9 \sim 10^{15}\Omega$cm [17, 22], and they concluded that the accumulation of charges can be avoided by decreasing the surface resistivity of the substrate down to $10^{12}\Omega$cm. Other methods such as ion implantation [23] and thin conductive layer deposit [19], were also applied to control the surface resistivities. We have developed another solution to avoid the charge accumulation problem by controlling the shape of the electric field around anodes. The results of this study are described in section 3.4 and in reference [21, 24].

Another critical problem is discharges between anodes and cathodes. Once a breakdown occurs, the strips would be critically damaged, and almost all the damaged strips are unusable again. It is considered that the extraction of electrons from the cathode edge and dusts on substrate are causes of breakdown. This effect is partially prevented by passivating the cathode edges [18, 19] or by employing a PMGC (Planar Micro-Gap Counter) design [25]. It was also reported that the main reason for the breakdown on MSGCs is due to streamers near the substrate [26]. In order to overcome this problem, the operation voltage between strips should be reduced. Recently the use of an intermediate gas-multiplier has been studied, which allows MSGC to be operated under low voltage while keeping the high gain. The Gas Electron Multiplier (GEM) has been developed in CERN [27] and a capillary plate has been used in our group [28] as the intermediate multiplier device. Originally the Yamagata Univ. group confirmed the gas amplification in a capillary [29]. As another solution for breakdown problem, an improved material of the strips is being tested in our group. It is considered that damage of electrodes due to a discharge will be reduced by using a metal that have higher melting point for the electrodes. The anodes and cathodes of the next version MSGC will be made from chromium that has melting point of 1890°C. These new approaches are expected to solve the discharge problem completely. Even if these charging-up and discharge problems are not solved perfectly, the development of MSGC soon reaches the final goal, opening many applications.

MSGCs with two dimensional readout have been developed by our group as an X-ray imaging device. We are developing MSGCs having $\sim 10\mu$m thin polyimide substrate for

several years [18, 19, 21]. This thin substrate makes possible to obtain two dimensional positions of incident X-rays, to realize the large detection area of 10cm square, and to control flow of ions near the anodes as described in chapter 2 and 3. Our MSGCs are made using Multi-Chip Module (MCM) technology [18, 19], which allows a high density assembly of bare silicon LSI chips on a silicon or a ceramic plane. This technology has been generally available in semiconductor companies. All of our MSGCs have been made in collaboration with the P.C.V.& Module Division in Toshiba Co. Ltd.

Our MSGC with a 200 μm pitch electrode has the following features:

1. fine position resolution of $\sim 100\mu$m,
2. high rate capability for incident X-rays of up to 10^7cps/mm^2,
3. fine timing resolution of ~ 50 ns,
4. mass productivity due to the uniform quality of the MSGC.

In addition to these features, the energy of an X-ray is observable similarly to most of wire chambers, and the high position resolution also enables us to observe the polarization of incident X-rays [30]. By means of these features, multi-dimensional physical variables (two dimensional position, timing, energy and polarization) can be measured simultaneously. For comparison between MSGC and other detectors, performance of X-ray detectors is summarized in Table 1.2. The integral type detectors are now widely used in the measurements where a fine position resolution is required, and the pulse counting detectors are used to those for a fast timing resolution. MSGC has both good imaging and timing capabilities, and it will be applied to the measurements where both of these performances are required.

A very fast data acquisition (DAQ) system which can record X-ray event up to 10^7cps has also been developed. In General, more than several ten thousands of events are necessary in constructing a two dimensional image, and more than a few tens of frames per second are required to display images like a movie. Thus, data taking capability of more than 10^6cps is required for a real-time X-ray imaging analysis. However the capability of existing detectors using delay-line is limited to $\sim 10^5$cps. Therefore, the development of a fast DAQ system is an inevitable work for the application of MSGCs as an area detector. Having a fast DAQ system, MSGC has been able to be used for the observation of time resolved X-ray images in synchrotron radiation (SR) sources. Our goal is to develop an X-ray imaging device

	IP[*a]	PSPC[*b]	SSD[*c]	SC[*d]
Type	Integ.	P.C.	P.C.	P.C.
Dimension	2	1	0	0
Position resol.	$(25\mu m)^2$	$200\mu m$	—	—
Timing resol.	$\times/100ms$[*2]	$10\mu s$	$\sim 1\mu s$	$20ns \sim 1\mu s$
Max. counting rate	$10^8 cps/mm^2$	$10^4 cps$	$10^4 cps$	$10^5 \sim 10^6 cps$
Dynamic range	$\sim 10^5$	Infinite[*3]	Infinite[*3]	Infinite[*3]
Energy resol. (@5.9keV)	—	—	$1 \sim 2\%$	18%
Non linearity (for image.)	$1 \sim 2\%$	perfect?	—	—
Image distortion	$> 1\%$	$> 2\%$	—	—
Online readout[*g]	△	○	○	○

	X-II[*e]	Fiber-CCD[*f]	MWPC	MSGC
Type	Integ.	Integ	P.C.	P.C.
Dimension	2	2	1(2)	2
Position resol.	$(300\mu m)^2$	$(150\mu m)^2$	$500\mu m/30\mu m$[*1]	$(100\mu m)^2/(30\mu m)^2$ *
Timing resol.	30ms	1∼2	20ns	20ns
Max. rate	$10^{6\sim7} cps/mm^2$	$10^8 cps/mm^2$	$\sim 10^4 cps/mm^2$	$> 10^7 cps/mm^2$
Dynamic range	$10^{5\sim6}$	$\sim 10^5$	Infinite[*3]	Infinite[*3]
Energy resol.	—	—	11%	13%
Non linearity	a few %	?[*5]	0%	0%
Image distortion	$\sim 1\%$[*4]	$\sim 10\%$	0%	0%
Online readout [*g]	○ $\sim$ 30ms	○ ∼1s	○ $< 1\mu s$	○ $< 1\mu s$

*a Imaging Plate.

*b Position Sensitive Proportional Counter.

*c Solid State Detector (Semiconductor Detector).

*d Scintillation Counter.

*e X-ray Image Intensifier.

*f The phosphors coupled with CCD via tapered optical fiber.

*g ○ means available, and △ means poorly available.

*1 Using the pulse height information.

*2 Case of the cinema type.

*3 Depending on the readout electronics.

*4 After correction.

*5 Not measured yet.

Table 1.2: Summary of X-ray detectors

having the ability of a real-time imaging processing. The necessity of imaging detectors operated under a brilliant source has been greatly increased, and this detector is expected to be used extensively in such a place as the SPring-8 synchrotron radiation facility in Japan.

In this thesis, I describe the developments of MSGCs, the fast data acquisition system, and the new analysis methods which allow exploiting all the features of MSGC. In chapter 2, the principle of operation and fundamental features of MSGC are described. Design parameters of MSGC and the results of the performance tests are presented in chapter 3 and chapter 4. Chapter 5 is devoted to the development of data acquisition system and its performances. Experiments using MSGC in crystallography are presented in chapter 6. Finally, I present the summary and conclusion in chapter 7.

Chapter 2

Principle of operation and features

2.1 Principle of operation

Figure 2.1 shows the schematic structure of MSGC. The space above the signal strips is filled by a noble gas (argon) mixed with a quencher gas (ethane). Figure 2.2 shows the principle of the operation for detecting X-rays on MSGC. In the argon gas atmosphere, the photoelectric absorption is a dominant process for incident X-rays of a few keV to a few tens keV. When an incident X-ray of energy E_γ is absorbed in a shell of energy E_j, a photo-electron of energy $E_e = E_\gamma - E_j$ is emitted, and residual molecule is excited. This excited molecule can return to its ground state mainly through two competing processes: one is fluorescence and the other is the Auger effect. In the later case, an emitted Auger electron has energy very close to E_j. In argon, about 85% of the photo-electric absorption is followed by the Auger effect, and then the total energy of primary electrons is nearly equal to the incident photon energy. These primary electrons lose an energy by ionizing the circumambient gas. The total number of ion pairs n_T becomes

$$n_T = \frac{\Delta E}{W_i} \quad , \tag{2.1}$$

where ΔE is the total energy loss in the gas volume, and W_i is the effective average energy to produce one ion pair. The whole energy of primary electrons are lost in the gas volume. The value of W_i is 26eV for argon gas. For example, an incident X-ray of 6keV produces about 230 electron-ion pairs, and produced electrons are drifted toward strips. Near the anode strips, the drifted electrons are accelerated enough to ionize circumambient gas. The gain of this gas-multiplication process is a few hundred $\sim$ a thousand in MSGC. Therefore,

$10^4 \sim 10^5$ electrons are collected on the anode strips and the same number of positive ions are collected on the cathode strips and the drift plane.

Charges induced on the strips are proportional to the energy of incident X-rays, and the range of this value is about $2 \times 10^{-15} \sim 2 \times 10^{-14}$[C]. The charges are also induced on back electrode behind the substrate, then two-dimensional readout is possible (see section 2.4). The signals of anodes and backstrips are fed to charge integrating amplifiers having a high gain of 0.5V$\sim$ 5V/pC. The amplified signals are discriminated, and fed to the data acquisition (DAQ) system individually in our MSGC. The details of the DAQ system are described in chapter 5.

2.2 Position resolution

Multi-Wire Proportional Chambers (MWPCs) have been used as a position sensitive detector for charged particles or X-rays. MWPC was proposed by Charpak in 1968 [31] as a particle tracker in high energy physics experiments. A typical structure of MWPC is shown in Fig. 2.3. Both MSGCs and MWPCs have many lines of sense electrode, and an incident particle is detected by gas multiplication process. In order to improve the position resolution, the simplest method is to reduce the spacing of lines (wires or strips). However, the closer the wire spacing is, the less the electric field around the anode wires becomes at the same operation voltage. An approximate expression of the electric field in MWPC has been given by Erskine [32]. Although the higher operation voltage is needed for narrowly spaced MWPC, the short spacing with high voltage causes an instability on wires by electrostatic force. For example, let us consider MWPC having 1mm wire spacing, 8mm cathode gap, 10μm diameter anode wires of tungsten and filled with pure argon gas. In obtaining $\sim 10^3$ gas gain, 2.2kV is necessary as the operation voltage, and the critical length L_c is 1m. Here, the critical length is the maximum length of anode wires without support along wires avoiding the distortion of wires. For a 0.5mm wire spacing, 4kV is necessary, and L_c is 50cm. These are calculated assuming the operation under pure argon atmosphere. In the actual case, because the quenching gas is mixed, higher operation voltage is required, and then critical length becomes shorter.

MSGC has sensing strips printed on the substrate instead of wires of MWPCs. A schematic structure of MSGC is shown in Fig. 2.4. All strips are printed on the dielectric

substrate, which can withstand the mechanical forces. The strips are printed by the same technique as the IC (Integrated Circuit) technology, which provides precise printing within 1μm error. This technology enables us to make very fine (10μm order) layout of the signal electrodes. In MSGC, cathode strips and anode strips are alternately placed. This structure makes enough high electric field to produce the gas multiplication. The force due to the strong electric field around the anode strips can be sustained by the arrangements of anodes and cathodes. For example, let us consider the simple structure of MSGC for rough calculation as shown in Fig. 2.5. The radius of each electrode is a, spacing between the anode and the cathode is s, and the operation voltage of the anodes and the cathodes are V_0 and 0. No field plane is placed near these wires. The capacitance per unit length of each wire is expressed as

$$C = \frac{2\pi\varepsilon_0}{\ln(s/2\pi a)} \quad , \tag{2.2}$$

where ε_0 is dielectric constant in a vacuum. An approximate value of electric field is obtained from the following expression:

$$E(x,y) \simeq \frac{CV_0}{2\pi\varepsilon_0}\frac{1}{r}, \qquad r = \sqrt{x^2+y^2} \quad , \tag{2.3}$$

and the multiplication factor is roughly estimated by following equation:

$$M = \exp\left[2\sqrt{\frac{kNCV_0a}{2\pi\varepsilon_0}}\left(\sqrt{\frac{V_0}{V_T}}-1\right)\right] \quad , \tag{2.4}$$

where, N is the number of molecules per unit volume, and k is a parameter appearing in Korff's approximated expression for the first Townsend coefficient [33]. This value depends on the kind of gas: $k = 1.81 \times 10^{-17}\mathrm{cm}^2\mathrm{V}^{-1}$ for argon and $k = 0.11 \times 10^{-17}\mathrm{cm}^2\mathrm{V}^{-1}$ for helium. V_T is the threshold voltage to begin the process of the gas-multiplication. The results of the calculation for obtaining 10^3 gas gain with $10\mu\mathrm{m}\phi$ electrodes are shown in Table 2.1.

The real MSGC geometry is different from this model; electrodes are not cylindrical, the shapes of the anodes and the cathodes are different, and other materials exist around the electrodes such as the dielectric substrate. The electric field using numerical calculations for the real MSGC structure is shown in section 3.4. From Table 2.1, only several hundred volts are required for the MSGC operation. Since there is practically no limit from the electrostatic force, the anode spacing of 200μm, which is impossible for wire chamber, can be realized in our MSGC.

	anode pitch (mm)			
	0.1	0.2	0.5	1
Operation voltage (V)	70	175	315	420

Table 2.1: Calculated voltage necessary for obtaining gain of 10^3 with MSGC like setup

2.3 Space charge effect

Most of the gas chambers with wire electrodes suffer from a space charge gain limitation due to the existence of ions in the gas volume, which are produced through the gas multiplication process near the anodes. These ions reduce the electric field in chamber until they reach cathode electrodes. Almost all the wire chambers have the ion drift region of more than several milli-meters thickness. The ion drift velocity w^+ is found to be linearly proportional to the reduced field E/P, where E is the electric field and P is the gas pressure. The mobility μ^+ of ions is defined as

$$\mu^+ = \frac{w^+}{E} \quad .$$

Some values of μ^+ in argon and other gases [34] are shown in Table 2.2.

Ions	Mobility μ^+ ($cm^2V^{-1}sec^{-1}$)
Ar^+	1.70
CH_4^+	1.87
CO_2^+	1.72
$IsoC_4H_{10}^+$	1.56

Table 2.2: Mobilities of typical ions in gases at the normal condition.[34]

In the MWPC of Fig. 2.3, the electric field E of the drift region (not around the anode wires) is expressed as

$$E \simeq \frac{CV_0}{2\varepsilon_0 s} \quad . \tag{2.5}$$

Then, in the typical arrangement of MWPC: for example, $\ell = 5$mm, $2a = 20\mu$m, $s = 2$mm, $V_0 = 4$kV — the ion drift time is calculated to be 50μs.

Whereas, in MSGC, the ions produced around the anode strips are collected in cathode strips. The distance from an anode to a cathode of MSGC is quite shorter ($< 1/100$) than

that of MWPC, and electric field along the path of ions is very high ($\sim \times 10$) because of the short distance between the electrodes. In the typical geometry of MSGC: distance between anode and cathode = 50μm, operational voltage = 400V — the ion drift time is found to be about 40 ns. The ion drift time of MSGC is over 1000 times faster than that of MWPC, then MSGCs can operate under very intense X-rays or charged particles of up to about 10^7cps/mm^2.

2.4 Two dimensional readout

The thin substrate of MSGC makes possible a two dimensional readout using the additional electrode that is printed behind the substrate. Figure 2.6 shows the principle of two dimensional readout.

At the moment after the gas multiplication has occurred, the cloud of ions remain around an anode strip. This cloud is spread about 5μm wide around anode (in analogy to the case of proportional chamber). When this cloud is defined as a square plane conductor with the following properties: charge of Q, area of $S \simeq (10\mu\text{m} + \text{anodewidth})^2$ and the distance from anode of h, the induced charge on the backstrips may taken from the capacitance between this temporally created conductor and each electrode. When C_b is defined as the capacitance between the ion cloud and backstrips, and C_a is defined as that between the ion cloud and the surface strips (cathodes and anodes), the induced charge on the backstrips Q_b is expressed as

$$Q_b \simeq \frac{C_b}{C_a + C_b} Q \quad . \tag{2.6}$$

Defining d as the thickness of the substrate and assuming that an anode has width of w, approximate expressions of C_a and C_b are the following:

$$C_a \simeq \frac{w\sqrt{s}}{2h\varepsilon_0}, \qquad C_b \simeq \frac{(s - w\sqrt{s})}{2(d+h)\varepsilon_0} \quad . \tag{2.7}$$

By substituting (2.6) into (2.7), the following equation is obtained:

$$Q_b \simeq \frac{hs - hw\sqrt{s}}{hs + dw\sqrt{s}} Q \quad . \tag{2.8}$$

Therefore, the thinner the substrate is and the narrower the anode strips is, the larger the induced charge on backstrips becomes. Our MSGC has a very thin substrates of $\sim$20μm

thickness, then comparatively large signals are induced on backstrips. Two-dimensional readout is realized by arranging the backstrips orthogonally to the anodes.

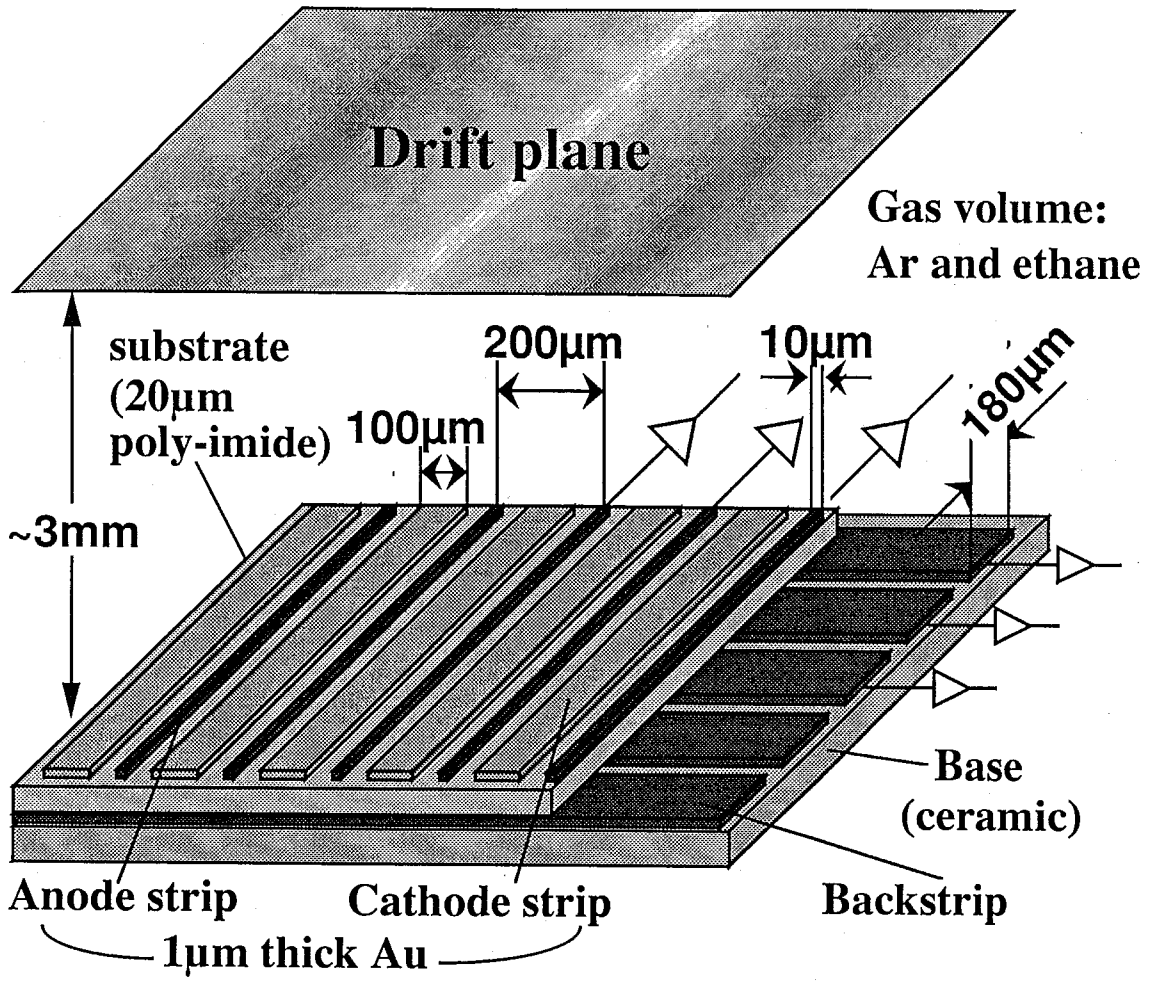

Figure 2.1: Schematic structure of the two-dimensional MSGC which is formed on a 17 μm thin polyimide substrate. On the polyimide layer, 10 μm wide anodes and 100 μm wide cathodes are formed with a 200 μm pitch. Between the ceramic base and the polyimide substrate, there are backstrips with a 200 μm pitch orthogonal to the anodes. All electrodes are made of gold with a thickness of 1 μm. To define the drift field, the drift plane is placed at 3 $\sim$ 10mm above the substrate.

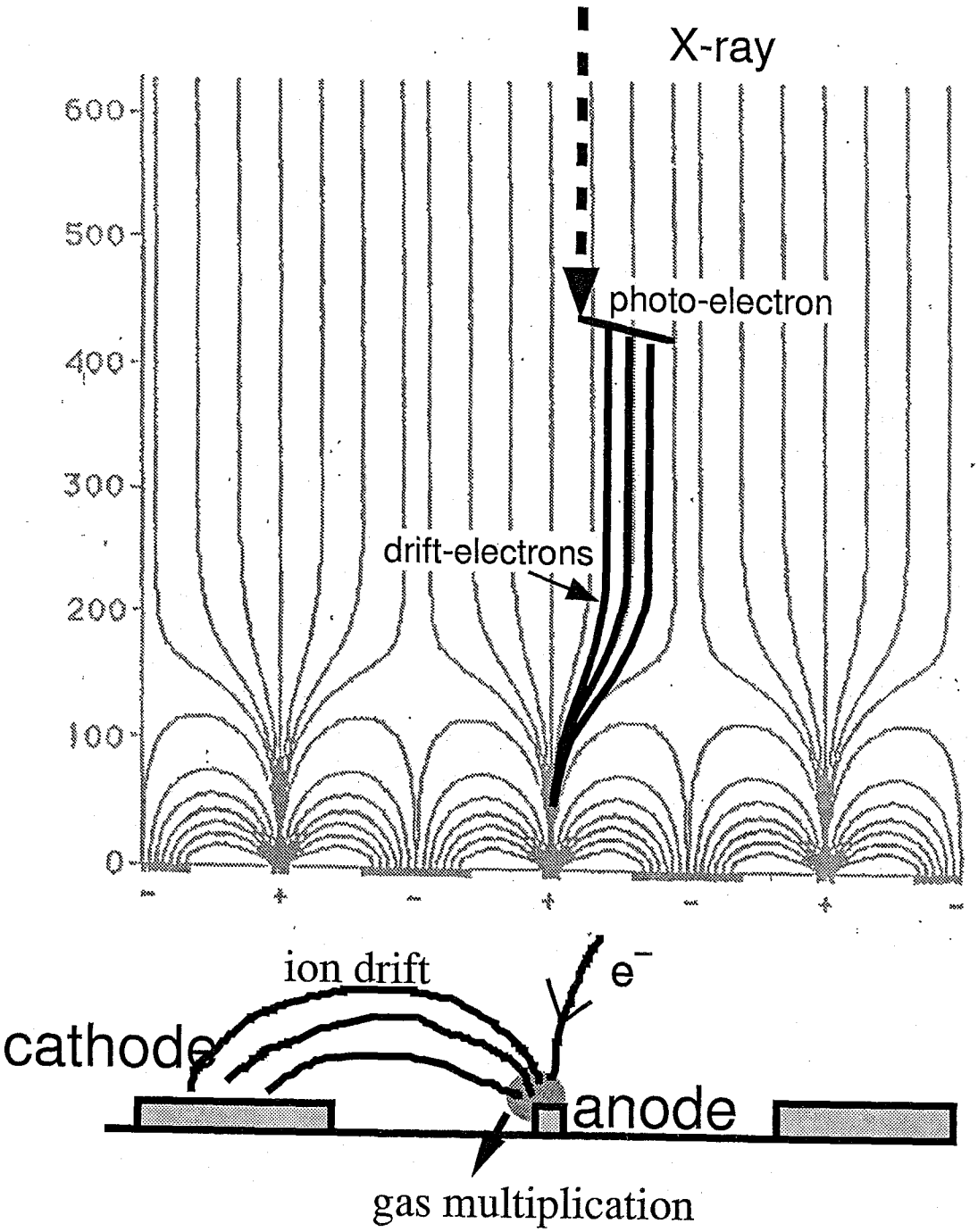

Figure 2.2: Principle of operation for detecting X-rays on MSGC.

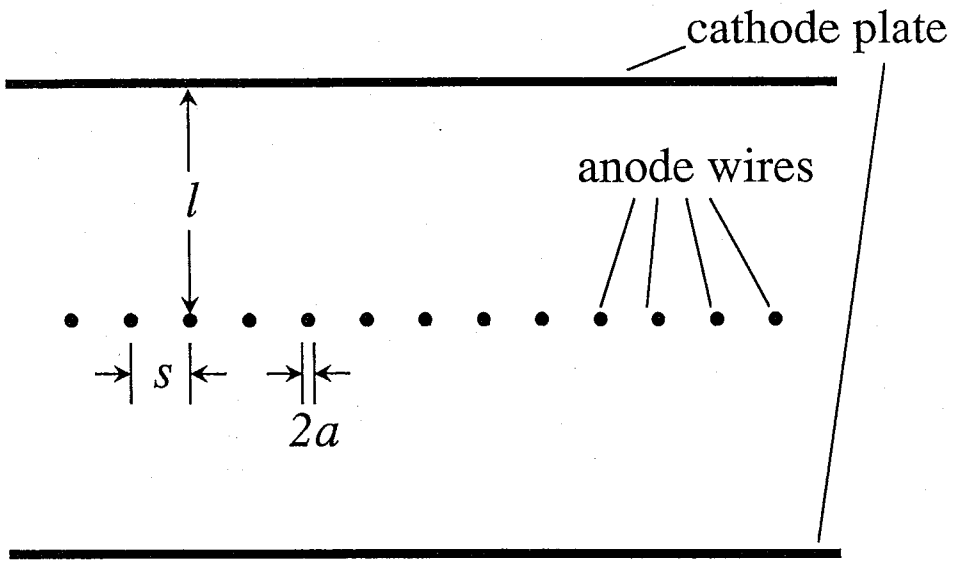

Figure 2.3: Schematic structure of MWPC.

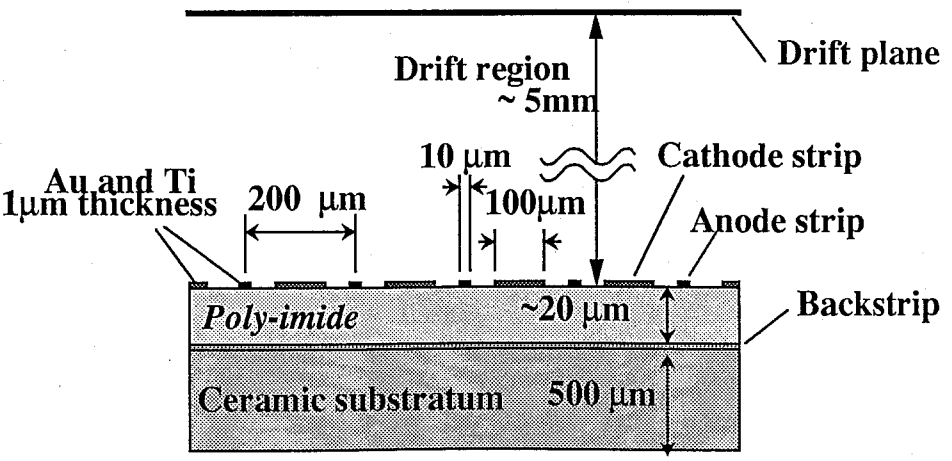

Figure 2.4: Schematic cross section of our MSGC.

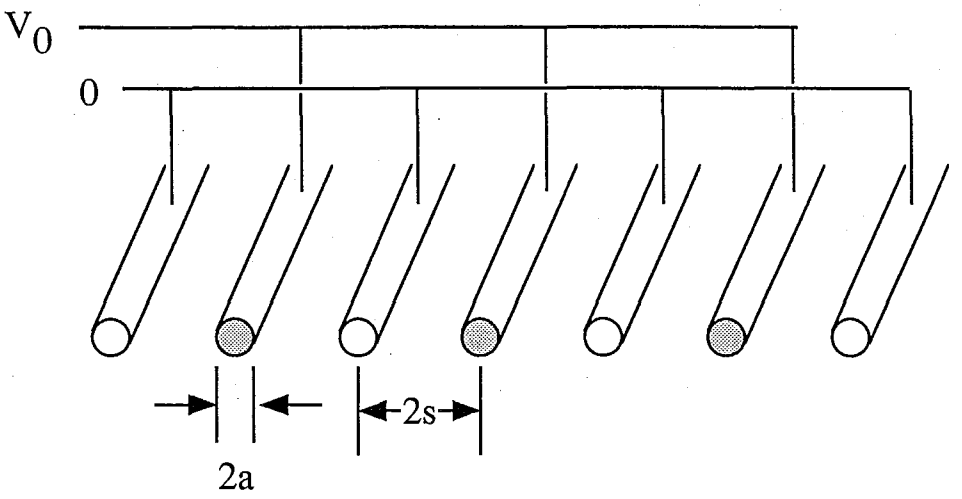

Figure 2.5: Simplified structure of MSGC for calculations.

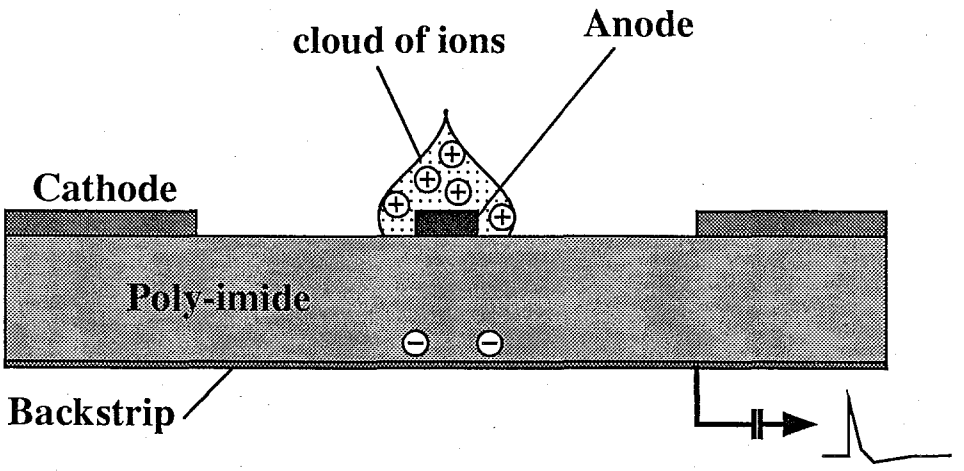

Figure 2.6: Principle of the two-dimensional readout from backstrips. Remaining ions around an anode induce a signal on backstrips.

Chapter 3

Design parameter of MSGC

3.1 General structure of our MSGC

Since MSGC was invented in 1988 by A.Oed [1], a lot of ideas of its structure have been proposed and tested. Oed's group made MSGC with anode pitch of 200μm and width of 10μm on a 300μm thick glass substrate. Up to now, the Pisa university group developed a two-dimensional MSGC with backstrips [15], and succeeded in obtaining two-dimensional image using 1.8μm thick SiO_2 insulator between anodes and backstrips [20]. In the same time, we have developed the a two-dimensional MSGC with thin organic substrate that was made of poly-imide using multi-chip module technology [18, 19]. These days, MSGC is considered to be suitable in many fields for detecting charged particles, neutrons and X-rays. We have mainly developed MSGC as an imaging detector for X-rays.

There are a lot of design parameters of MSGC which have to be optimized for the stable operation as follows:

1. the selection of noble and quencher gas, mixture ratio, gaseous volume, and pressure.
2. structures and materials of electrodes,
3. thickness of substrate, its material, and suitable operation voltage.

Other features such as an amplitude of output signal, a stability in operation, and the position resolution strongly depend on these parameters. In this chapter, the optimization of these parameters is described in detail.

Figure 2.1 in chapter 2 shows a schematic structure of the two-dimensional MSGC, which is formed on the 20μm thick poly-imide substrate. On the poly-imide layer, the 10μm wide anodes and the 100 μm wide cathodes are formed by the photo-lithography technology. In

order to tightly maintain the structure, the MSGCs are made on the thin ceramic base. Between the ceramic base and the poly-imide substrate, there are backstrips with a 200μm pitch in orthogonal to the anodes. All electrodes are made of gold with the thickness of 1μm. To define the drift field, a drift plane is placed 3mm$\sim$10mm above the substrate. Following two types of two-dimensional MSGC have been made:

- type I: 5cm$\times$5cm detection area with 254$\times$255 readout electrodes.
- type II: 10cm$\times$10cm detection area with 512$\times$512 readout electrodes.

Every 15 (type I) or 32 (type II) cathodes are aggregated to one group at one end in 5cm square or 10cm square MSGC respectively, and the negative high voltage is supplied (Fig. 3.1). One MSGC has several cathode groups to which high voltages are independently supplied. The edge of the cathode is coated by poly-imide with a width of $\sim$ 7μm for suppressing discharge between the anodes and the cathodes (see Fig.3.10 in section 3.3). Argon and ethane were used as a noble gas and quencher gas, respectively. The detail of the gas mixture is mentioned in section 3.2.

All of signal electrodes are connected to the patterns on the printed board with the wire bonding technology. In the type I: 5cm square setup, to evaluate the newly developed MSGC as quickly as possible, we have developed a removable MSGC package and a read-out system specific to the two-dimensional MSGC. For a tracking device having a very precise position resolution, the handling of a large number of signals in a small area is inevitable and important problem. At the stage of R&D, we should actually handle a lot of signals for each different prototype for the evaluation of its imaging performance, and then a high cost, a long time and large amount of manpower are necessary to finish the development. For this troublesome problem, we found a simple solution: setting the MSGC on a large Pin Grid Array (PGA) package having more than 500 pins on the backside [1]. Every time when we change the specification of an MSGC, the new MSGC can be readily operated and studied by only replacing the MSGC package on the circuit board. Figure 3.2 shows the top and bottom views of the PGA package on which a 5 cm$\times$5 cm two-dimensional MSGC is mounted. The package is made of ceramics with a 8 cm$\times$8 cm size, and has 541 pins with a 0.1 inch pitch on the backside. Since all electrodes of 254 anodes and 255

[1]Our MSGCs are actually produced and mounted on a PGA package by P.C.V.& Module Division in Toshiba Co. Ltd.

backstrips and 17 groups of cathodes are connected to pads on the ceramic package by gold-wire bonding and fed to backstrip pins; no wire has to be connected to the MSGC plates directly. It is particularly noteworthy that signals from backstrips which lie under the substrate are derived through the micro through-hole pad on the substrate by means of MCM technology as schematically shown in Fig.3.3, and all the pads from all electrodes on the MSGC are placed on the surface of substrate. This makes bonding between the MSGC and the package very easy. The cross talk between adjacent strips was measured to be $\sim$ 5%, which is not serious for digital read-out in our MSGC. The MSGC package is mounted on a printed mother board on which a gas vessel is attached around the MSGC as shown in Fig. 3.4. The preamplifier cards are inserted vertically to the connectors on the mother board to reduce the size of the mother board.

However in the case of type II, the new 10 cm square MSGCs are directly mounted on 30 cm square mother board by a wire bonding technique to reduce the space of the mother board. In addition, some ideas have been adopted for the mother board to handle more than a thousand signals in 30 cm square size: the structure of 8 layer circuit board, and the micro resistor arrays attached by bonding. Figure 3.5 shows a mother board on which the 10 cm square MSGC is mounted. The 16 preamplifier cards are inserted vertically to the connector on the rear side of the motherboard. Each card has 64 fast amplifiers (MQS104 developed by LeCroy) and discriminators. All discriminated signals from the anodes and the cathodes (ECL level) are fed to the newly developed position encoded system.

The gas vessel is attached directly on the mother board of both the type I and II. Figure 3.6 shows the cross section and top view of the gas vessel used for the 10 cm square MSGC. The side of this vessel has four holes at its side. Gas is supplied from two of those holes, and discharged from the other holes. The front cover of the vessel has a window for incident X-rays and a drift plane. The window and the drift plane are made of aluminized mylar. The drift voltage is supplied from the front cover of the vessel.

3.2 The gas mixture

Most of all the gas detectors having avalanche multiplication process use noble gases. In particular, a gas with short absorption length of photon is required for an X-ray detector, and then noble gases with high atomic number are required. As well known, the cross

section of photoelectric absorption is approximately proportional to Z^5 and $E^{7/2}$, where Z is an atomic number of the gas, and E is the energy of an incident photon, when photon energies are greater than the energy level of the K-absorption edge and less than the electron mass. Photon absorption lengths in typical gases are shown in Fig. 3.7 [35]. The best gas for an X-ray detector is xenon gas, and the second may be krypton gas to obtain high quantum efficiency. However, xenon gas is relatively expensive, and krypton gas contains a lot of radioactive isotopes. Therefore, we have chosen argon gas for verification of the performances of the MSGC.

Ethane gas is used as a quencher. In the case of MSGC, since the distance from anode to cathode is very short, fluorescent photons produced near the anodes in gas multiplication process are likely to reach at the cathodes, and it is feared that the photo-electrons produced in cathodes cause discharges between anodes and cathodes. Then strong reduction of fluorescence is required to avoid discharge. Usually, thick concentration of quencher gas is used for MSGC. Even the pure (100%) quencher had been used at the CERN group [7]. The mixture ratio of 50% : 50% for argon and ethane is used for our MSGC.

The absorption length for this mixture gas is approximately twice of that of pure argon gas. The conversion efficiencies for $4 \sim 15$keV X-rays are calculated as shown in Fig. 3.8. Although a thicker volume provides higher efficiency for detecting X-rays, a thick volume makes the position resolution worse because of the longer drift distance and of serious effect of the slanting angle of the incident X-rays. The diffusion of drift electrons is approximately proportional to the square of the drift distance. For 1cm drift length, the diffusion of electrons is more than $\sim 200\mu$m. For some experiments, the effect of the slant angle of the incidence would be a critical problem. As shown in Fig. 3.9, incident X-rays which have the slant angle θ are absorbed on the way along the X-ray trajectory in the gas volume. Then, the converted electrons drift vertically to the anode strips. This effect significantly blurs the position resolution. The blur by this effect is roughly expressed as $d \sin\theta$, where d is the thickness of the gas volume. This effect is especially critical for a wide angle X-ray diffraction measurement such as the crystallography. The demands on the detection efficiency and on the position resolution are the conflicting requirements. The most reasonable thickness of the gas volume is dependent on each experimental requirement. Our MSGC has a drift plane with variable position from 3mm to 10mm above the MSGC

substrate.

3.3 Structures and materials of strips and substrate

In the present technology, the pitch of anodes can be made below 100μm. However, since the diffusion lengths of electrons are more than one hundred μm for X-rays of energy more than 5keV, the ionized electron clouds spread over a few hundred micro-meter. Therefore, $\sim$ 200μm is enough for anode pitch which gives RMS position resolution of $\sim$ 60μm.

The most distinctive feature of our MSGC is a very thin substrate of poly-imide of 20μm thick. Most of the MSGCs in the world are formed on inorganic substrate such as glass [1, 10, 36], SiO_2 [20] or diamond [37]. These inorganic substrates are weak against mechanical tension. It is well known that the difference of thermal expansion coefficients of electrodes and the substrate will break the structures for large area MSGCs. We have chosen poly-imide, which has an elasticity and resistivity for high voltage up to 1kV/μm, and we have developed a new type of MSGC on a thin poly-imide substrate using the multi-chip technology which supports high-density assembly of bare LSI chips on a silicon wafer or ceramic [18, 19]. It provides good features for the MSGC of thin multi-layer structures. By this technology, the protection for cathode discharge has been realized by the over-coated poly-imide with a width of $\sim$ 7μm as shown in Fig. 3.10 and Fig. 3.11. This coating effectively suppresses the discharge from the cathode edge, and drastically increases the durability against dust attached on the surface. Since the potential on the edge of the cathode has no effect on the gas amplification, this passivation makes no effect on the gain at the same operation voltage. In this method, the limit for operation voltage (breakdown voltage) is over 600V with gain of $\sim 10^4$. This is to be contrasted with the non-passivation type, which frequently sparked above $\sim$ 500V [18, 19].

Nowadays, the gain variation has been well known as a critical problem for MSGCs. This variation is caused by charge-up due to high resistivity on the surface of the substrate. The poly-imide which is used in our MSGC has the surface resistivity of $\sim 10^{16}\Omega$/square which is one of the highest resistive materials. Therefore, the control of surface resistivity was one of the most important subjects to be overcome. In the early stage of our development, to reduce the surface resistivity of the substrate, organic titanium was coated on the surface of poly-imide in a very small thickness, by which the surface resistivity of $\sim 10^{15}$ Ω/square was

obtained. This surface resistivity seems to be a little too high for obtaining stable operation at high counting rates of $> 10^7$cps/mm^2 [21]. The gain stabilities under higher flux X-rays for variable surface resistivity have been also studied elsewhere (see Ref. [22, 38, 10]e.g.). However, we have found one solution for this problem by adjusting both the thicknesses of the substrate and the potential of the electrodes, which is described in detail in the next section. The studies of MSGC with high resistivity are also described in [39, 24].

3.4 Computer simulation on the electric field

Although the electric field for a simplified MSGC is schematically shown in section 2.2, real MSGCs have more complex structures as shown in Fig. 2.4. The calculation of the field and multiplication factor is very complicated by analytical methods, and then a numerical calculation is usually carried out for obtaining suitable design. The optimizations of the anode width (w_a), a cathode width (w_c), a thickness of substrate (d), and operation voltages of these strips (V_a for anodes, V_b for backstrips and V_c for cathodes) were calculated using computer simulation program "Garfield" which was developed in CERN for calculating electric fields of wire chambers. The details of this simulation are described in reference [39], and in this section, only the summarized results are presented. Those parameters were optimized by satisfying the following requirements:

(1) lower probability for discharges,

(2) stable gain,

(3) higher gain.

The probability for discharges was estimated from the strongest electric field around the cathode strip. The emission of electron from the cathode can be suppressed by the reduction of electric field around the cathode strip. Figure 3.12 shows the electric field near the surface of the substrate. These fields were calculated at the position of 1.5μm above the surface of the strips, varying the position across the surface strips from the center of the cathode to beyond an anode along the x-axis. In Fig. 3.12, the region of $x < 93.2 \times 10^{-3}$cm corresponds to the cathode strip, and $99.5 \times 10^{-3} < x < 100.5 \times 10^{-3}$cm corresponds to the anode strip. The potential voltage of the backstrips V_b was fixed to zero volt in these calculations. From these calculations, the probability of discharges was found to increase as V_c increases, and this tendency was small when the substrate was thick. In the case of

thick substrate, the variation of electric field near an anode was comparatively small for that of V_b. This calculation indicated that the thicker substrate suppresses the discharges more efficiently.

The gain stabilities were estimated from the perpendicular component of the electric field E_y on the surface of substrate. If $E_y < 0$, ions which are produced around anodes are drifted onto the surface of the substrate, and the electric field around the strips decreases. In the case of $E_y > 0$, the positive ions are repelled from the surface and drift toward the cathode strips. The E_y was calculated at the point **c** as shown in Fig. 3.13. The results of this simulation are presented in Fig. 3.14. In this simulation, the widths of anode strips and cathode strips were 10μm and 63μm respectively. The applied voltages between anodes and cathodes are always 500V, then cathode voltage V_c is taken as $V_c = V_a - 500$V according to the following discussions. For higher V_a voltage, E_y tended to be negative value. In the case of $V_a = 0$, E_y is always positive as shown in Fig. 3.14(c). This condition is however likely to cause discharges between anodes and cathodes as mentioned before. The condition of $E_y > 0$ is satisfied in the positive voltage region as shown in Fig. 3.14(b).

The gas gain was estimated from the electric field around the anode strips. The Garfield also provides a multiplication factor of a gas avalanche. The results of this calculations varying the width of anode strips W_a and that of cathode strips W_c are shown in Fig. 3.15. Wider cathodes and narrower anodes are found to provide higher gain. The distance between the anode edge and the cathode edge is determined by the cathode width. The electric field is approximately proportional to inverse of the distance. The relation between the gain and the anode width is complicated because the electric field depends both on the capacitance of strips (large for narrow W_a) and on the inverse of the gap between the cathode and the anode (small for narrow W_a). Although a wide cathode produces higher electric field, a small gap between the anode and the cathode is also the main reason of discharge. In our structure, $W_c = 100\mu$m was used. The optimized W_a value for W_c of 100μm is found to be $4 \sim 7\mu$m from Fig. 3.15(d). However, it is difficult to make long anode strips narrower than 10μm because of the technical problem. Then $W_a = 10\mu$m is finally used for our MSGC. The variation of gain can be kept within about 20% compared to most suitable condition.

The design parameters are summarized in Table 3.1.

	Type I	Type II
Detection area	51mm×51mm	102mm×102mm
Signal readout		
anode	254	1024
backstrip	255	1024
cathode	17	16
Pitch size	200μm	
Anode width	10μm	
Cathode width	100μm	
Gas	Ar:C_2H_6 (50:50)	
Drift space	3 ~10mm	5mm
Substrate thickness	17μm	20μm
Substrate material	poly-imide	
Surface processing	organic Ti	none
Surface resistivity	$10^{14} \sim 10^{15}\Omega/\square$	$> 10^{16}\Omega/\square$

Table 3.1: Summary of design parameter

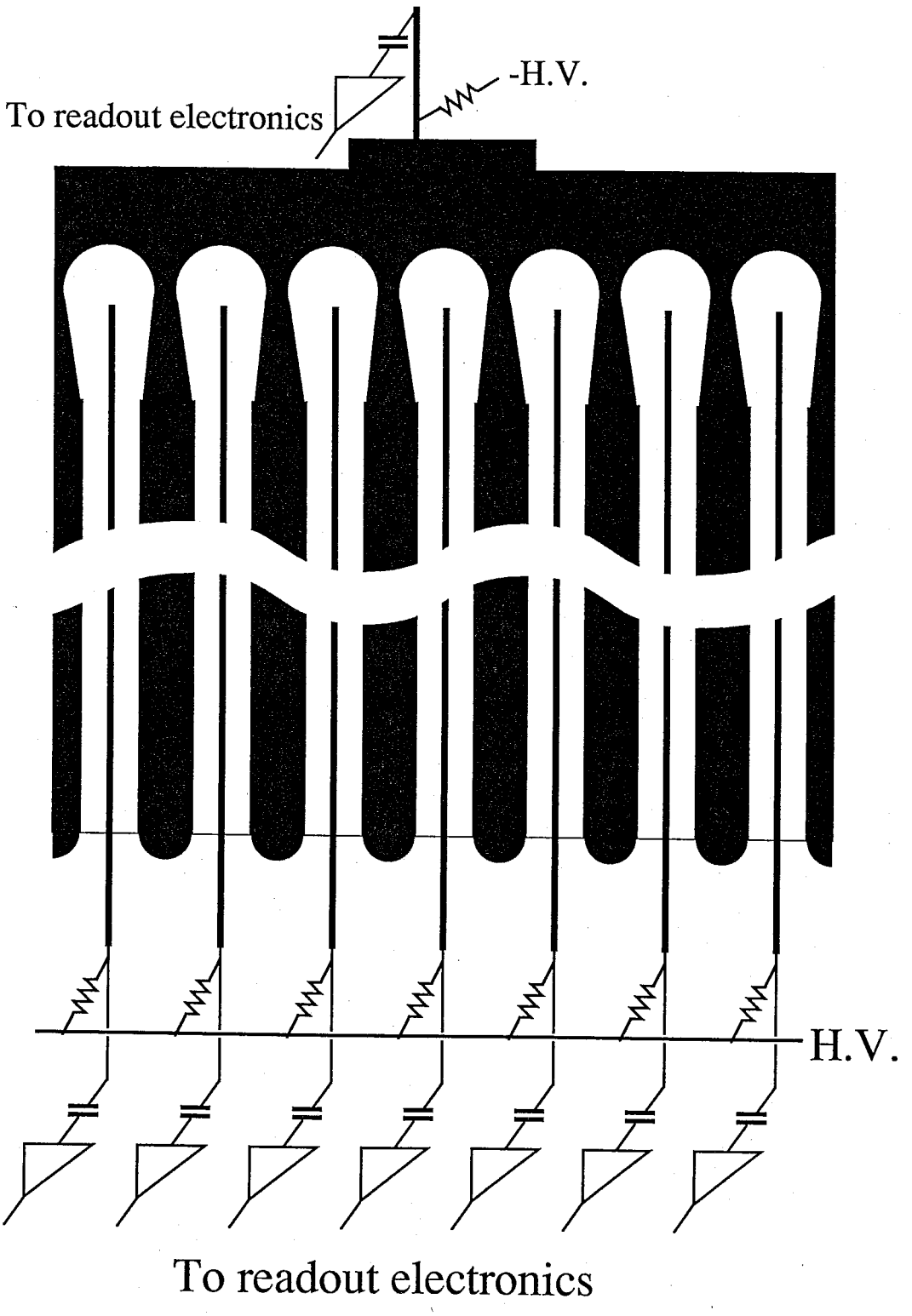

Figure 3.1: Every 15 (or 32) cathodes are aggregated to one group at one end. The output signals are obtained from all anodes and the aggregated cathodes.

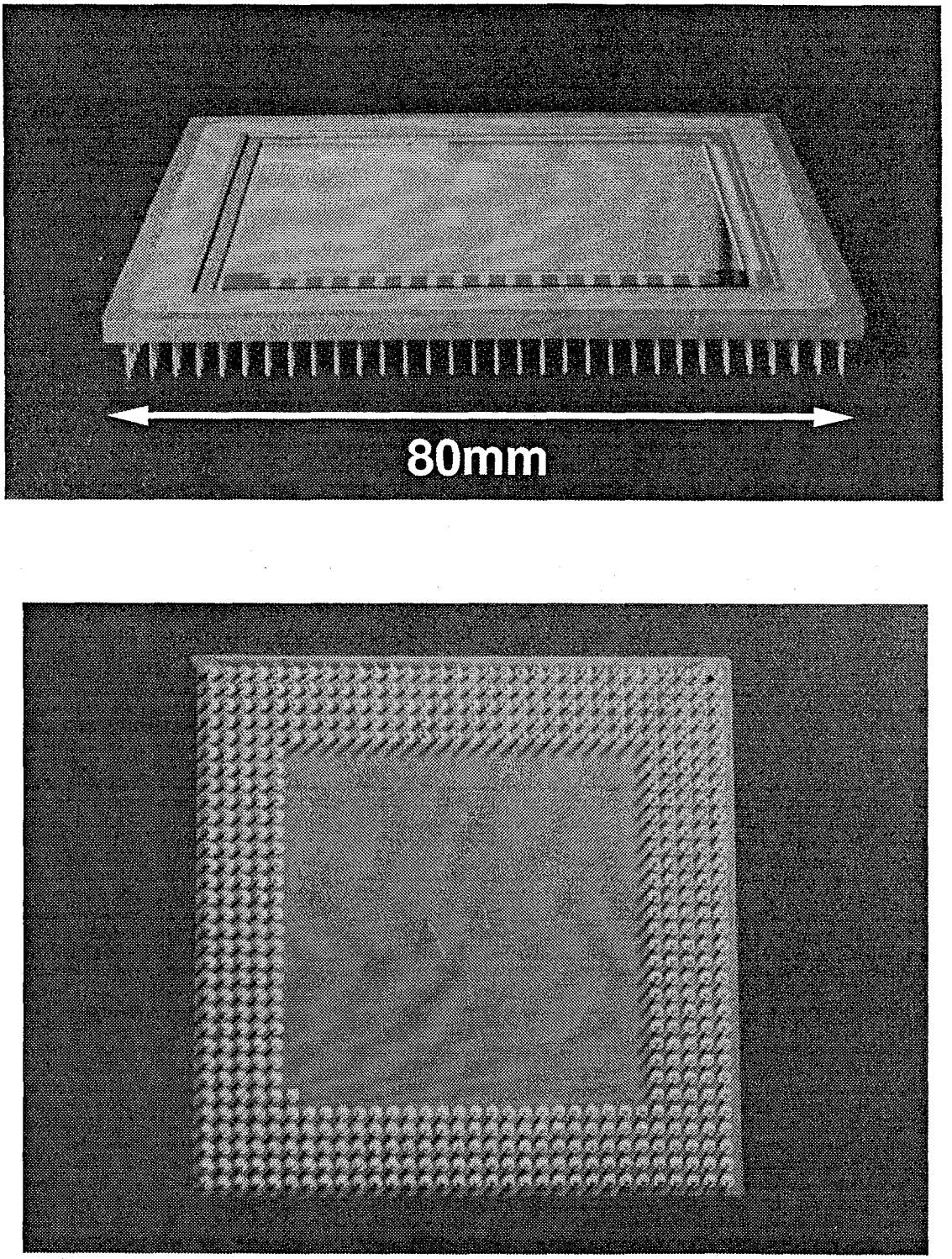

Figure 3.2: MSGC mounted on PGA package. Figures show the top view and bottom view of this package.

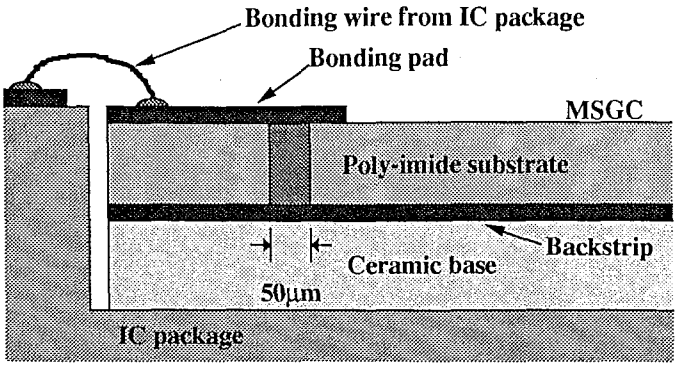

Figure 3.3: Schematic structure of the cross section near the bonding pad. The bonding pads and bonding wires are made of gold. The signals from back strip are lead to the bonding pad by a micro through-hole.

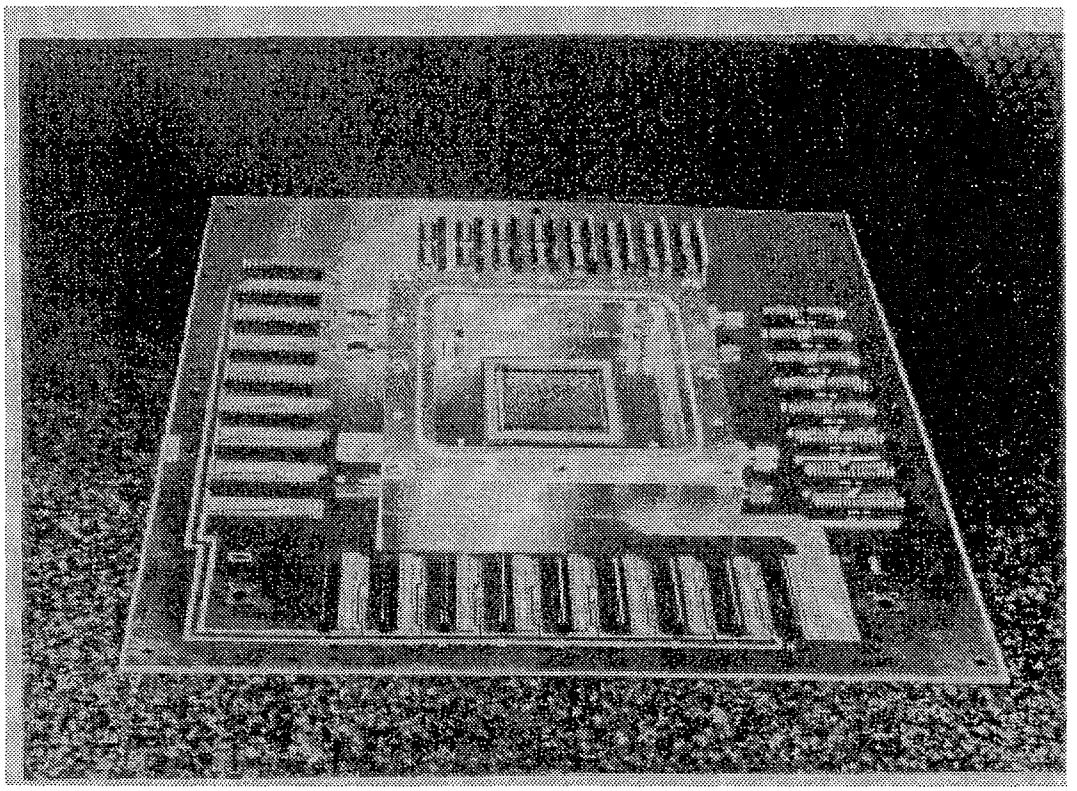

Figure 3.4: Photograph of the printed mother board on which a type I MSGC is mounted. The gas vessel is attached around the MSGC. Preamplifier cards are inserted vertically to the connectors on the mother board.

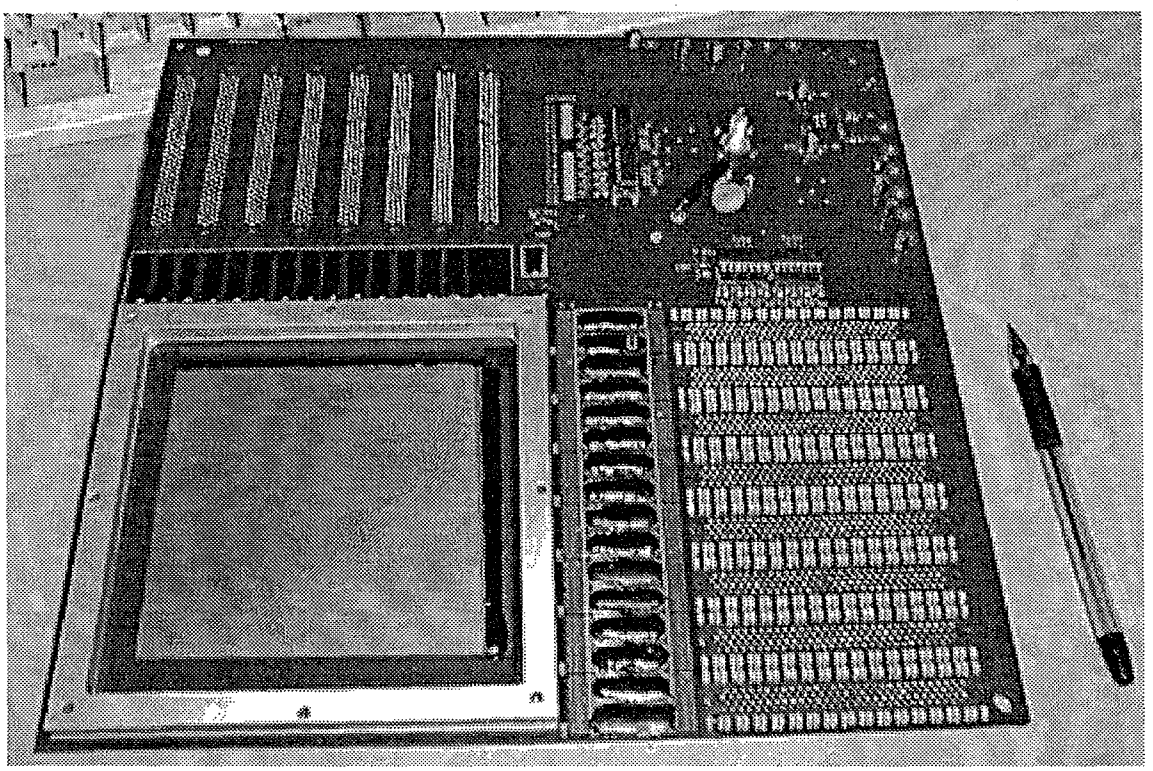

Figure 3.5: Photograph of the printed mother board on which a type II MSGC (10cm square) is mounted. The gas vessel was removed in this photograph. Preamplifier cards are inserted vertically to connectors behind it.

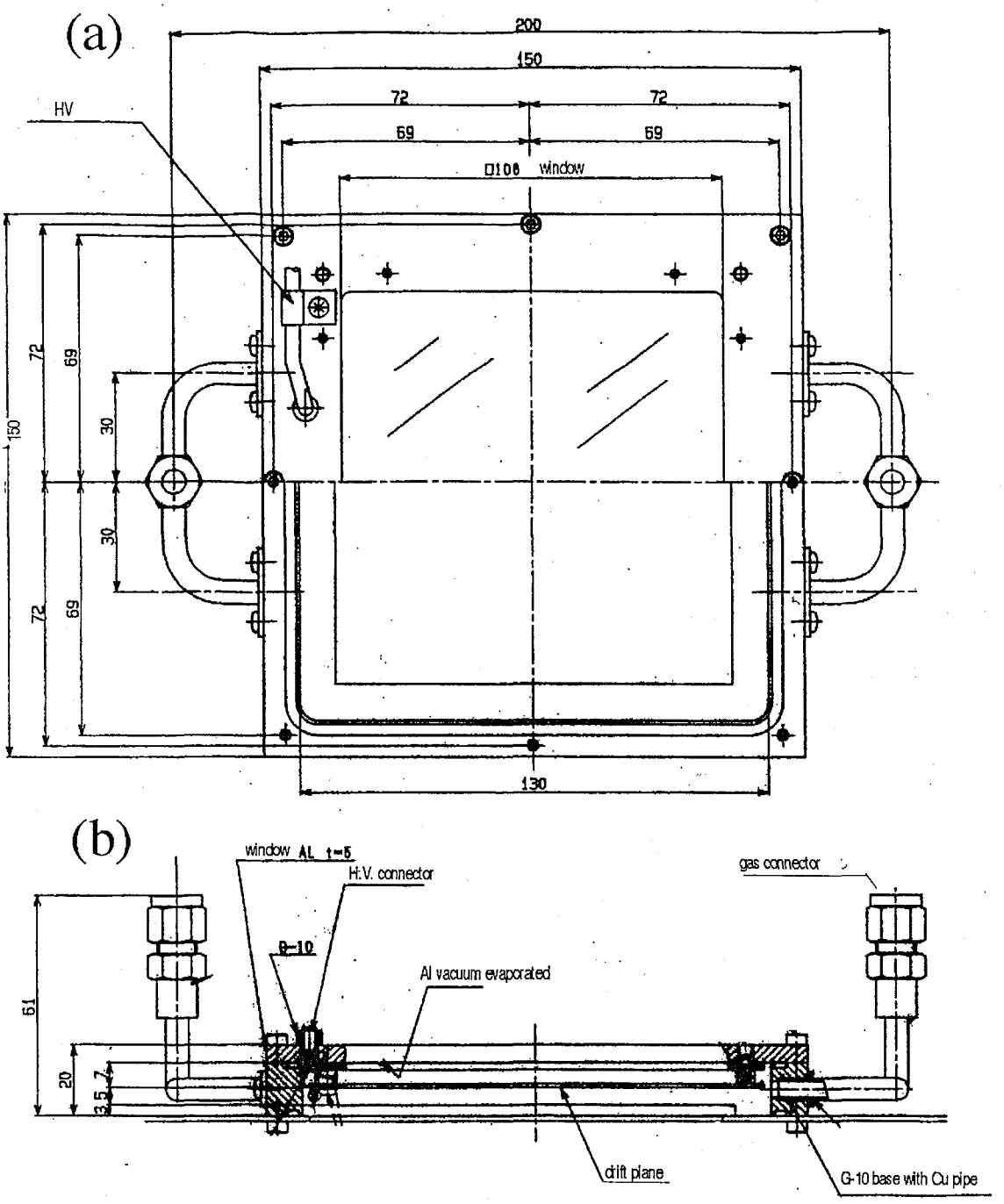

Figure 3.6: Design of gas vessel for type II MSGC. (a) shows the top view and (b) shows the cross section.

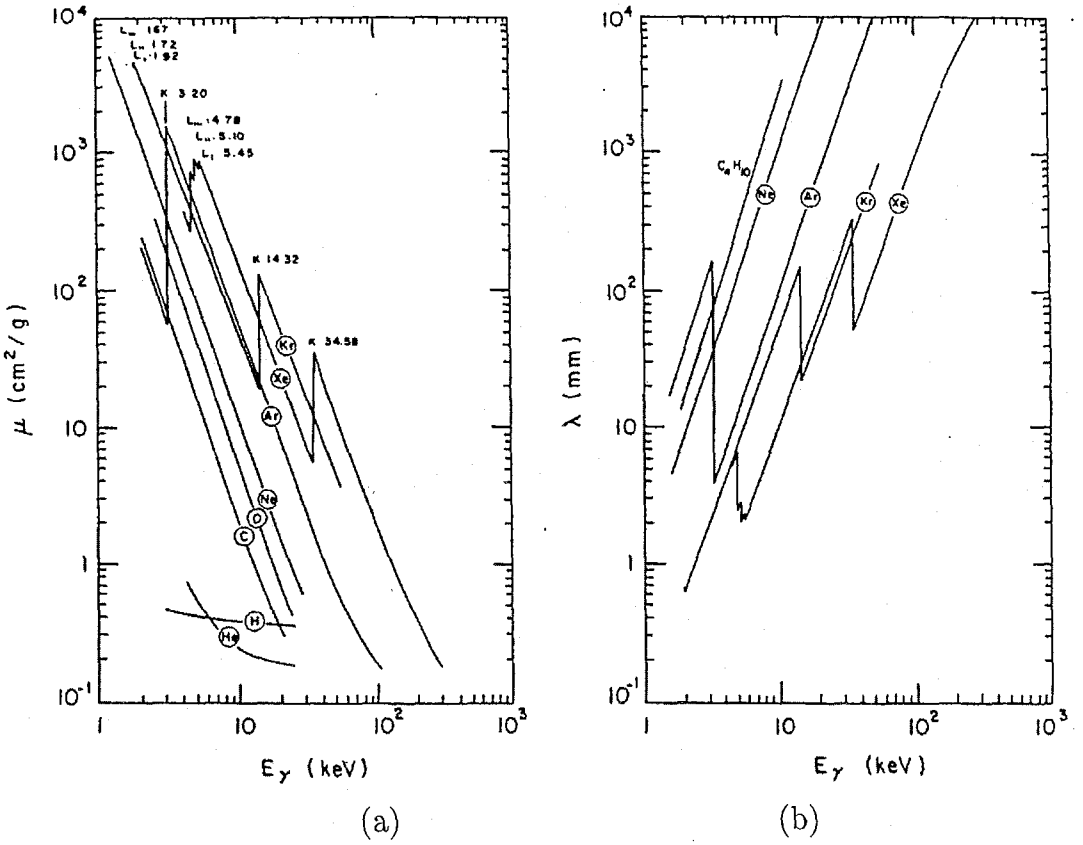

(a) (b)

Figure 3.7: Cross sections of photoelectric effect (a) and mean free path (b).

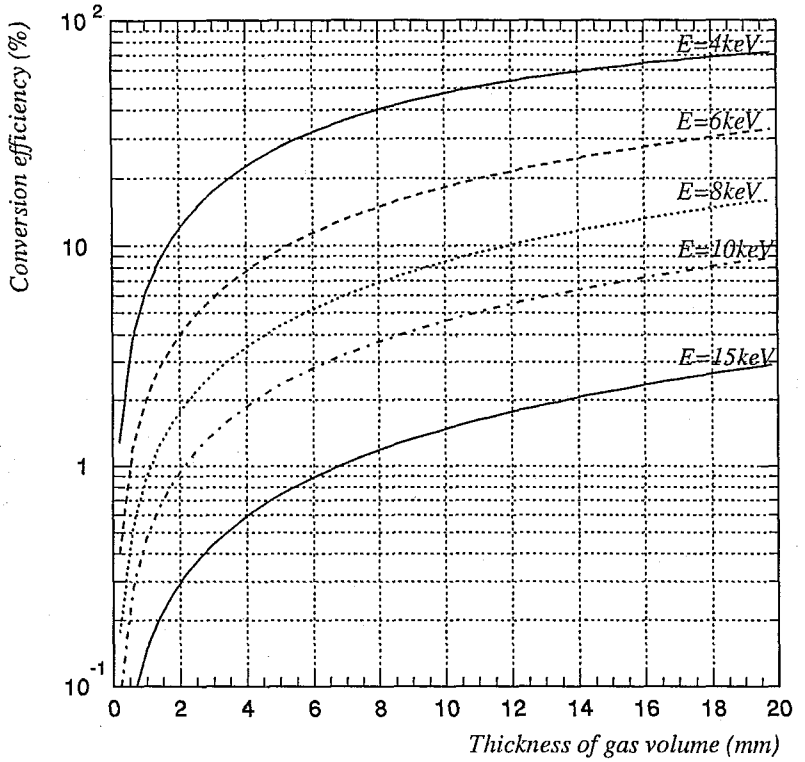

Figure 3.8: Conversion efficiencies for X-rays of various energies for an MSGC of 5mm drift spacing. The gas mixture is Ar : $C_2H_6 = 1 : 1$ in this calculation.

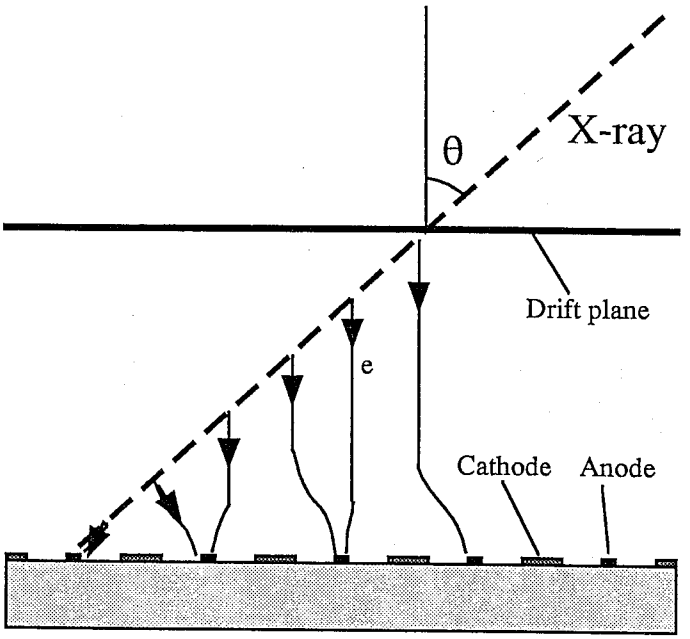

Figure 3.9: Schematic figure for explanation of slant incidence. An incident X-ray which have the slant angle θ is absorbed on the way along the X-ray trajectory in the gas volume.

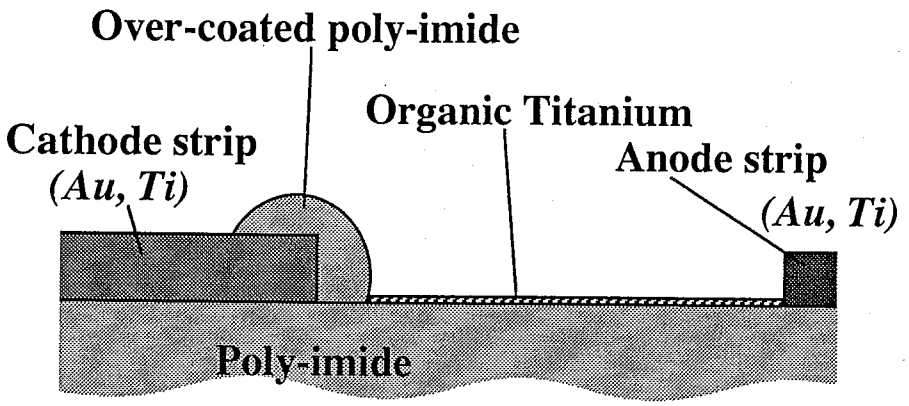

Figure 3.10: Schematic structure of the passivation on the cathode. The edge of the cathode is protected by over-coated poly-imide to avoid discharge.

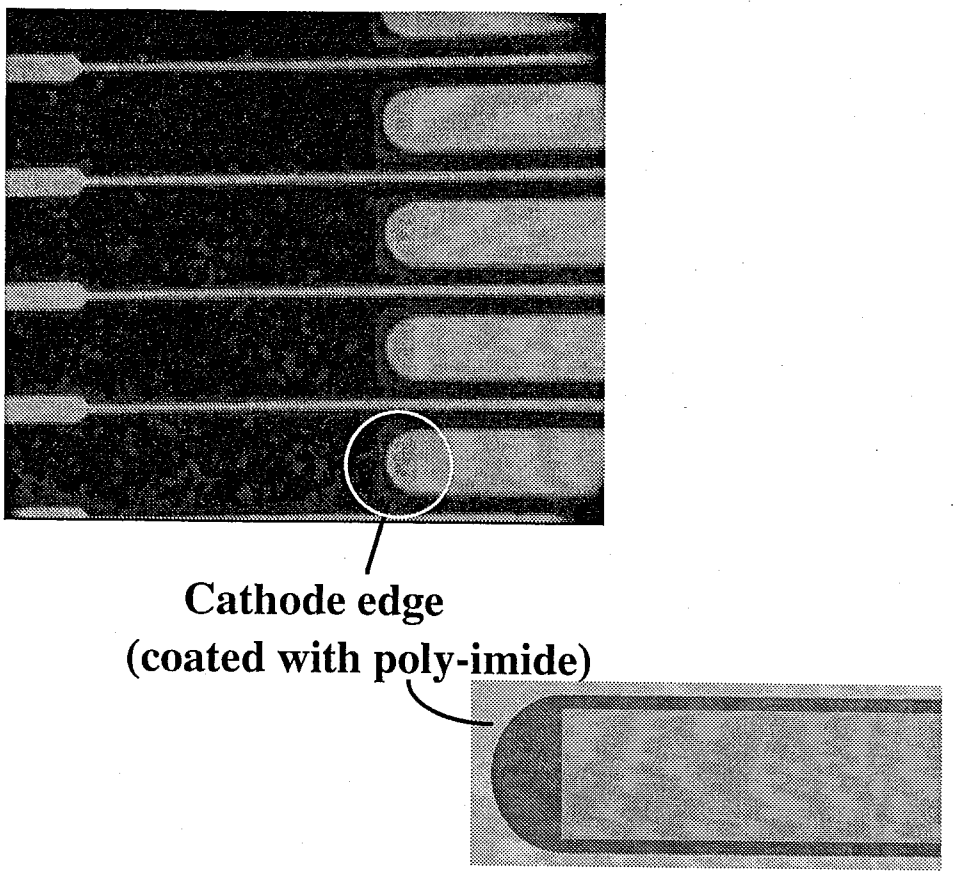

Figure 3.11: Microscope photograph of strips on the MSGC. The edge of the cathode is protected by over-coated polyimide.

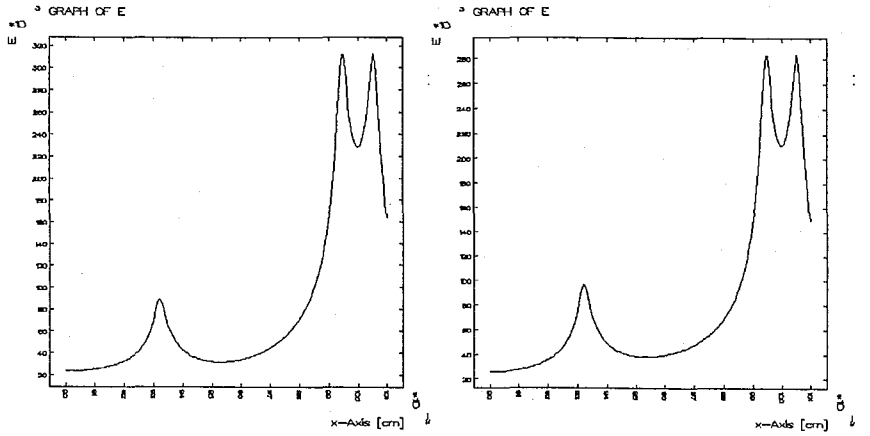

(a) $V_a = 400\text{V}$, $V_c = -100\text{V}$, d=8μm (b) $V_a = 400\text{V}$, $V_c = -100\text{V}$, d=17μm

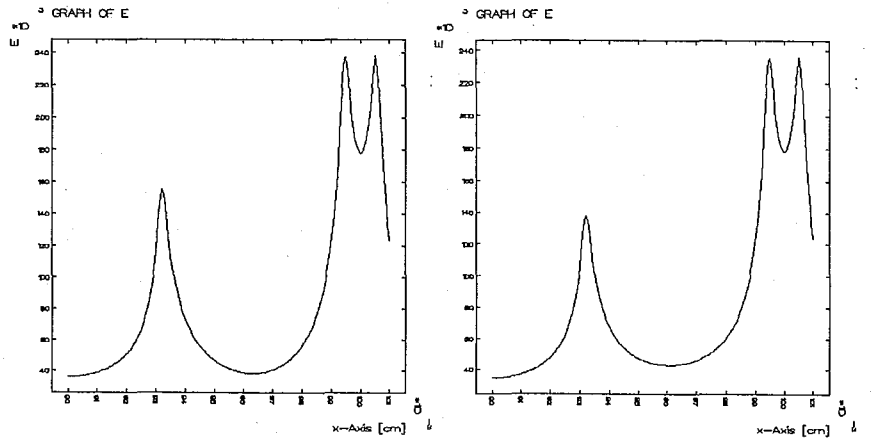

(c) $V_a = 250\text{V}$, $V_c = -250\text{V}$, d=8μm (d) $V_a = 250\text{V}$, $V_c = -250\text{V}$, d=17μm

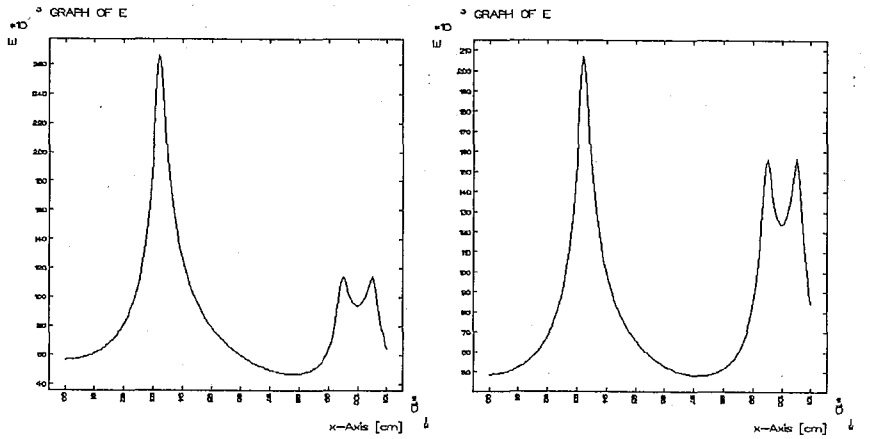

(e) $V_a = 0\text{V}$, $V_c = -500\text{V}$, d=8μm (f) $V_a = 0\text{V}$, $V_c = -500\text{V}$, d=17μm

Figure 3.12: Electric field near the surface of the substrate in different potentials V_a, V_c, and the substrate thickness d.

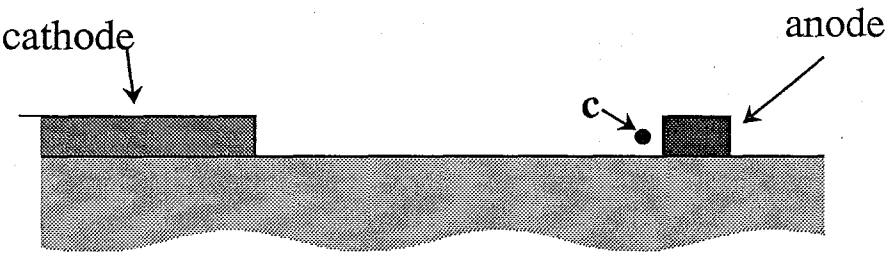

Figure 3.13: Definition of the point for field calculation.

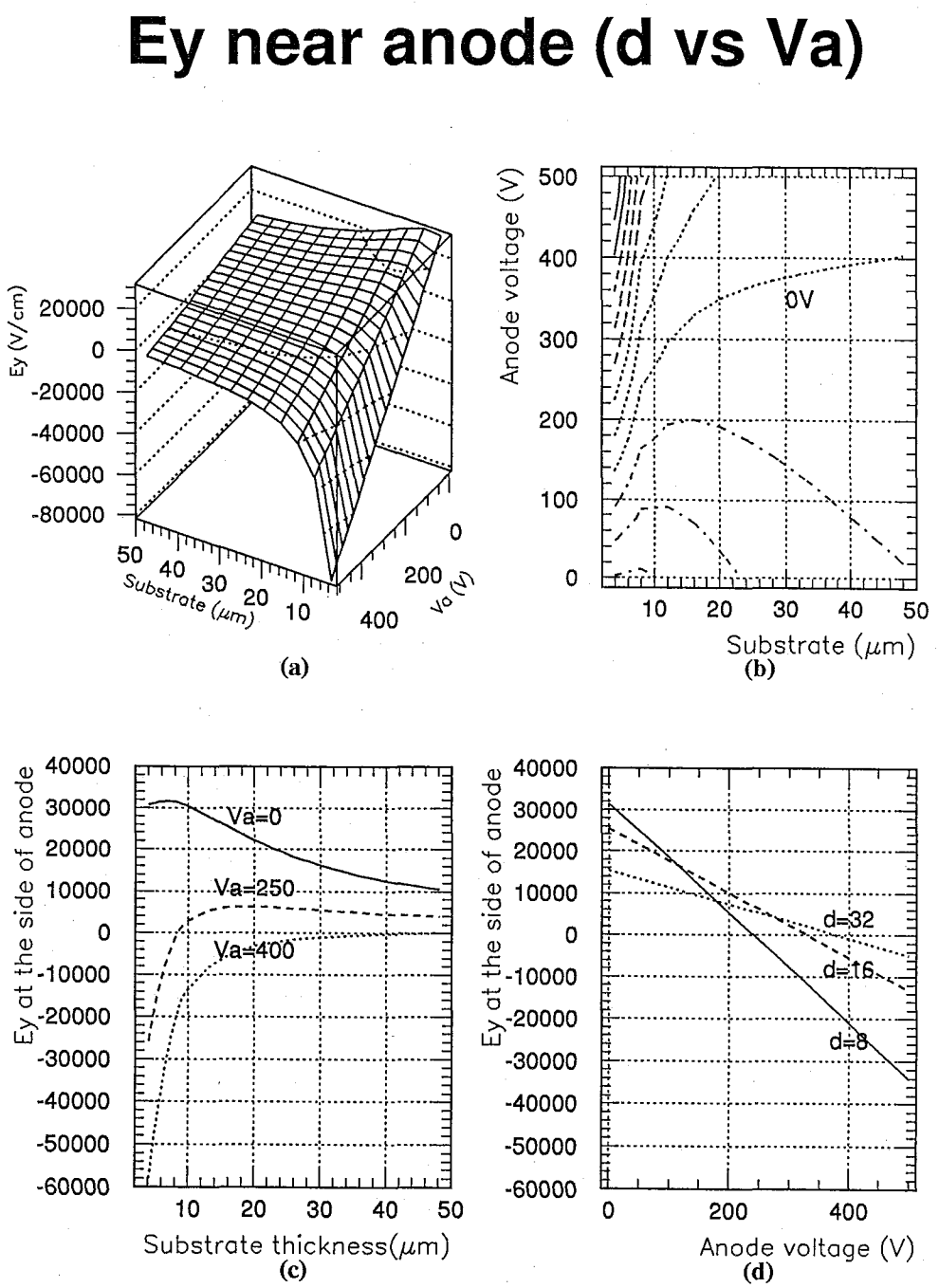

Figure 3.14: Perpendicular component of electric fields. (a): The surface plot of E_y for d and V_a variation. (b): The contour plot for an (a). (c): E_y vs d in cases of $V_a = 0$, 250 and 400V. (d): E_y vs V_a in cases of $d = 8$, 16 and 32μm.

Figure 3.15: Multiplication factor of MSGC for varying the width of anode W_a and that of cathode W_c. (a): The surface plot of gain for W_a and W_c variation. (b): The contour plot for an (a). (c): The gain vs W_c in cases of $W_a = 8\mu$m. (d): The gain vs W_a in cases of $Wc = 63$, 100, 120 and 152μm.

Chapter 4

Performance test

4.1 Two-dimensional readout

The performances of the MSGC have been examined. The type I (5cm × 5cm area) MSGC was mainly used to measure the performance of imaging capability, gain stability, the capability of the operation in the high counting rate, and the energy resolution. The type II (10cm × 10cm area) MSGC were also used to examine the imaging performances for actual applications.

In order to use an MSGC as an X-ray area detector, additional electrodes besides anodes are necessary. There are four types of electrodes on the MSGC: anodes, cathodes, a drift plane, and backstrips. At first, the signals from each electrode (except for a drift plane) were measured. An anode, a group of cathodes and a backstrip on 5cm square MSGC were connected to charge sensitive preamplifiers with charge gain of 800mV/pC and timing constant of 500ns. The outputs of these amplifiers were fed to digital oscilloscope respectively, and these signals were acquired simultaneously. The MSGC was operated under the gas gain of $\sim$ 800, and X-rays from ^{55}Fe (5.9keV) were irradiated. Figure 4.1 shows the pulse shapes obtained from an anode, a group of cathodes, and a backstrip for the same X-ray event. The rise time of the backstrip is very fast of a few ns, and its shape seems to be the residual of the anode pulse subtracted by the cathode pulse of which rise time was seen to be $\sim$200 ns. The typical pulse height induced on the backstrip was small and about one quarter of that of the anode. The cathode has a large induced signal, but the rise time of $\sim$200 ns is fairly slow. Then cathode signal is not suitable for fast readout. The signals from cathodes are summed up and fed to analog readout for measuring energy of incident

X-rays (see section 4.4). Some part of ions generated in avalanches flow to the drift plane and induce signals on it, which are however very slow of several tens μs.

One avalanche generated by an incident X-ray induces signals both on anodes and backstrips. The range of the photoelectrons in argon gas (1atm) is $\sim$ 1mm for 8keV X-rays, and electrons are produced through ionization with a expanse of that range. Therefore, the signals are induced on several anodes and cathodes simultaneously. Observing the position of hit strips and their timings, two dimensional position is obtained. The 5cm square MSGC and the data acquisition system based on CAMAC (see section 5.1) were used for tests of two dimensional readout. The gas gain is set to $\sim$ 300 in this measurement. The number of hit electrodes depends on a threshold charge at which the signals of the strips were discriminated. The threshold level of the backstrips was set to slightly higher charge than that of the noise ($\sim 2 \times 10^{-15}$ C), and the threshold of the anodes was determined such that the number of hit anode and that of hit backstrip are similar. An X-ray tube of copper target ($K_\alpha = 8.0$keV) was used as a source, and X-rays between 7keV and 9keV are selected using the energy information from the cathode strips. The box plot of the numbers of hit on backstrips and hit anodes is shown in Fig. 4.2. Most of all events have less than four hits in both anodes and backstrips. The simple method of getting the hit position as a center gravity of the hit electrodes was proven to provide a good position resolution of less than 100 μm.

To reconstruct a two-dimensional position, the timing coincidence between anode and backstrip signals is needed. The time differences between signals were measured. The timing data from CAMAC timing-digital converters (LeCroy:LRS2277) were used, and time differences between anodes and backstrips were recorded as shown in Fig. 4.3. The observed narrow concentration within 10ns (FWHM) is due to the fast rise time of both anode and backstrip pulses.

4.2 Gain stabilities and performances under high counting rate

The time variation of the gain due to charge-up on the substrate is one of the most important issues to be overcome. From the simulation studies in section 3.4, positive ions generated in an avalanche around the anode were found to smoothly reach the cathode

without crossing the substrate surface when the substrate is thicker than ~14 μm. The time variation of gain was measured using 5cm square MSGCs with substrate thickness of 8μm and 17μm. Figure 4.4(a) shows the time variations of the gain obtained from the MSGC with 17μm thick substrate for various potential ratios of the anode to the cathode (V_{ab}/V_{ac}). It is noted that the gain soon settles down and remains constant for any potential ratios. However, as shown in Fig. 4.4(b), there is no potential configuration for an 8 μm thick substrate to attain the stable operation. This result is reasonably consistent with the result obtained from our computer simulation in section 3.4.

With this improvement, we used an intense X-ray generator as an X-ray source in testing our MSGC, and then the capability of our MSGC for the high counting rate operation was investigated. First, the linearity of the anode current was examined up to a counting rate of $\sim 2 \times 10^7$ Hz/mm^2 at the gain of ~200. In this measurement, fast amplifiers MQS104(τ ~20 ns) developed by LeCroy were used to reduce pile-up effects, and the gain of the MSGC was decreased to $\sim$ 200 taking the high gain of this amplifier into account. As shown in Fig. 4.5, the linearity was found to be kept even at the highest counting rate of 2×10^7 Hz/mm^2. Figure 4.6 shows digital-oscilloscope images of output signals from one anode at different counting rates. Each pulse is clearly distinguished even at such a high counting rate. This is very important to keep in mind when considering how to derive the coordinates of the X-ray under such a high counting rate.

At the counting rate of$\sim 10^7$ Hz/mm^2, time variation of the gain is shown in Fig. 4.7 for one discrimination level (40% of the average pulse height in the low intensity operation). Up to ~1000 seconds, the gain of our MSGC was observed to be constant, and thereafter gradually decreased. From these results, our MSGC appears to be applicable to a high counting operation in intense X-ray sources. Our MSGC is currently being operated for several days under moderate irradiation of radioactive source.

4.3 Imaging performance

Imaging performances were investigated using both the 5cm square and 10cm square MSGCs. At first, X-ray transmission image was measured by 5cm square MSGC. The X-ray tube with copper target was used as an X-ray source. An intensity of X-rays was reduced to $\sim$ 1cps/mm^2 by copper foils, because capabilities of data acquisition were limited. The

gas gain is about 300, and 25mm×26mm area was used for imaging. The CAMAC DAQ system as described in section 5.1 was used. A good example of an X-ray image obtained from MSGC is presented in Fig. 4.8. This is a transmission image of a circuit board having very fine through-holes with a 300μm diameter and a 600μm pitch in line. Each through-hole is clearly separated from the other. Furthermore, note that the printed pattern on the circuit board can also be seen, which indicates that the digital image of X-ray in MSGC allows us to measure the small variation of material density. The enlarged surface plot near the through-holes is shown in Fig 4.9. The position resolution is obtained from this figure to be $\sim$ 100μm.

X-ray diffraction images were also taken with 5cm square MSGC. This measurement was carried out in 6C beam line at KEK Photon Factory (KEK-PF) in December 1996 to verify the ability as an area detector for an X-ray diffraction measurement. Figure 4.10 shows a small angle diffraction pattern of a collagen irradiated by 8.9 keV X-ray beam with a 1 mm square size, and its projection to the axis normal to the beam is also presented in Fig. 4.11. Note that both large peaks and small peaks appear very symmetrically from the beam position, which is an excellent feature of both the fine electrode pitch of the MSGC and the wide dynamic range of the photon counting. Peak widths were determined not from the position resolution of the MSGC but from the beam size of 1 mm. Furthermore, very small peaks around the tail of the large peaks can be clearly distinguished, which shows that the spread function of the MSGC has no halation around diffraction peaks.

The image distortion in the MSGC is also the important performance which has to be measured. X-ray imaging detectors such as an image intensifier or a tapered glass fiber usually suffers from an image distortion, and the calibration of an image is certainly necessary for each experiment. The MSGC has no image distortion in principle. The aim of this measurement is to verify the uniformity of the image on MSGC. The universal printed circuit board with 0.1 inch pitch and 0.8mmϕ holes is used as a calibration pattern, and transmission image was taken by the 10cm square MSGC. An X-ray generator with rotation copper target (K_α: 8.0keV) was used as the source, and X-rays are monochromized by a 10μm thick nickel filter. The obtained image is shown in Fig. 4.12, in which no distortion was found in MSGC. The distortion factor of MSGC was less than 0.5 %, whereas that of fiber coupled CCD is 10%.

The uniformity of the efficiency was also measured. X-rays from the generator with copper target and nickel foil filter (K_α: 8.0keV) was used as the source. The uniformity of the source was calibrated using an imaging plate, and it was formed to be less than 5% in the whole detection area of the MSGC. The type II MSGC was used for this check, and operated at the gain of 200. The experimental results were rather poor as shown in Fig. 4.13(a)~(c). Figure 4.13(a) shows the X-ray image with the threshold level of 50mV, which corresponds to charges of $\sim 1fC$, and Fig. 4.13(b),(c) show that with the level of 46mV and 42mV, respectively. The efficiency should be uniform in principle for digital readout, however these results show the uniformity is not so good. The horizontal stripes of these images are caused from the instability of electronics, and the vertical lines are caused from the dead strips broken by discharges. Uneven images that are independent from the signal lines are also found in these figures, and these inefficiencies are thought to come from the gain difference. The inefficiencies from the gain differences, which is defined as the ratio of the standard deviation of the obtained intensities in the average intensities, are 95%, 65% and 55% for Fig. 4.13(a),(b),(c), respectively. The induced charge on backstrips is estimated to be about 1 $\sim$ 2fC for 6keV, and the charge on one backstrip is equal or less than 1fC in the gas gain of 200. These induced charges are near the lower limit of the threshold level, and the non-uniformity of the gain is emphasized in the image. For $>$ 10keV X-rays, the non-uniformity problem is small because induced signals are large enough to exceed the threshold level. It is thought that the difference of the gain is due to the non-uniformity of the substrate thickness. The multiplication factor of MSGC is strongly dependent on the substrate thickness for less than 20μm as shown in Fig. 3.15 of section 3.4. Therefore we have to develop MSGC operated stably at higher gain.

4.4 Energy spectrum

In our MSGC, all signal of the anodes and the backstrips are discriminated by one threshold level, and pulse height information is lost. However, energy information of an X-ray is obtained from cathodes. Summed cathode signals are amplifiered and fed to an ADC (Analogue to Digital Converter). Figure 4.14 shows the energy spectrum of ^{55}Fe 5.9keV X-ray thus obtained. The energy resolution is about 13% (RMS), and the escape peak is also seen clearly.

The energy resolution of the MSGC is not good enough to use it for spectroscopy, but the combination of the imaging capacity and the energy measurement makes possible to take an X-ray image like a color photograph. For example, the MSGC will enable us to measure the energy of each diffraction spot in the Laue method taken under white X-rays. The test of this "energy resolved Laue method" was made to study the capability of MSGC as a spectroscopic imaging detector. An X-ray tube with copper target without any filter was used as a source. The 5cm square MSGC and the CAMAC data acquisition system (section 5.1) with ADC were used. A monolithic crystal of Phenothiazine-Benzilic acid complex was used as the diffraction sample. Figure 4.15 shows sample of Laue picture taken in this measurement. Fig. 4.16 shows the pulse height distributions for (A)~(D) spots on Fig. 4.15 (solid lines), and those for the same spots when a sample was absent (dashed lines). The shapes of dashed lines correspond to the spectrum of the source X-rays. You can see that the center values of the distributions are clearly different for each spot. This result shows that the new dimension of data will be provided besides the imaging data. In this method, the reciprocal lattice will be observed directly.

The measured performances of the MSGC are summarized as follows:

Operational gain	$200 \sim 800$
Energy resolution	13 % (RMS) at 5.9keV and gain $\simeq$ 500
Spatial resolution	100μm at 8.0keV (RMS)
Maximum rating	2×10^7cps/mm^2
Image distortion	$< 0.5\%$
Uniformity	$\sim 50\%$ at $\sim$ 1pC threshold for backstrips

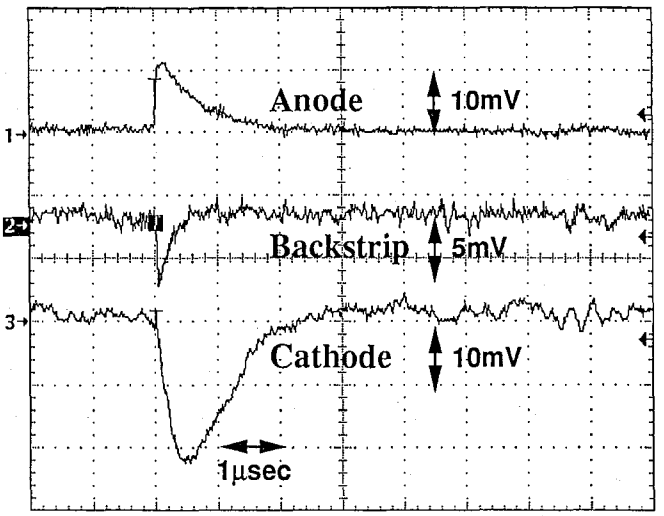

Figure 4.1: Oscilloscope image of pulse shapes obtained from an anode, a group of cathodes, and a backstrip for the same X-ray event, respectively. The fall time of the pulse is due to the time constant of the preamplifier of 500ns.

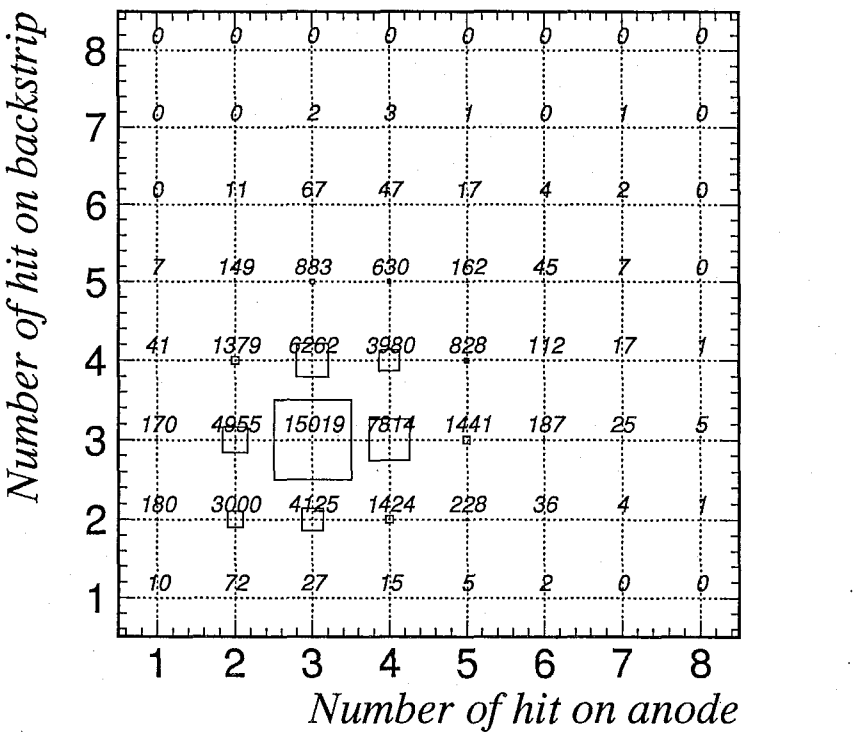

Figure 4.2: Plot of the number of hit backstrips vs. that of anodes.

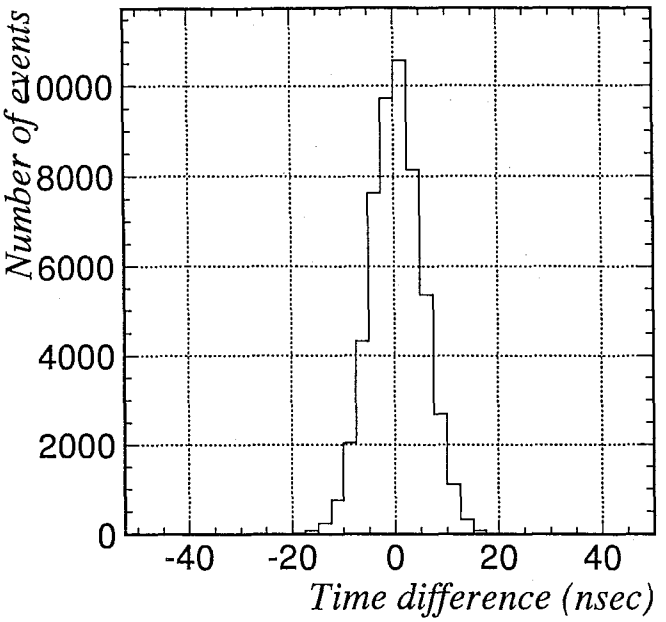

Figure 4.3: Distribution of the time difference between an anode pulse and a cathode pulse measured by time-digital converter.

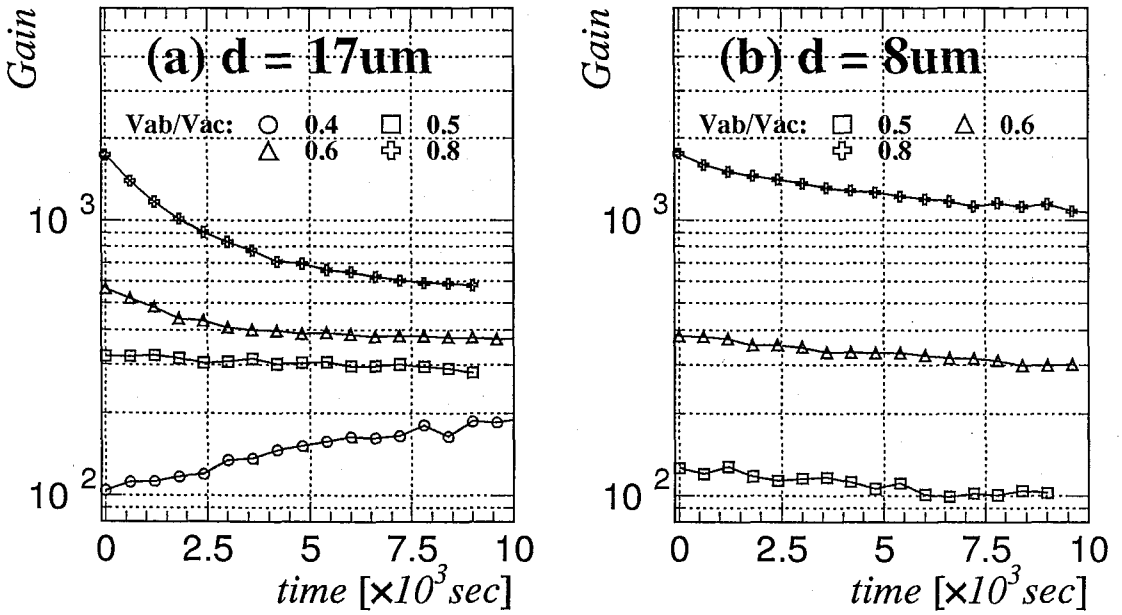

Figure 4.4: Time variations of gains obtained from MSGCs of (a) a 17μm thick substrate at various potential ratios of the anode to the cathode (V_{ab}/V_{ac})

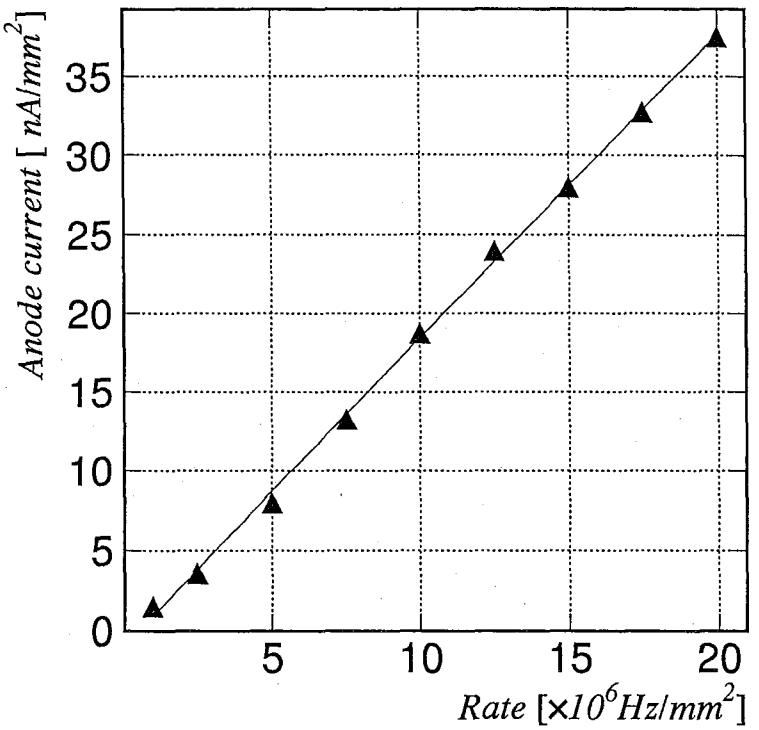

Figure 4.5: Anode current as a function of the intensity of X-rays.

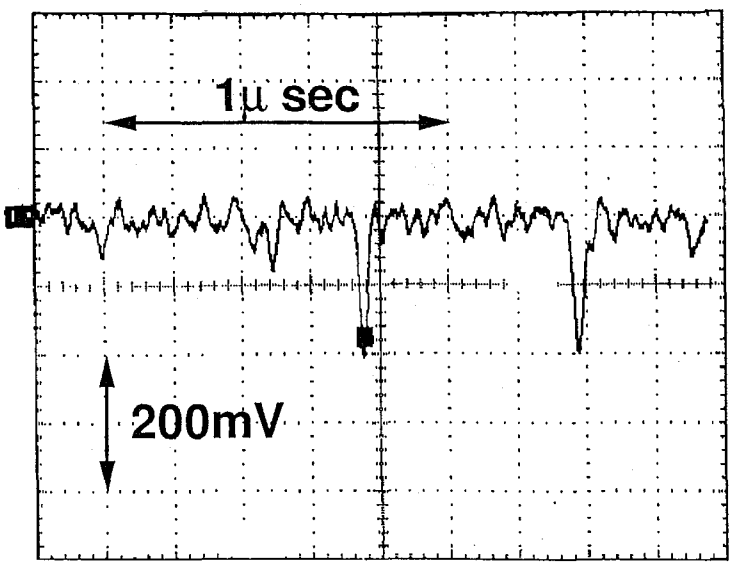

(a) Rate = ~2×10^{6}mm^{-2} sec^{-1}

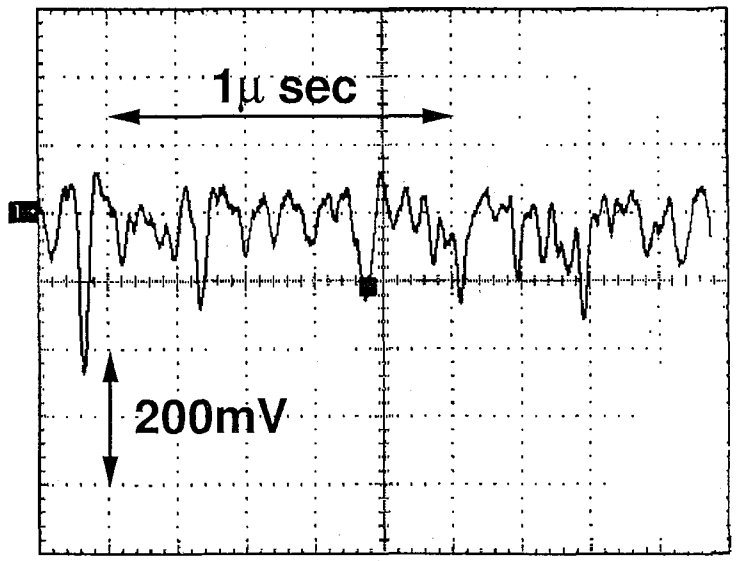

(b) Rate = ~10^{7}mm^{-2} sec^{-1}

Figure 4.6: Digital oscilloscope images for output signals from an anode of the MSGC at a counting rate of (a) 2×10^6Hz/mm^2 and (b) $\sim 10^7$Hz/mm^2

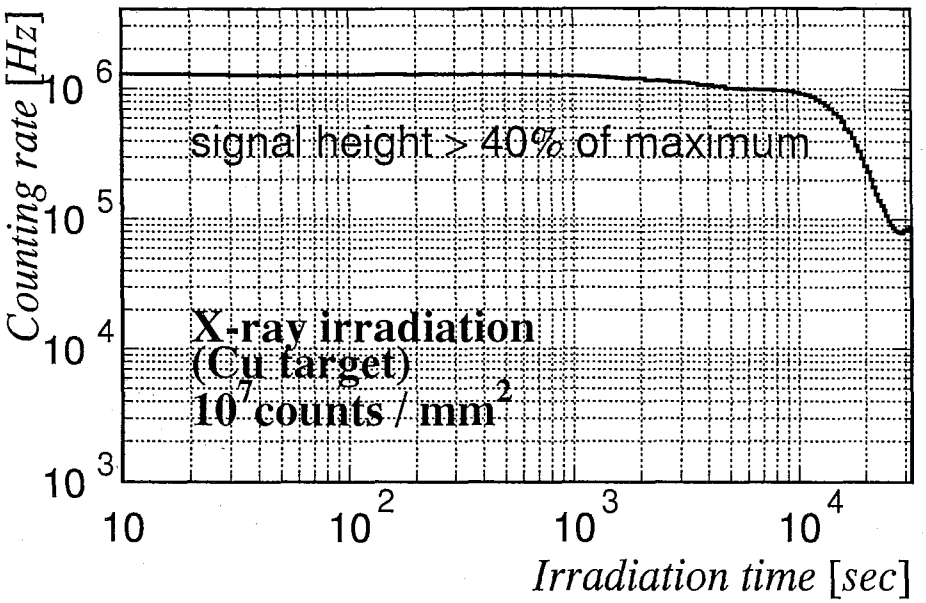

Figure 4.7: Time variation of the gain under a high counting rate of $\sim 10^7$Hz/mm^2 at one discrimination level (40% of the averaged pulse height in the low intensity operation).

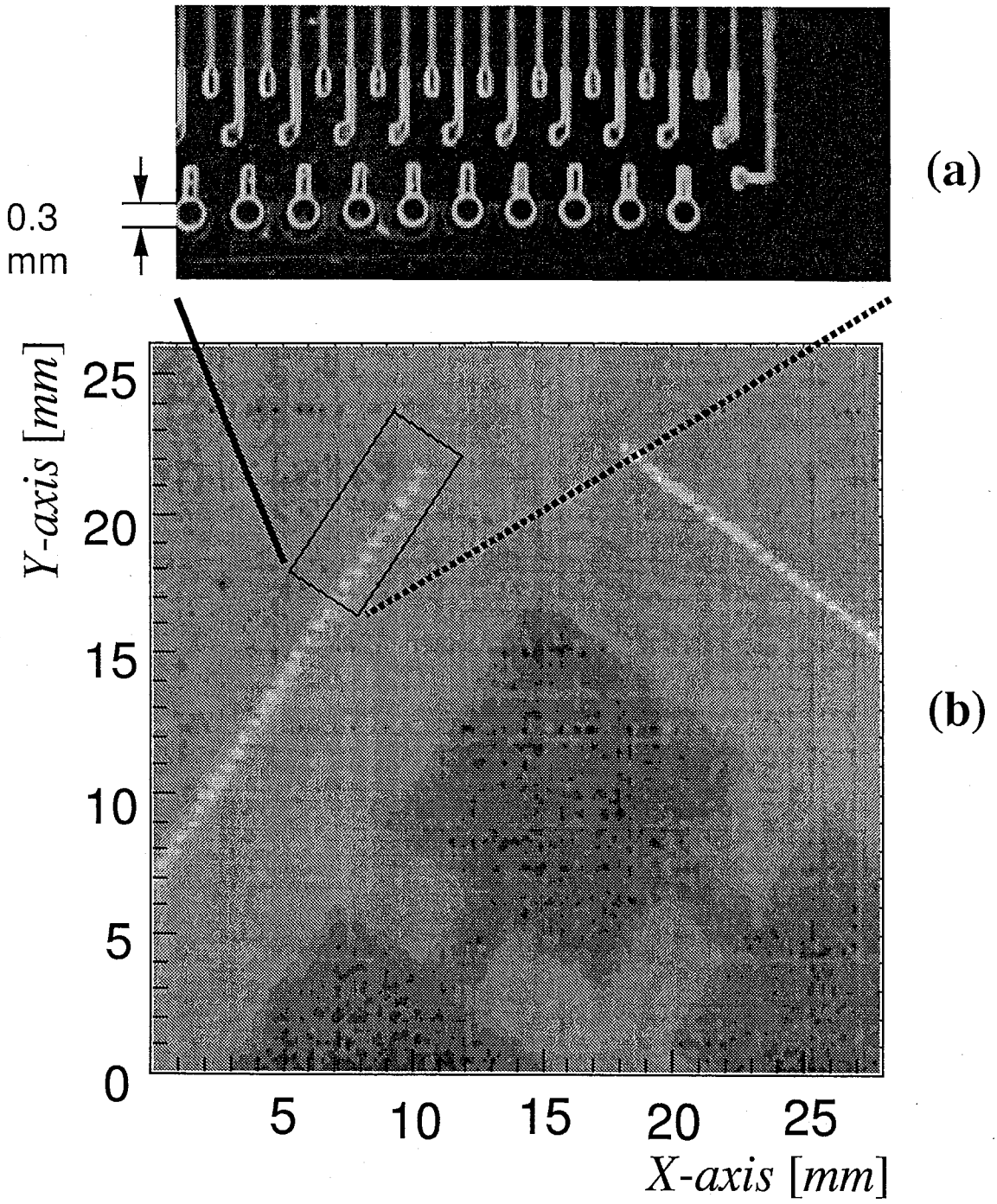

Figure 4.8: (a): Enlarged picture of the bonding part of the circuit board, on which large area MSGC will be directly mounted by bonding technique, in which very fine through-holes with 300 μm diameter and a 600 μm pitch are formed in line. (b): Transmission image for this board, where images of both fine through-holes, and printed pattern are clearly seen.

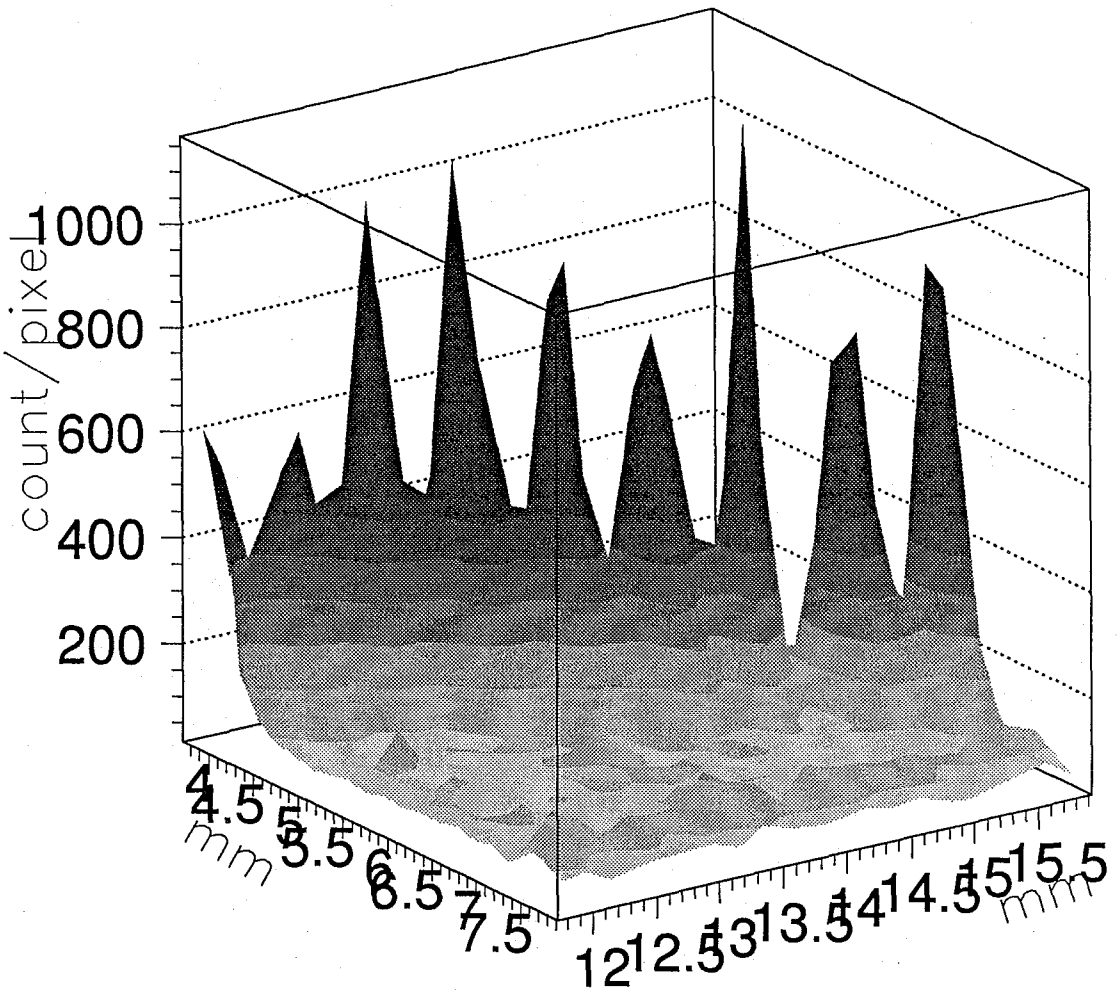

Figure 4.9: Enlarged surface plot near the through hole image. The image of holes is well separated each other, and this image corresponds to the RMS position resolution of 100μm.

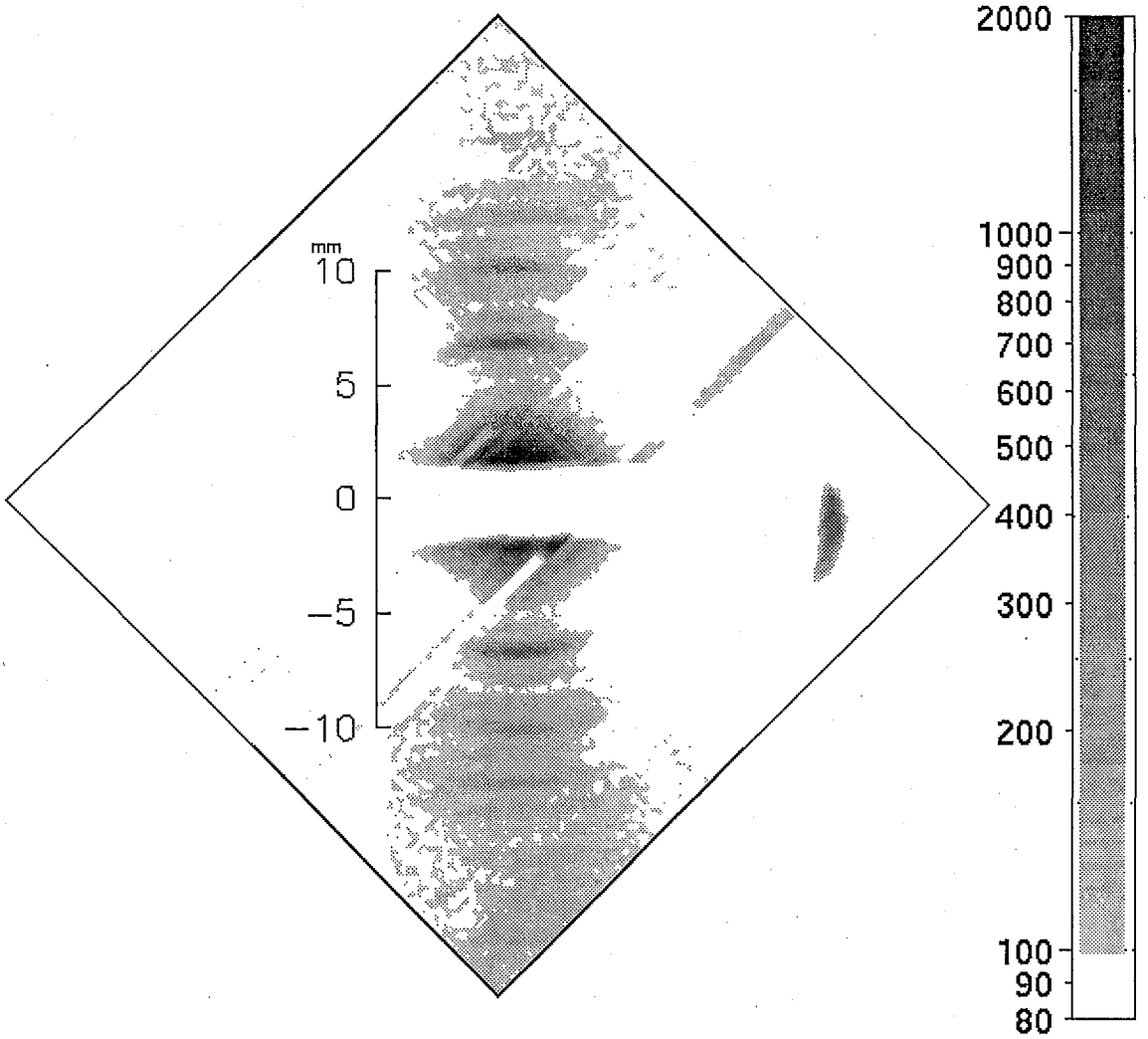

Figure 4.10: Small angle diffraction image of a collagen.

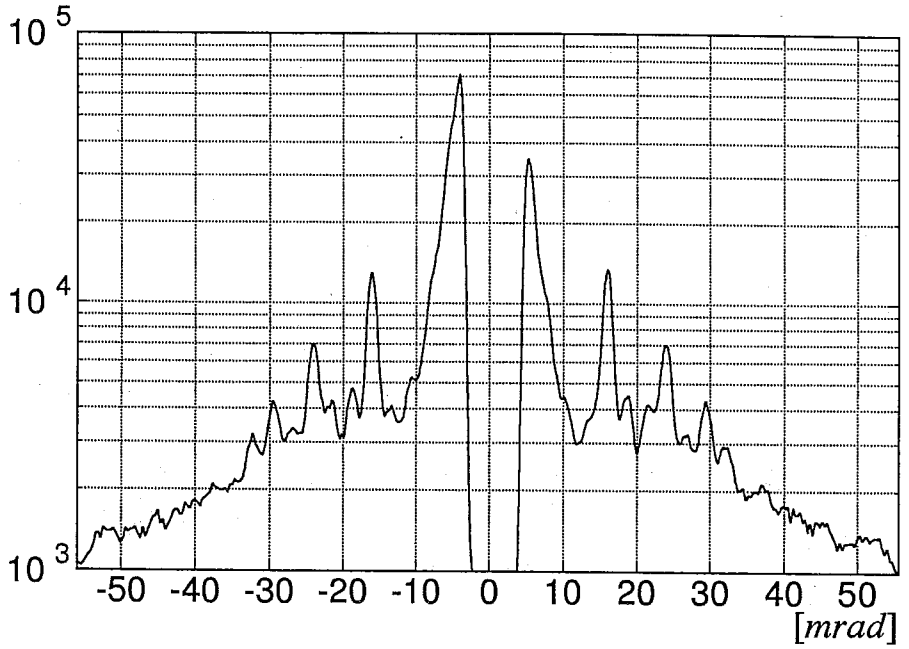

Figure 4.11: Projection of the small angle diffraction image of the collagen.

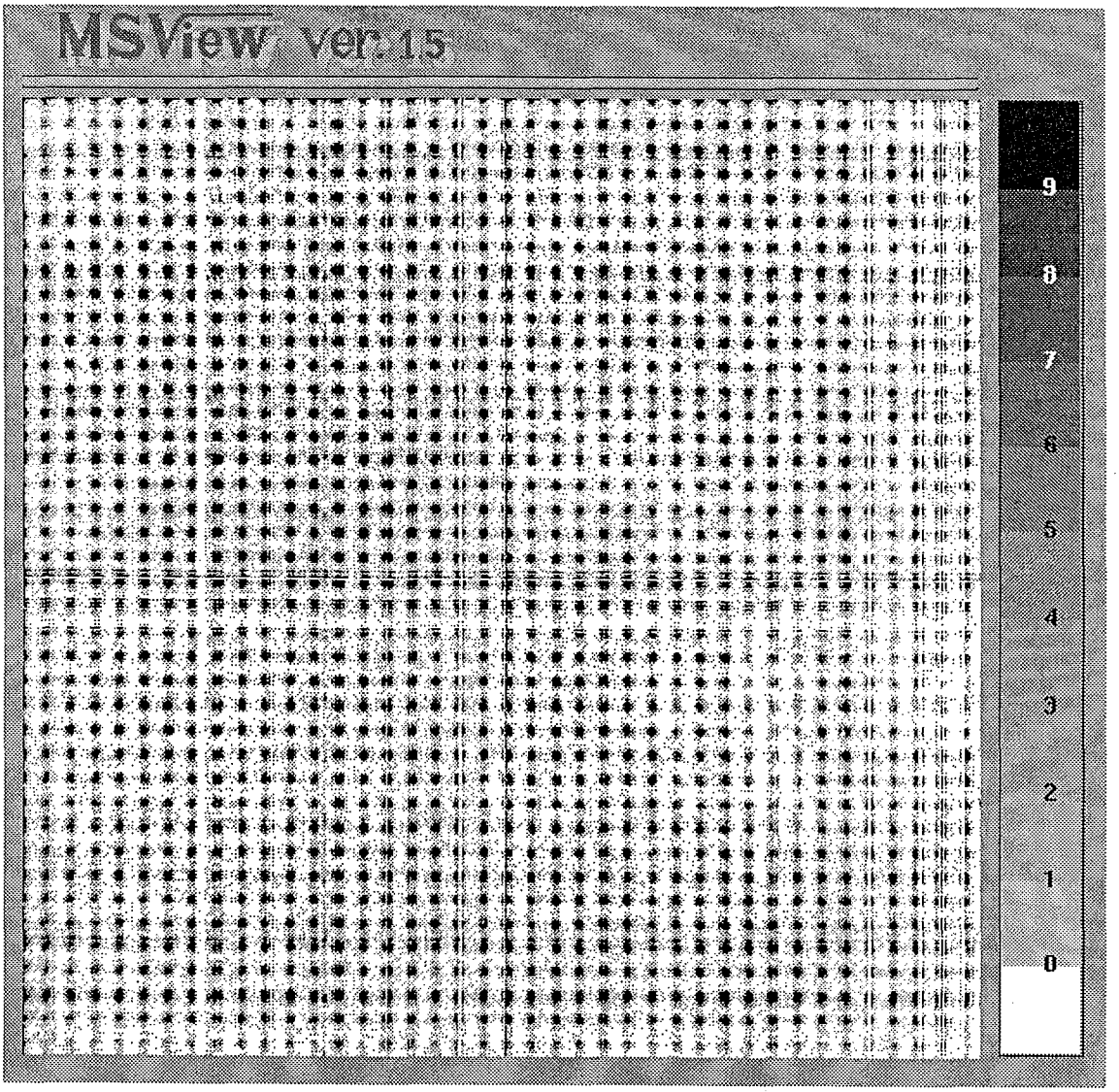

Figure 4.12: Transmission image of universal printed circuit board with 0.1 inch pitch. No distortion is observed from this figure.

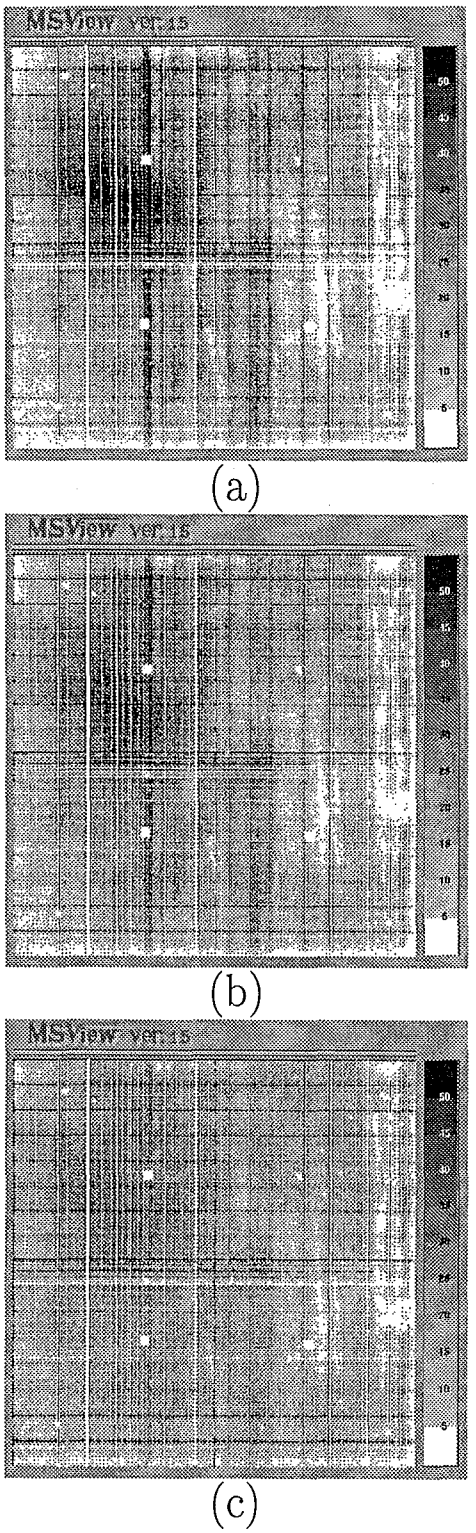

Figure 4.13: Images obtained from MSGC for uniform X-rays irradiation. The threshold voltage was set at (a) 50mV, (b) 46mV, and (c) 42mV.

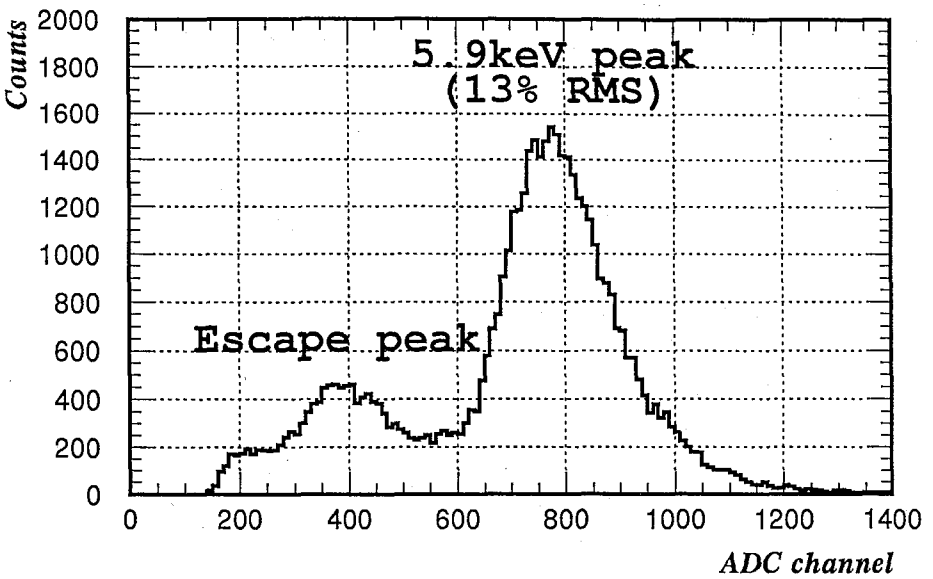

Figure 4.14: Energy spectrum of ^{55}Fe 5.9keV X-ray obtained from the cathode of the MSGC.

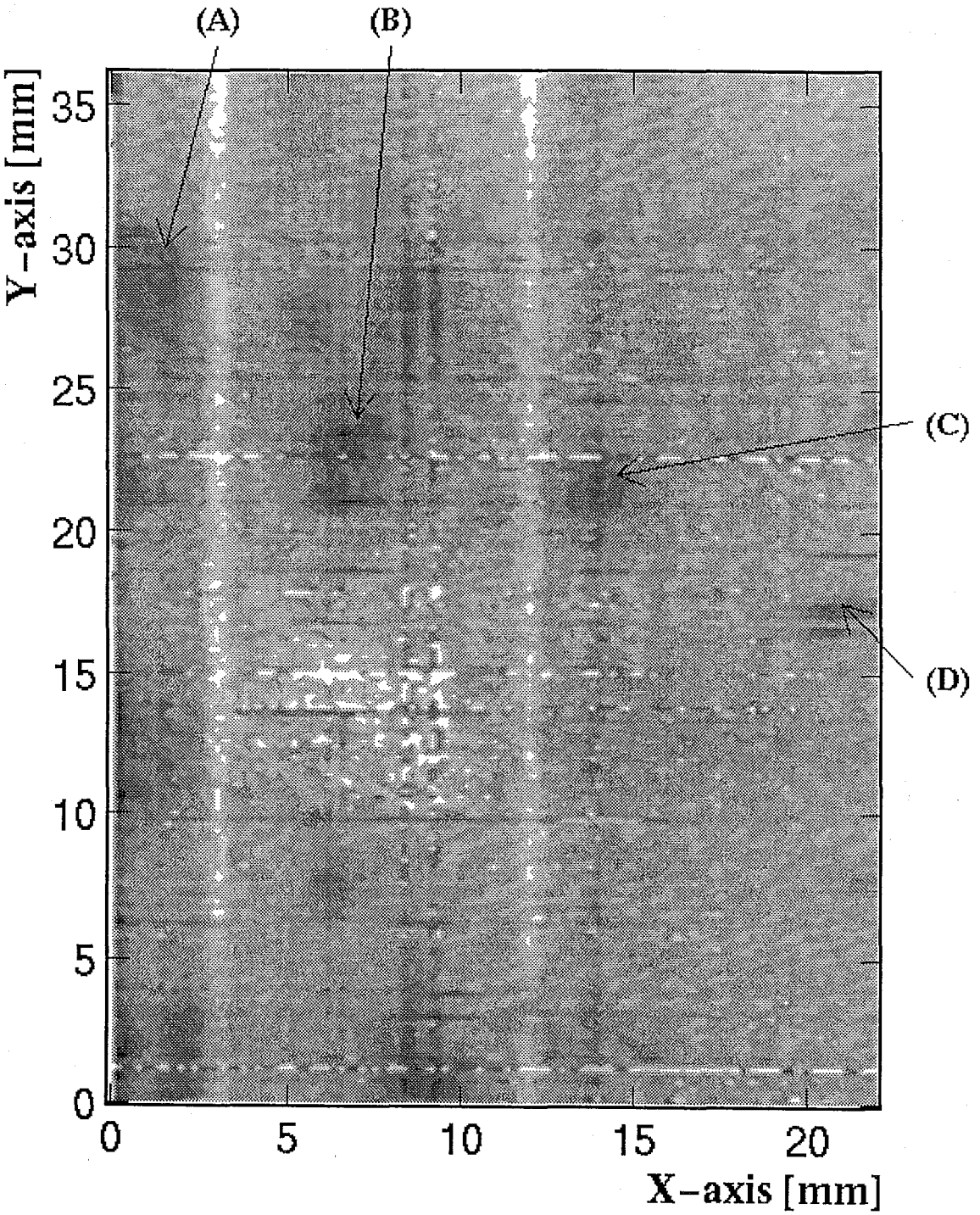

Figure 4.15: Laue photograph using the MSGC. (A)~(D) are the Laue spots whose energies were measured as shown in Fig. 4.16.

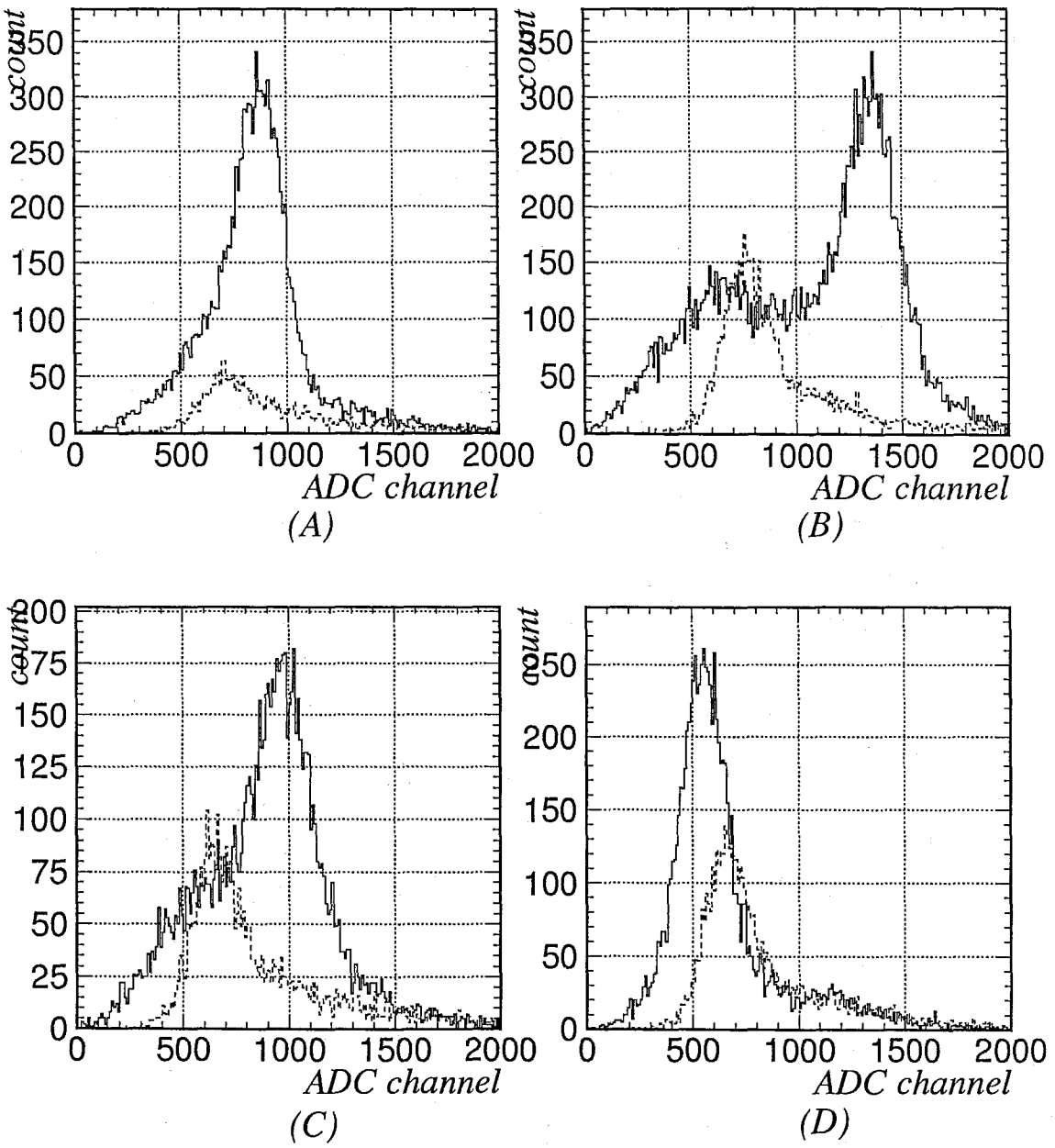

Figure 4.16: Pulse height distribution for each spot on Laue photograph on Fig. 4.15 (solid line) and the distribution when a sample was absent (dashed line).

Chapter 5

Fast data acquisition system

5.1 DAQ based on CAMAC system

One of the most serious problems for the MSGC operation under intense X-rays is the limitation of the capability of the data acquisition (DAQ). At first, the DAQ system used in the early stage of the development, which was based on CAMAC system, is explained, and secondly, an ultra fast DAQ system developed that enables us the real-time X-rays measurements are described.

The read-out system for type I (5cm × 5cm) MSGC consists of pre-amplifier cards, discriminator boards, multi-hit CAMAC TDCs (Time to Digital Converters: LeCroy 2277 and 3377), and an UNIX workstation for the data acquisition from the CAMAC system. The block diagram of this readout system is shown in Fig. 5.1. A charge integrated pre-amplifier with a time constant of 500 ns was designed using the LeCroy TRA1000 monolithic amplifier chip. Figure 5.2 shows the circuit diagram for one channel of this amplifier. A feed back capacitor is 1pF, and the effective charge gain is 800mV/pC. Each pre-amplifier card contains 16 amplifiers. As a main-amplifier and discriminator system, we used the system developed at KEK (High Energy Accelerator Research Organization) as a part of the drift-chamber readout system that includes a fast current amplifier and discriminator. The discriminated pulses were fed to CAMAC multi-hit TDCs. The distribution of the timing difference between an anode pulse and a backstrip pulse measured by this TDC system is shown in Figure 4.3 in chapter 4. The narrow concentration within $\sim$ 10ns at full width half maximum is due to the fast rise time of both pulses. Using this good timing coincidence, accidental and electrical noises were completely removed in reconstructing an

image. The sum of cathode signals is used not only as a trigger, but also for the pulse height measurement. This signal is amplifiered by a shaping amplifier (ORTEC 450) with 1μs of shaping time, and fed to CAMAC ADC module. The position and energy of each X-ray event are recorded in this system.

This system is based on the same technology used in high energy physics experiments. The component of this system is provided commercially except for the pre-amplifiers. Then, it is not optimized for MSGC readout. To handle all the signals of 5cm square MSGC, we need 33 pre-amplifier cards, 16 discriminator boards, 16 CAMAC TDC modules, several NIM standard modules (for generating trigger signal), one VME crate to connect the workstation and the CAMAC system, and a lot of cables. As all the timing data of hit strips were recorded by the computer via CAMAC bus, the data acquisition rate was restricted by the data transfer rate. The access time from the computer to a CAMAC module is about 30μs, and the number of access to the CAMAC in one X-ray event is about 40 $\sim$ 60 times (the number of CAMAC modules [$\sim$ 16] + (number of hit strips)$\times$2 [20 $\sim$ 40] + access to ADC and control modules). Therefore, about 1.5ms was necessary for taking one X-ray event, and data acquisition rate is restricted only up to several hundred counts per second.

In order to achieve a faster data acquisition rate, we used a CAMAC auxiliary crate controller (ACC: kinetic 3976-Z2A) having CPU (MC68030 40MHz) and memories (4Mbyte). The block diagram of this module is shown in Fig. 5.3(b). The access time from the ACC to a CAMAC module is improved to a few μs, which depends on the programming on the ACC, and data transfer rate from the ACC to the workstation was achieved to be 150 kbyte/sec at the fastest data transfer mode. By this improvement, the data acquisition rate of $\sim$1k events/sec was obtained. The real-time X-ray analysis, however, requires more than 1000 times faster than this data acquisition system.

5.2 Ultra fast DAQ system

Figure 5.4 shows the block diagram of the new DAQ system. For this new system, not only the ability of handling data of Mega events/s, but also the compactness of the system are required for the X-ray imaging analysis. Whole DAQ system consists of 16 pre-amplifiers cards, four Position Encoding Modules (PEM), one Control and Memory Module (CMM), and one CPU board.

Pulses from anodes and backstrips of MSGC are amplified by fast shaping-amplifiers (LeCroy MQS104A) and discriminated by monolithic comparators (LeCroy MVL407S) on the cards inserted vertically on the MSGC board. The schematic circuit diagram is shown in Fig. 5.5. One MQS104A has 4 channels of charge integrated preamplifiers with 0.2pF feedback capacitor and a shaping amplifier with 20ns timing constant. They have differential outputs and charge gain of $\sim$ 20mV/fC. Figure 4.6 in chapter 4 shows digital-oscilloscope images of signals of one anode at the MQS104A output at the counting rate of a few MHz per one anode. Each pulse width is $\sim$ 30ns and clearly distinguished. The outputs from MQS104A are connected to one of the differential inputs of the discriminators via AC coupling. The threshold voltage of the discriminators is supplied to the other side of the differential input as a bias voltage as shown in Fig. 5.5. The outputs of discriminators are differential ECL standard. Sixteen sets of MQS104A and MVL407S (corresponding to 64 channels) are mounted on both the front and the rear sides of the printed circuit board. In order to handle lots of signal lines in the same space of the printed board, the technology of 8 layer circuit board was used. A photograph of the pre-amplifier card is shown in Fig. 5.6. The size of this card is 135mm$\times$147mm and the thickness is 15mm (including connectors for the output). For reading 1024 of anode- and back-strips, 16 pre-amplifier cards are needed. The MSGC with these pre-amplifier cards is shown in Fig. 5.7. All of these signals from anode- and back-strips are processed as one bit digital data for one electrode, in which only hit or no-hit is recorded.

As pointed out in section 4.1, the fast and narrow pulses of both anodes and backstrips provide very sharp timing coincidence between anodes and backstrips within $\sim$10ns. This means that the two coordinates of a hit point can be synchronously encoded from the MSGC with a few ten ns clock cycles by requiring coincidence in the timings of both anodes and backstrips. This procedure enables us to encode more than 10^7 events per second, which is ten times superior to the ability of the conventional delay-line method. This procedure is still insufficient to make the most of the capability of MSGCs. The MSGC continuously generates data of a few ten Mbyte/s when operating at $\sim$ 10 MHz, in which the transfer rate from the MSGC to the computer reaches the limit manageable by the present computer technology. Most of the events produce less than three or four hits on both anodes and backstrips. The simple method of getting the hit position as a center gravity of the hit

electrodes was proved to provide a position resolution of 100 μm. This resolution reaches near the limit due to the diffusion of drift electrons as described in section 3.3. Therefore, we need to record only the positions of the hit anodes and backstrips instead of the pulse heights of those electrodes.

We have developed a synchronous encoding system based on the above strategy. This system consists of 9-U VME modules of two types. One is the position encoding module (PEM) which has 256 inputs and three Complex Programmable Logic Devices (CPLD). The PEM encodes hit strips of X or Y coordinates. The other is the control and memory module (CMM) which has a large buffer memory of 512Mbyte for keeping the image data during ~10 seconds at the counting rate of 10^7 events/s, and generates the synchronous clock.

Four PEMs encode 1024 data of electrodes from the 10cm square MSGC into the 20 bit data of the position. The PEM is the most significant part for the fast DAQ, in which all data have to be processed by digital hardwares including such process as the noise reduction and the calculation of the arithmetic centroid of the cluster of hit electrodes. One PEM handles 256 electrodes from the MSGC, then four modules were needed for the 10cm square MSGC. These PEMs and CMM are designed on the basis of VME-9U (Versa Module European - 9 Units) standard architecture. Figure 5.8 shows the two PEM modules and the CMM module. The physical size of these boards is mainly determined by the number of connectors, for data inputs. This system would be smaller if more high density cables and connectors were available. Figure 5.9 shows the block diagram of the PEM. The ECL-differential inputs are translated to TTL standard, and fed to the encode logic that consists of several CPLDs. In one PEM, two EPM7256E and one EPM7192E (Altera Corp.) are used. These CPLDs have a large number of I/O pins (160 pins are available in EPM7256E), and it is very useful to deal with a lot of inputs.

The first stage of the signal processing is a synchronization of the input data with a system-clock cycle. The signals from pre-amplifier cards of which width is about 20 ns, are fed to the inputs of the PEM. Figure 5.10 shows the circuit diagram of synchronizing circuit and timing chart. In order to hold input signals, the input A are processed as clock inputs of D-type flip-flop, and the edges of the pulses are recognized. To synchronize them with the system clock, the output of the first flip-flop B is latched in the next flip-flop

D, and then the first one is cleared by signal C. The one of the most serious problems for synchronization is the timing decision whether the input pulse are to be held before or after the clock. Several input pulses from the MSGC have time jitter of a few ns at one event, therefore, it is not clear whether these hits belong to one event or two events to cross over a clock edge. For avoiding this uncertainty, the signals which are recognized in flip-flop within ten ns from the first signal arrival are decided as the component of one event. Although there exist dead time of 10 ns in one clock cycle, parasitic events are perfectly rejected.

At the second stage, the positions of hit electrodes are encoded synchronously. A few sequential strips of MSGC are usually hit for one incident X-ray. The position of an incident X-ray is decided as a center of these hit electrodes. The highest and the lowest positions of hit electrodes are calculated by a priority encoder, and they are averaged arithmetically to get the center. However, a huge priority encoder to handle several hundreds inputs would be very complex circuit system and would need a long processing time. In this system, it is taken account that the signals from MSGC are induced on several neighboring strips for valid event. As shown in the schematic diagram of Fig. 5.11, the outputs of lower bit and upper bit are calculated independently and simultaneously. The processing between these upper bit and lower bit are taken into account at the final stage of this logic.

The validity of signals is also checked in this circuit as follows. An event that has only one cluster of sequential hit electrodes is decided as a valid event, and the event having two or more clusters is rejected as a noisy or an accidental event. These encoding and validity checks are processed sequentially by a pipeline method in which one function is carried out in one clock cycle. This position-encoding circuit consists of five logical steps, and each step processes another event simultaneously. Therefore the capability of data processing is one event per one clock. Now, this system is operated at 10MHz clock cycle.

The encoded data from the PEMs are fed to the CMM board via J3 VME-bus that is definable by users. A schematic diagram of the CMM is shown in Fig. 5.12. Two PEMs (512ch) handle the anode signals, and the other two PEMs do the backstrip signals. The roles of the CMM are data accumulation from the PEMs, final validity check of a signal by the coincidence of anodes and backstrips, and interface to the CPU. The validity of the data is carried out such that only one cluster from anode PEMs and other one cluster from

backstrip PEMs have to be fed in one clock cycle. The validity (ACCEPT) is actually judged as the following logical formula:

$$\texttt{ACCEPT} = ((\texttt{AHIT1} \oplus \texttt{AHIT2}) \cdot (\texttt{AHIT1} \oplus \texttt{AHIT2})) \cdot \overline{\texttt{DUP}} \quad ,$$

where, event signals from the four encoder boards (two manage the anodes, and two others manage the backstrips) are AHIT1, AHIT2, BHIT1 and BHIT2, and DUP is set when more than one clusters are detected in anodes or backstrips. The accepted signals are accumulated in the storage memory of the CMM. In the CMM, the maximum memories of 512M byte are available, and these memories can be accessed from the CPU board through VME bus. Data of one event consists of x, y position (20bit), timing of data input (4bit), and energy information of an incident X-ray from ADC (8bit). Therefore, total 32bit (4byte) are used in one event, and 128M events are kept temporally.

The CPU board controls the encoding system, and transfers the data to other computers via a network. FORCE CPU-5V on which the microSPARC (110MHz) CPU is mounted is used because of the compatibility with UNIX workstations. In the VME system, the memories on the CMM can be accessed from the CPU via J1 bus of VME crate similarly to the internal memory of the CPU. In this way, the data from the MSGC is transferred immediately to the CPU. In this CPU, data were recorded on the hard disk. The power of the CPU and transfer speed to the hard disk restricts the performance of the MSGC for compiling images. Recently developed 64bit CPU enables to picture real-time movies, but such high performance CPUs are not still available in a VME on-board type. It is also possible that a main data analysis is done by an external CPU by linking it through powerful network faculty of UNIX. A faster data processing is available in an external fast CPU.

5.3 Performance of new DAQ system

In order to evaluate the performance of the new DAQ system, the image and sequential images of a moving object were obtained using the 5cm square MSGC under intense X-rays. The fast data acquisition system is also usable for the 5cm square type MSGC with adapters that interface the connector of 10cm square type MSGC. A half of the DAQ system (two PEM modules: 512 channels are used) was connected to the MSGC in this test. In all of

these measurements, X-rays from the copper target tube were used. The tube voltage was 20 kV, and the intensities of X-rays were controlled by varying tube current (2 mA $\sim$ 30 mA) and by inserting beam dampers made of 100 μm copper foil. The relative intensity of X-rays was monitored by the counting rate of the MSGC itself at low intensity. At high intensity, the source intensity was estimated by extrapolation using the relation between the thickness of damper and the tube current of generator. X-rays from the generator were scattered to the region of 1 msrad. This solid angle corresponds to the spot size of 12cm diameter at 1 meter distance from the generator.

Figure 5.13 plots the number of events that was handled by the DAQ system versus the intensity of X-rays. The event rate handled by the DAQ increases linearly up to 1Mcps, and gradually saturates at ~3Mcps. The maximum number achieved was 3.2Mcps. This system has a capability for processing 10M events per second for synchronous events. However, X-rays usually comes randomly, and the duplication hits within one cycle degrades its capability. The number of events in one cycle follows the Poisson distribution. One and only one hit is defined as a valid event. Therefore, the expected data acquisition rate (defined as R) is calculated by the following formula:

$$R(r) = r \cdot e^{-r/c} \quad ,$$

where, r is a pulse counting rate in an MSGC that is proportional to the intensity of X-rays, and c is a clock cycle. The maximum value of $R(r)$ is c/e at $r = c$, then about 3.7Mcps is the theoretical limit for this system. Our result is consistent to this limit.

Figure 5.14(a) shows the transmission image of a small metal pendant obtained using the MSGC and the DAQ system. The exposure time was about 8 second, and 590 k events of X-rays are taken. The same image in the same exposure time using the old system is also shown in a Fig. 5.14(b) for comparison. Only 1000 events are taken for an image formation. The position resolution of this measurement is about 100μm. The most minute structure of pendant ($\sim$ 200μm) is observed clearly in this figure.

Imaging performance for a moving object is tested with transmission images of the rotating metal pendant. The rotation speed is about 1 round/second. X-rays of 1.3Mcps intensity is used for this measurement. Figure 5.15 shows snap shots for each 25ms acquisition time. By displaying these series of images continuously, a moving picture with X-rays is available. The data from this system contains a time stamp of micro-second or-

der. Using the timing of each photon, X-ray imaging with sub-milli-second is possible, and furthermore, micro-second order imaging would be possible for periodical or reproducible phenomenon.

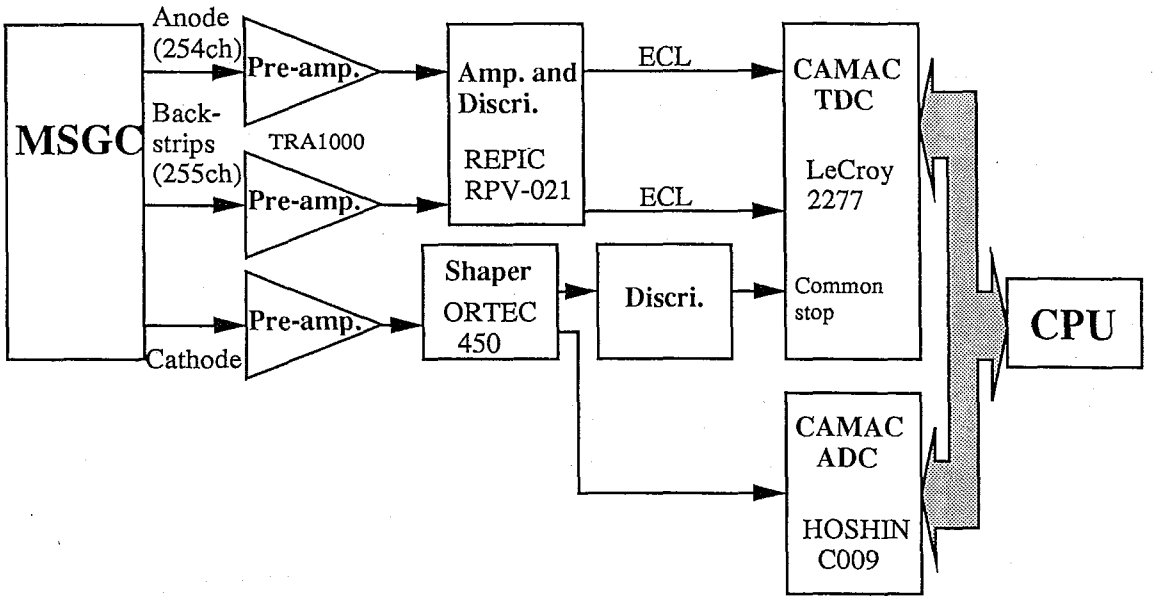

Figure 5.1: Block diagram of the readout system with CAMAC system.

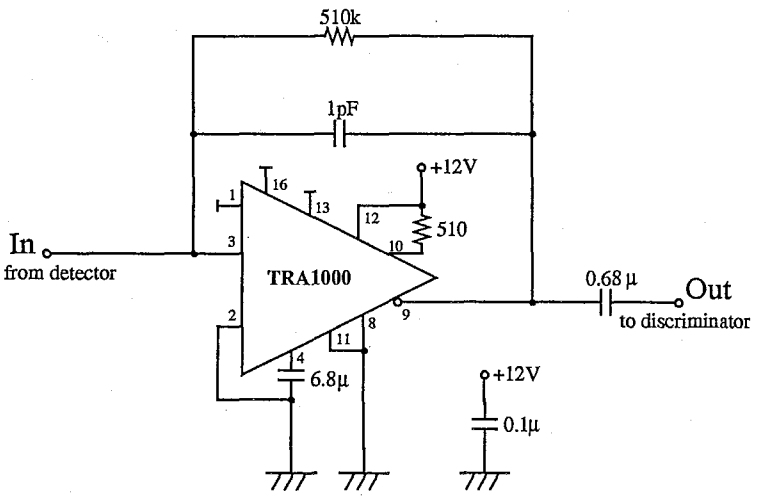

Figure 5.2: Circuit diagram of the preamplifier with TRA1000.

(a) CAMAC readout system in our early development

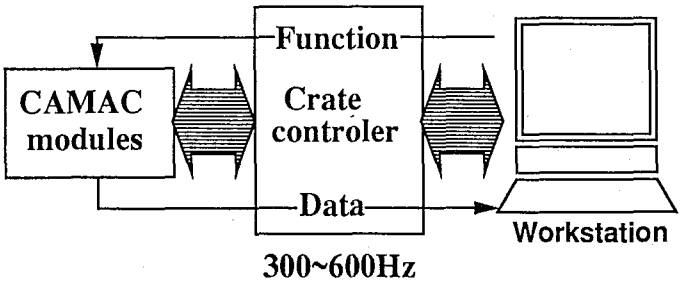

(b) CAMAC readout system with ACC

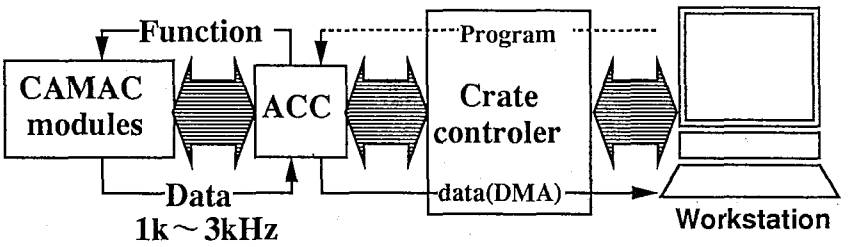

Figure 5.3: Block diagrams of the readout from CAMAC. (a) shows the direct readout, and (b) shows the readout using the ACC module.

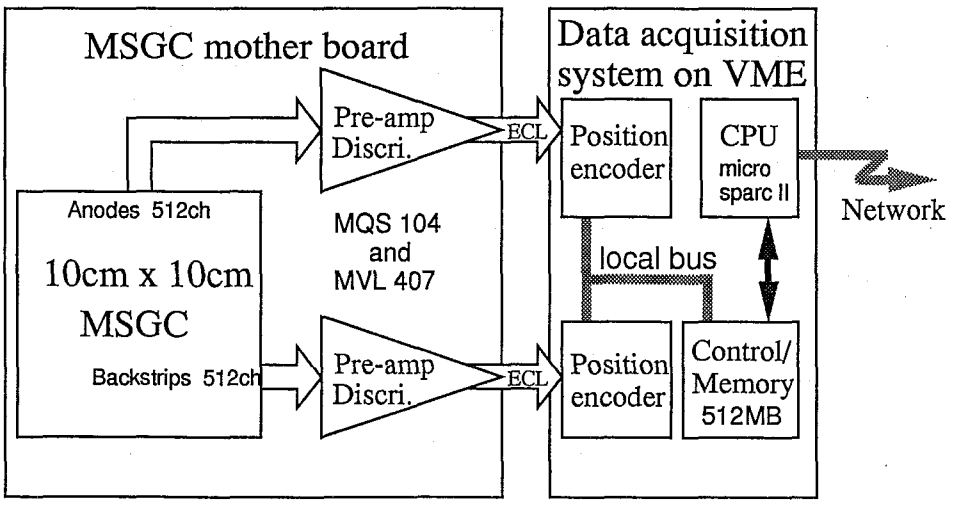

Figure 5.4: Block diagram of the MSGC fast data acquisition system

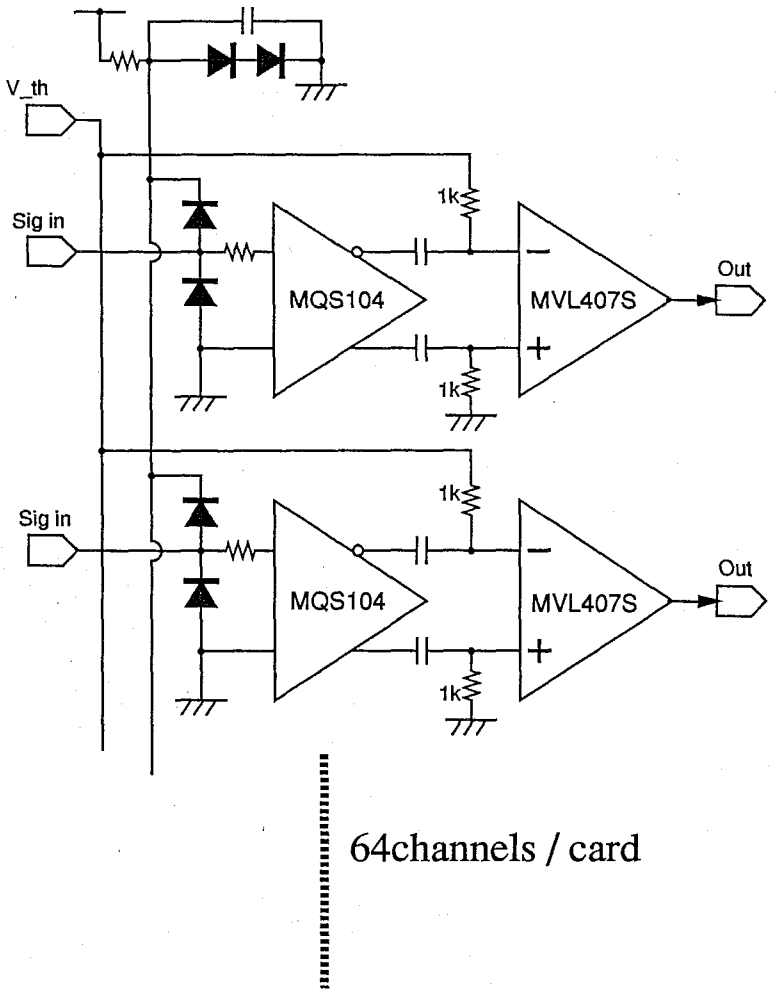

Figure 5.5: Circuit diagram for the new MSGC preamplifier and discriminator card.

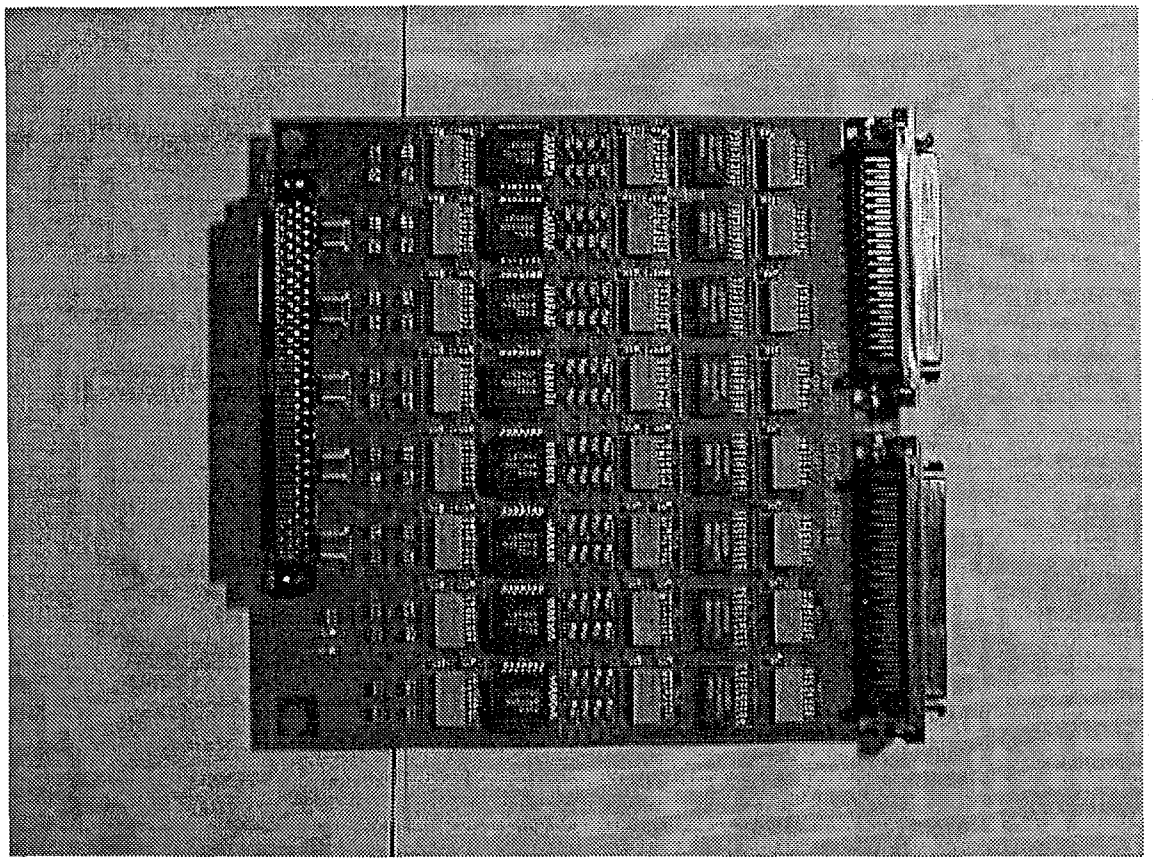

Figure 5.6: Photograph of a 64 channel pre-amplifier board.

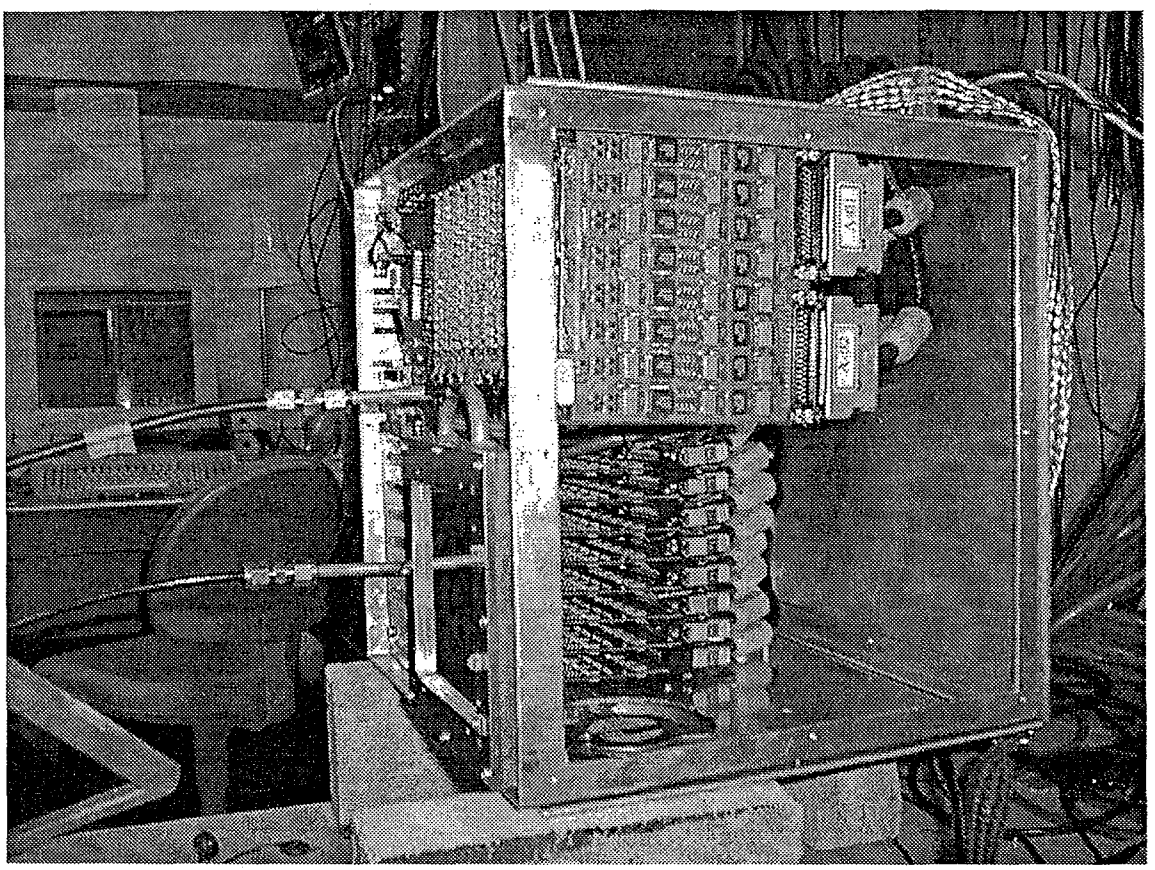

Figure 5.7: Photograph of the type II (10cm square) MSGC with preamplifier cards.

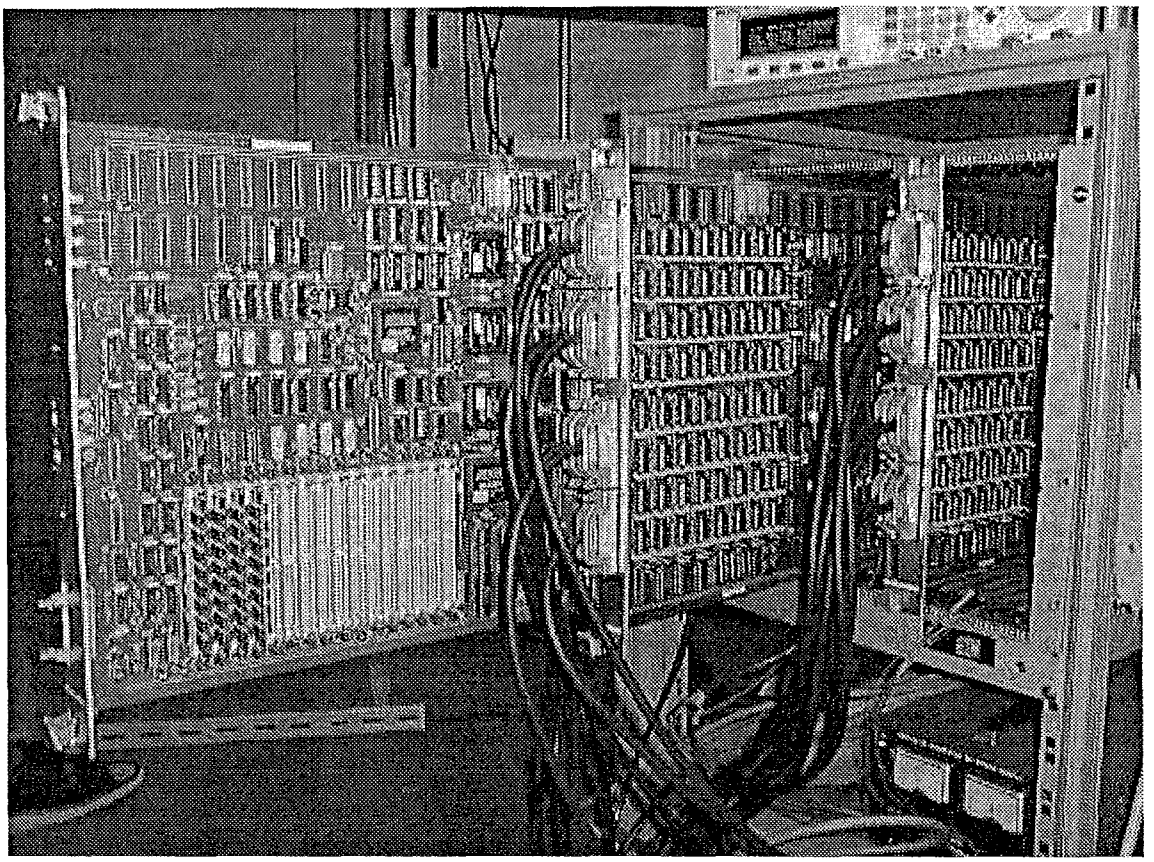

Figure 5.8: Photograph of the ultra fast data acquisition system.

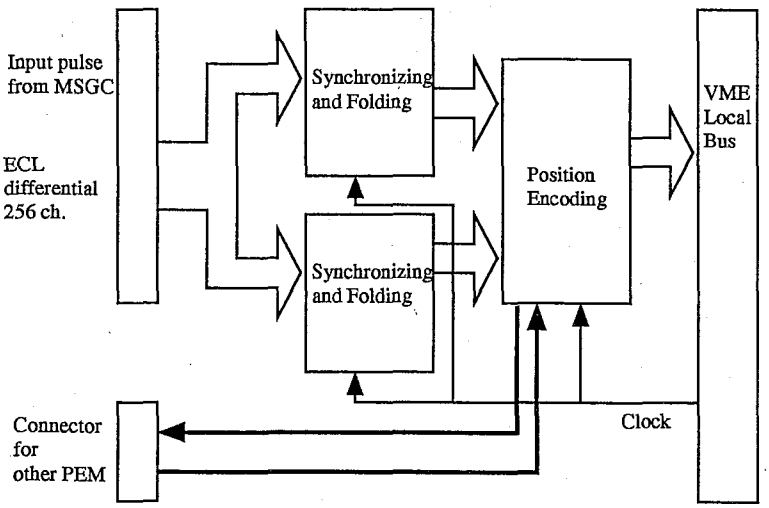

Figure 5.9: Block diagram of the position encoder

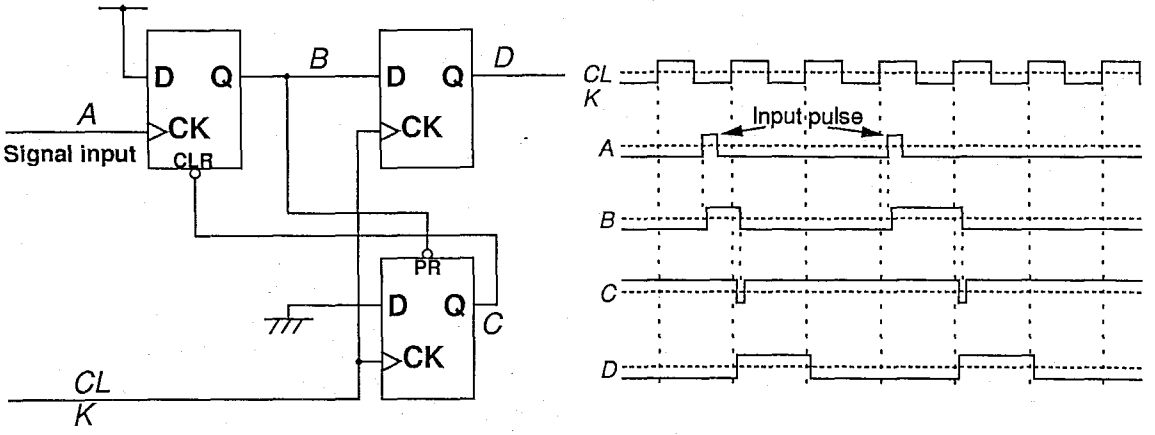

Figure 5.10: Circuit diagram of synchronizing circuit and a timing chart. The input A is processed as a clock input of D-type flip-flop, and the edge of the pulse is recognized. To synchronize with the system clock, the output of the first flip-flop B is latched in the next flip-flop D, and then the first one is cleared by the signal C.

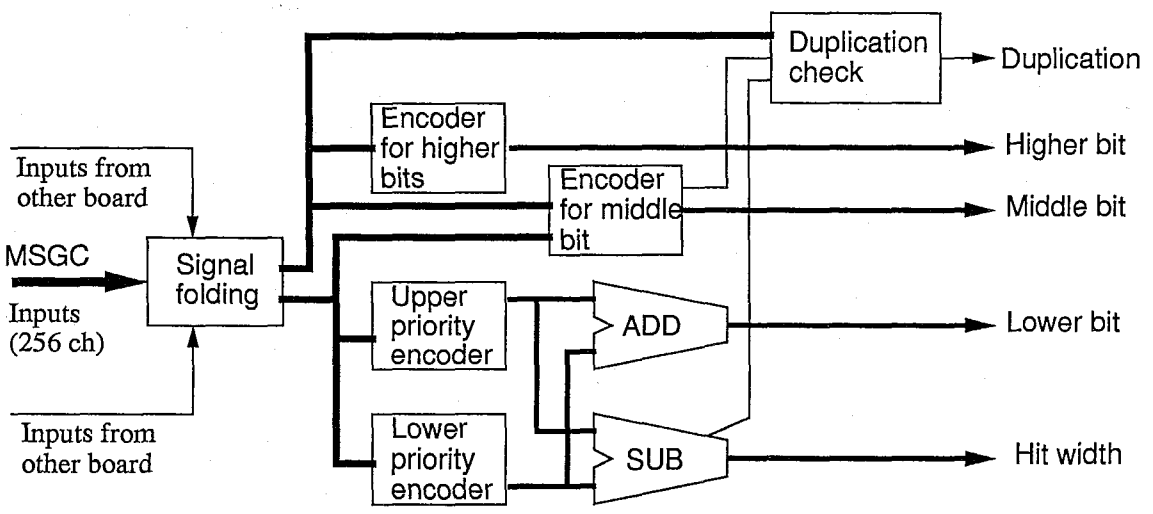

Figure 5.11: Main circuit diagram for PEM.

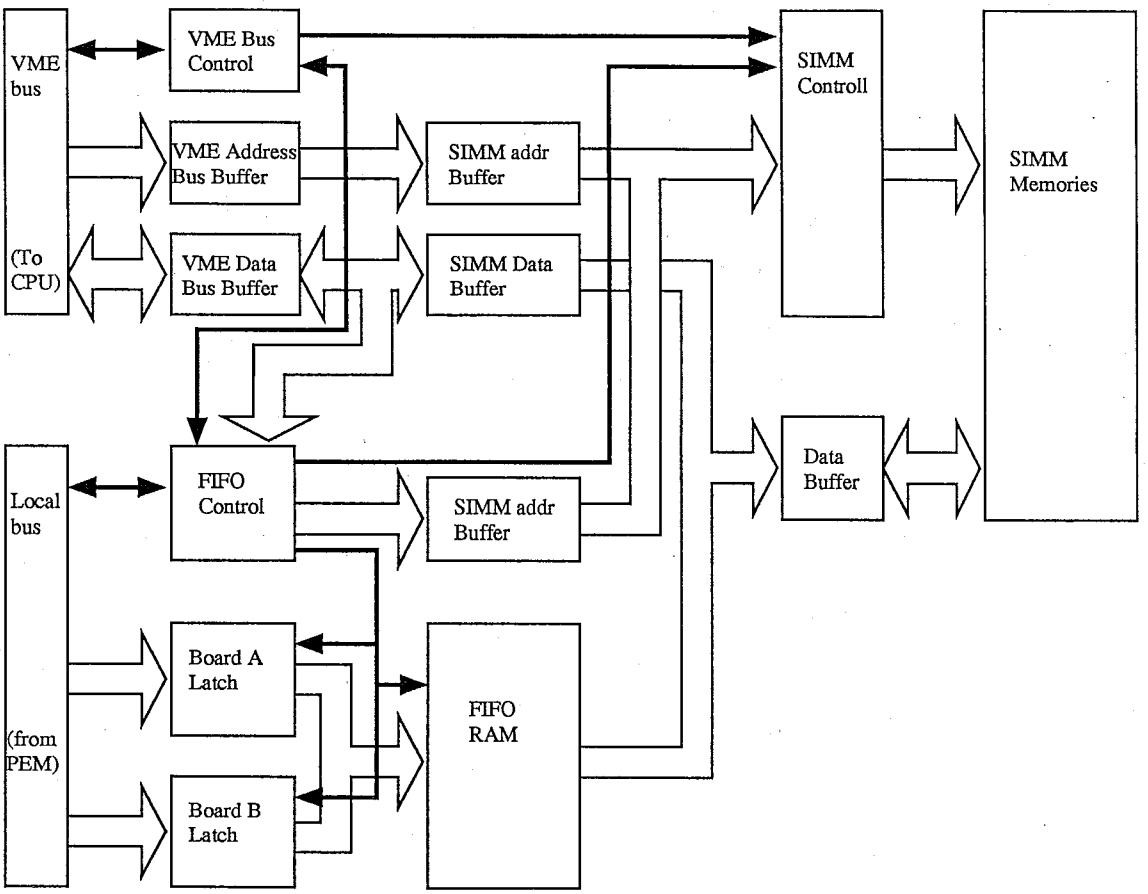

Figure 5.12: Block diagram of CMM.

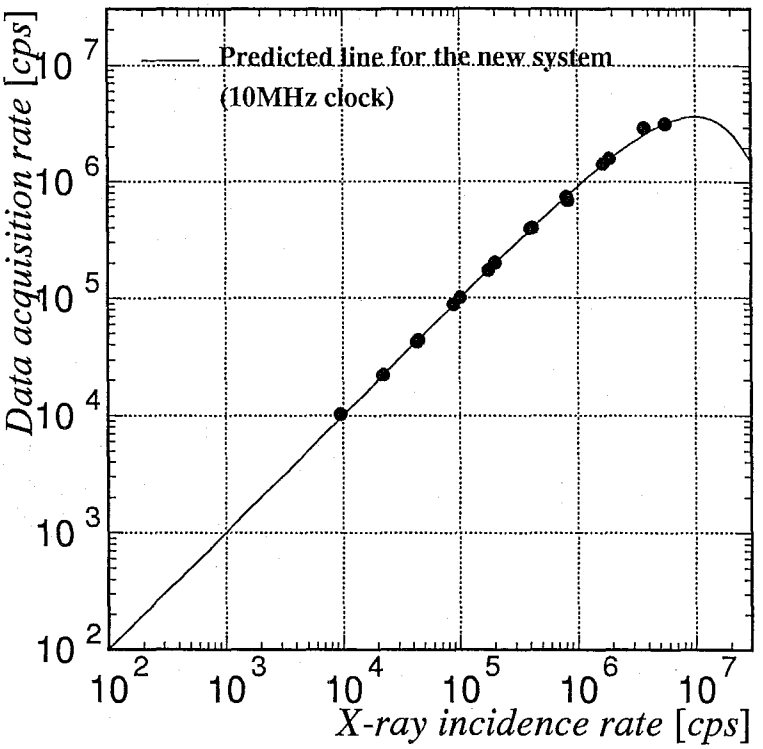

Figure 5.13: Result of performance test for DAQ rate

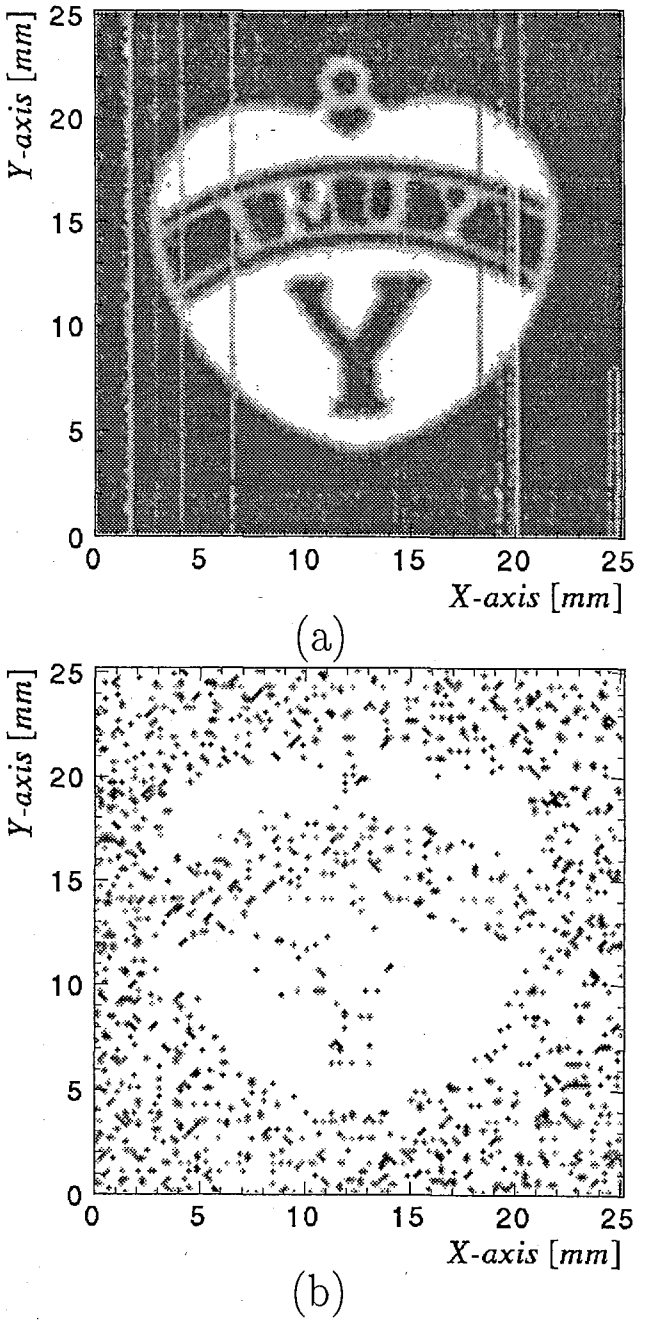

Figure 5.14: Imaging capability for 8 seconds exposure time with (a): the newly developed data acquisition system, (b): the old data acquisition system

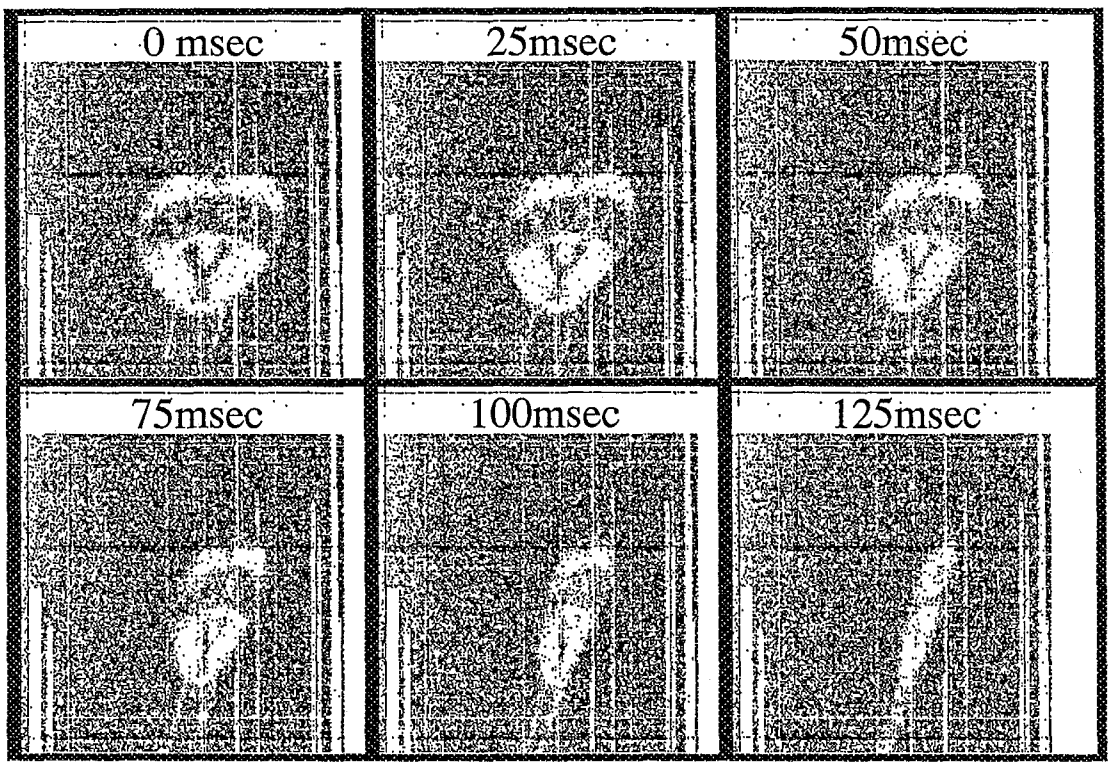

Figure 5.15: Snap shots of X-ray transmission images of a moving object

Chapter 6

Time resolved experiments using the MSGC in X-ray crystallography

The type II (10cm square) MSGC with the fast data acquisition system has sufficient potential as a real time X-ray area detector. X-ray crystallography is one of the most expected fields for the MSGC to be useful. Since the MSGC has both good imaging capability and very fine timing resolution, it is possible to measure the transition process of crystals by milli-second timing resolution. It has been impossible by existing detectors to acquire sequential images with the fast timing resolution. The comparison of the MSGC with other recent X-ray area detectors is listed in table 1.2. With this timing resolved property, MSGC also makes possible the new analyzing method for crystallography as mentioned hereafter "rotation continuous photograph (RCP)" method. In this chapter, the first experiment for time resolved crystallography with photo excitation, and RCP method with single crystal are described.

6.1 Time resolved measurements of the photo excitation process of solid crystal

6.1.1 Motivation

A molecule is excited in the process of reactions. For investigating the dynamical process of the reaction directly, observation of the excited structure using an X-ray diffraction (XRD) has been made. However, the lifetime of the excited state is very short (less than order of a second), and only a few molecules in the sample are excited in the reaction. Then,

the observation of excited state with XRD has not been possible up to now. The excited state is usually observed only through a spectroscopic method or through some peculiar physical properties. The development of the real-time X-ray area detector would allow us to observe the process of reactions directly.

Almost none of the existing X-ray detectors have ability for observing both time variation and images in an X-ray diffraction method. X-ray films or imaging plates (IP) have been used commonly for static XRD. Although an IP has good imaging capability and dynamic range as described in table 1.2, the time resolved measurements are very difficult. The pulse counting detectors are usable for time resolved measurements. Proportional counters (PC), scintillation counters (SC) and solid semiconductor detectors (SSD) have been used commonly. However, these pulse counting detectors do not have enough imaging capability for real-time measurements, and it is necessary to scan on the plane or spherical surface for obtaining the two-dimensional diffraction pattern. Recently, an imaging detectors using large area CCD (charge coupled device) has been available, and expected to improve the X-ray imaging analysis. Typical X-ray imaging detectors using CCD are X-ray imaging intensifier (X-II) and Fiber-CCD as described in chapter 1. The CCD has a fine property of imaging and time resolved measurement that reaches up to ~1sec/frame. This timing is still limited by the speed of sequential readout from CCDs that used in X-II and Fiber-CCD.

MSGC has both a fine imaging capability and an excellent timing resolution of $\sim$ 20ns, which allow us a very fast timing analysis for the direct observation for some of reaction processes. As the first observation of excited states, the light excitation of metal complexes were measured. Recently, the distortion of the diffraction pattern under light irradiation was observed for $[Bu_4N]_4[Pt_2(pop)_4]$ (pop means $P_2O_5H_2^-$) using an X-ray powder diffractometer [40]. One peak appeared in the X-ray powder pattern of $[Bu_4N]_4[Pt_2(pop)_4]$ was observed to move toward the higher diffraction angle when light was irradiated, and it returns when light was off. In the measurement done by Ikagawa *et al.*[40], they used only the visible light with filters to reduce the thermal effect, and the sample was cooled by water to keep it at constant temperature. The result of their measurements is shown in Fig 6.1. Diffraction patterns were shifted to the higher diffraction angle in light-on. This means that the structure of the unit cell in solid crystal was changed by light irradia-

tion. The similar phenomenon was observed for $VO(acac)_2$ (acac means acetylacetonate: $CH_3C = OCHC = OCH_3$). The diffraction pattern of $VO(acac)_2$ in light-on was shifted to the small angle. These were rare phenomena for solid crystals, and it is considered that these phenomena would be good prove for studying the direct observation of the excitation state. The structures of $VO(acac)_2$ and $[Pt_2(pop)_4]$ are shown in Fig. 6.2 and Fig. 6.3, respectively.

Although the time constant of this change is thought to be important parameters, it has not been known yet. In this experiment, the time constant of this diffraction peak movement has been measured using the MSGC. This is the first measurement made possible by the MSGC.

6.1.2 Experimental setup

Our goal is the measurement of the time constant for the variation of the structure caused through photon excitation. Structural analysis of crystal was not carried out in this measurement. The schematic setup for the experiments is shown in Fig. 6.4.

For the measurement, the powder of the crystal of $VO(acac)_2$ and the single crystal of $[Bu_4N]_4[Pt_2(pop)_4]$ were used. Although the change of the structure was observed for the diffraction pattern of powder $[Bu_4N]_4[Pt_2(pop)_4]$ in reference [40], the powder X-ray diffraction pattern was hard to be observed by our MSGC. One diffraction peak for $VO(acac)_2$, of which diffraction angle 2θ is 43^o for CrK_α (5.4keV) X-rays, was expected to have a large shift from another experimental data, which was measured using the powder diffractometer. From these data, the peak shift is expected to be about 0.1 degree for $CuK\alpha$ (8.0keV) X-rays. The peak shift for $[Bu_4N]_4[Pt_2(pop)_4]$ is also expected to be very small (0.03 degree), however, it was reported that the direction of peak shift is opposite side against that due to thermal influence, therefore it is reliable to distinguish the photon absorption effect from the thermal effect.

The sample was placed in front of the MSGC, and the distance between the sample and the MSGC is 8 $\sim$ 9cm. The xenon light was used as the light source for photo irradiation to the sample. The spectrum of the xenon light and the absorption spectrum of $[Bu_4N]_4[Pt_2(pop)_4]$ are shown in Fig 6.5 and Fig 6.6 respectively. The xenon light source of 150W was placed at the angle of 45° from the X-ray beam axis, and between the xenon light

source and the sample, an optical shutter and a convex lens were placed. In order to cut the infrared part of xenon light, a filter was attached to the xenon light. The transmittance spectrum with this filter is also shown in Fig 6.5. An X-ray tube of a chromium target and a vanadium filter (K_α = 5.4keV) was used as the X-ray source. In this energy, the large distortion of diffraction pattern is expected to be 1.5 times greater than that with CuK_α (8.0keV) X-rays. Also the fluorescent X-rays from vanadium atoms in $VO(acac)_2$ is expected to be minimized using CrK_α X-rays. The X-ray source was collimated to 1mmϕ, and the tube voltage and current were set to 40kV and 40mA respectively. The detector was slanted in the direction of the expected diffraction pattern (or point) to avoid the slant incident effect of MSGC (see section 3.2). In this experiment, this angle was 35° $\sim$ 40°.

6.1.3 Measurements and analysis

The powder X-ray diffraction pattern of $VO(acac)_2$ was measured. The image of Debye-Scherrer rings obtained by MSGC is shown in Fig. 6.7. Since the detection plane of the MSGC is leaned from the right angle of the incident X-ray beam, the shape of a Debye-Scherrer ring becomes an ellipse or a hyperbola.

In the analysis, the projections of the rings for the 2θ directions are necessary, and it is calculated as follows. The X-rays scattered by the powder with $\Theta(\equiv 2\theta)$ diffraction angle is on the cone as shown in Fig. 6.8. In this geometry, Z axis is defined as the source beam line, and the sample is set on the origin. X and Y axes are defined as the other two axes of the rectangular coordinates, and those directions are arbitrary. A diffraction cone that has diffraction angle of Θ is expressed by the following formula,

$$X^2 + Y^2 - Z^2 \tan^2 \Theta = 0. \tag{6.1}$$

In order to obtain the projection of equation (6.1) on the slant detector plane, it is assumed that the plane is fixed at the straight position from the Z axis, and the beam axis is rotated in the XZ plane. In this geometrical transformation, new xyz coordinates are defined as shown in Fig. 6.9. The X-ray beam is on the z axis, and ψ is defined as the angle between Z and z. This transformation is expressed as follows;

$$\begin{pmatrix} x \\ y \\ z \end{pmatrix} = \begin{pmatrix} \cos\psi & 0 & \sin\psi \\ 0 & 1 & 0 \\ -\sin\psi & 0 & \cos\psi \end{pmatrix} \begin{pmatrix} X \\ Y \\ Z \end{pmatrix} \quad , \tag{6.2}$$

substituting (6.2) into (6.1), the following equation is obtained;

$$\begin{aligned} & x^2(\cos^2\psi - \sin^2\psi\tan^2\Theta) + y^2 \\ & +z^2(\sin^2\psi - \cos^2\psi\tan^2\Theta) \\ & +2xz\cos\psi\sin\psi(1+\tan^2\Theta) \quad = 0 \quad . \end{aligned} \tag{6.3}$$

The plane of the detector is expressed as

$$z = d \quad , \tag{6.4}$$

where, d is the distance between the sample and the detector plane. The observed curve on the plane is the intersection of the equation (6.3) and (6.4). Substituting (6.4) into (6.3), and arranging about $\tan\Theta$, the following equation is obtained;

$$(x\cos\psi + d\sin\psi)^2 + y^2 - (x\sin\psi - d\cos\psi)^2\tan^2\Theta = 0. \tag{6.5}$$

Θ should not be negative value, and the resultant solution of Θ is

$$\Theta = \begin{cases} \tan^{-1}\left(\frac{\sqrt{(x\cos\psi+d\sin\psi)^2+y^2}}{d\cos\psi-x\sin\psi}\right) & (x\tan\psi < d) \\ \tan^{-1}\left(\frac{\sqrt{(x\cos\psi+d\sin\psi)^2+y^2}}{d\cos\psi-x\sin\psi}\right) + \pi & (x\tan\psi > d) \end{cases} . \tag{6.6}$$

The imaging data on the MSGC is expressed as the two-dimensional histogram. A pixel in the (x, y) plane corresponds to the scattering angle Θ by the equation (6.6), and a histogram for Θ is filled from that transformation.

In this measurement (d = 82mm and $\psi = 35°$), the bin width of Θ histogram is 0.1°. The length on the MSGC corresponding to the minimum division of the angle ($\sim 150\mu$m) is narrower than the pitch of the MSGC electrodes (200μm). The approximate diffraction flux is obtained by adding the counts of pixels included in one bin. For more optimizations, the azimuthal region for the above adding is also restricted. Near the $\frac{n\pi}{2}$ of azimuthal angle (see Fig. 6.10), contour lines for Θ are parallel to anodes or backstrips, and then some of Θ bins contain a few or no pixels (see Fig. 6.11). Therefore, azimuthal angle should not be near the $\frac{n\pi}{2}$. The effect of slant incidence also restricts the optimized azimuthal angle. Figure 6.12 shows the optimized angle on the detector plane. At the base point on the plane of normal from the sample (denoted by **H** in Fig. 6.9 and Fig. 6.12), there is no effect of the slant incidence. At the other points, the images are stretched to the radial direction

from **H**. Then, for arbitrary diffraction angle of $\Theta\,(<\phi)$, the best point to minimize the slant incident effect is the tangential point on contour curve of Θ from **H**. In this analysis, the proper region of the azimuth was chosen for $10^o < \psi < 40^o$, in which 0^o is defined as the direction of **H** by hand, by considering above conditions and by minimizing dead strips.

Figure 6.13 shows the powder diffraction pattern corresponding to the diffraction angle 2θ for the same data of Fig. 6.7. The movement of the peak at the $2\theta = 43°$ with light irradiation was measured by the MSGC. The measured peak width was about 1 degree as shown in Fig. 6.14, which is due to the position resolution of the MSGC (200μm bin width) and the size of the sample (0.5mm$\phi\times$ 1mm). For obtaining a precise diffraction angle, the large amount of events and statistical analysis are necessary. The intensity of X-rays was 1.6kW (40kV, 40mA), and the counting rate of the diffracted X-rays was about 10^4 cps. The counting rate in the peak of Fig. 6.14 was $\sim$ 140cps. For obtaining the sufficient statistics, the light irradiation was chopped periodically every ten or two seconds by the optical shutter having 6ms opening/closing time. The status of the light was monitored by a photodiode behind the sample. The timing of the light chopping was tagged by the signal of the photodiode, and the timing for each X-ray event was also recorded with the position data.

Secondly, the time variation of the diffraction spot was measured by single crystal of $[Bu_4N]_4[Pt_2(pop)_4]$. The measurement and analysis were basically similar to those in the powder diffraction case. The rotation photograph of $[Bu_4N]_4[Pt_2(pop)_4]$ is shown in Fig. 6.15. In order to obtain particular diffraction spot, all of diffraction spots were taken by RCP method (see section 6.2) at first, and then the angle of the crystal was fixed at which the proper diffraction spot appears. The two diffraction spots were selected in this measurement. The azimuthal angle for the analysis was restricted within the 3° width around the angle of the proper spot.

6.1.4 Results and discussion

For the powder of $VO(acac)_2$, the ring on $2\theta = 42.7^o$ (CrKα) was selected for the measurement of the peak shift. Fig. 6.14 is the diffraction pattern near the proper peak. By fitting the peak using Gaussian function, the mean value and its error were calculated, and held

in one periodic cycle as a function of the elapsed time after light-on as shown in Fig. 6.16 and in Fig. 6.17. In the condition of Fig. 6.16, the light on/off cycle was repeated every 10 seconds, and in the condition of Fig. 6.17, that was repeated every 2 seconds. From these figures, the peak shifts were estimated. The statistical errors for each plotted point are less than 0.01° thanks to the folding method. In Fig. 6.16, the position shift of the proper peak was found to be 0.2° in the 5 second transition time. The faster component of the peak movement was also searched for as shown in Fig. 6.17, where the diffraction peak angle was analyzed in 100ms time interval. However no significant fast component was observed. The direction of the peak movement by photo excitation and that by thermal expansion effect is the same in this sample, and these two effects cannot be distinguished in this plot. Nevertheless, we could successfully display that the time-resolved measurement with MSGC makes possible to observe the dynamical process of the crystal structure directly.

On the other hand, the light excitation measurement of $[Bu_4N]_4[Pt_2(pop)_4]$ sample is expected to distinguish the light effect from the thermal effect. The results of measurements for the diffraction angle of 35.7° and 34.7° are shown in Fig. 6.18(a),(b) respectively. In these figures, the duration of light on/off cycle was both 200 seconds, and the statistical error of each plotting point was achieved to be $\sim$ 0.001° thanks to the folding method. Obviously these movements have two timing components. One has the slow component with 50 seconds transition time, where the peak moved toward the large diffraction angle with light-on, and the other has the fast component with less than 10 seconds transition time of which peak moves the opposite side of the slow one. The observed peak movements in these transitions were both $\sim$ 0.2°. The timing variation of 1 second bin around the just light-on timing is also shown in Fig. 6.19 using the same data as Fig. 6.18(b). Although the statistical errors become $\sim$ 0.003° due to low statistics, the fast movement of the diffraction peak was observed clearly just after the light irradiation. The time constant of the fast component was obtained to be 1.9 seconds. To estimate the movement of the peak due to the thermal effect, the air varying the temperature was blown against on the sample, and the peak shift was also measured similarly. The temperature was controlled by a thermocouple near the sample. The movement of 2θ in varying the temperature is shown in Fig. 6.20. From Fig. 6.20, the crystal of $[Bu_4N]_4[Pt_2(pop)_4]$ has the tendency of thermal constriction. Therefore it is concluded that the peak movement of the fast component is

due to the light illumination, and the slow component is due to the thermal effect.

The direction of the peak movement by the light illumination was not consistent with the results of measurements with powder diffraction elsewhere [40]. The reference [40] reported that almost all the diffraction peaks shifted to the large diffraction angles under light irradiation. The inconsistency between those results and our results are explained as follows: (1) the diffraction peaks obtained in our measurement have the opposite preference for light irradiation accidentally. (2) The control of temperature seems not to be not perfect in the experiment in [40]. Perfect rejection of the thermal expansion due to the light irradiation is difficult. Both in the light illumination and thermal effect, the diffraction peaks shift to the large angle in [40]. (3) A behavior of $[Bu_4N]_4[Pt_2(pop)_4]$ is different in single crystal and in powder crystal. To investigate it more precisely, another measurement should be necessary. However, since the two timing components of peak movement were observed in our measurement, in which the slow component can be assigned due to the thermal effect, We can conclude that the fast component is due to the light excitation. The measured timing constant of this excitation is 1.9 ± 0.3 seconds.

6.2 The basic experiments for fast structure analysis with Rotation Continuous Photograph (RCP) method using MSGC

6.2.1 Earlier methods for crystal XRD analysis

A two-dimensional image of a diffraction pattern is not sufficient to obtain the three-dimensional information of an objective crystal. When using a monochromatic X-ray beam, several diffraction patterns are taken varying the angle between one axis of the crystal and the X-ray beam over an acceptable angle range. The MSGC can record both the position and the arrival time of each X-ray photon with a few ten ns resolution. The timing just gives us the information on the angle of rotation of the crystal with a fine angular resolution. This allows us to get all the information needed for three-dimensional crystal analysis from the only one measurement.

For analyzing the crystal structure, two steps are necessary as follows: (1) the size, form of unit cell, and space group of the sample are estimated, (2) getting all positions and

strengths of diffraction points. For any wave length λ of X-rays, the reflection points from the sample crystal appear on Ewald's sphere in the reciprocal lattice as shown Fig. 6.21. The origin of this reciprocal lattice space O must be located on this sphere, and the diametrical line including the origin corresponds to the path of the incident X-rays. Although the lattice is three dimensional, the XRD method can provide only two or one dimensional information. Then, another piece of information is needed for obtaining the projection of the reciprocal lattice.

The Laue photograph is one of the popular technique to obtain the projection of the reciprocal lattice. By using a white X-ray beam, the lattice point with polar angle 2θ and azimuth ϕ is projected on a X-ray film. This method needs some known parameters such as the crystal system to reconstruct the tree dimensional point on lattice of each spot. Therefore, for crystals of which axes are unknown, we have to try to take several pictures for getting accurate axis.

The oscillation photograph is one of the other popular methods, which uses a monochromatic X-ray beam. When the crystal is oscillated between θ_1 and θ_2 angle as shown in Fig. 6.22, the appeared image on film corresponds to the lattice point in the gray region of Fig. 6.22. In this method, the diffraction angles of the points in the image are accumulated over the oscillated angles, and the exact structure of lattice has to be estimated using known parameters as well as the Laue photograph. In order to transform the diffraction spots into the reciprocal lattice, many trials by varying the oscillation angle are required.

The Weissenberg camera provides the other projection of the reciprocal lattice. The schematic structure of this camera is shown in Fig. 6.23. The crystal rotates around the one of the crystal axes, and a cylindrical X-ray film is moved simultaneously along the same axis of the rotation of crystal. There is a cylindrical slit between the sample crystal and the X-ray film in the direction of the axis of the rotation, and any one layer (e.g. $(hk0)$, $(hk1)$...) of the diffraction pattern is measured as a two-dimensional pattern along the rotation angle of the crystal. In this measurement, the accurate coincidence of the rotation axis with one of the crystal axes is necessary. Mainly this method is used for obtaining the size and the crystal system of the unit cell.

To estimate the exact intensity of all X-ray diffraction spots, four-axes X-ray diffractometer is used generally. The sample crystal can be rotated around 3-axes: ϕ, κ, ω,

and the pulse counting detector (such as SC or PC) is rotated around 2θ axis. With this diffractometer, all the lattice points in reciprocal space within the sphere of $2/\lambda$ radius, and the intensities of all spots are measured exactly. Since this detector is a 0-dimensional (point like) type, it takes much time to scan all the reciprocal space. $10 \sim 20$ hours will be necessary in the measurement of a typical unorganized crystal.

6.2.2 Three dimensional XRD method with MSGC

The MSGC can obtain both the positions and timings of incident X-rays. It enables us to measure both the position of the diffraction spot and its appearance timing which corresponds to the rotation angle of the sample crystal. Therefore, wide region of the reciprocal space of the sample crystal is at once calculated using only the data obtained by the MSGC. This method is called here Rotation Continuous Photograph (RCP) method. In this method, not only the three-dimensional lattice points are observed quickly (less than a few minutes depending on the source intensity and the rotation speed), but also no exact matching of the axis of crystal to the rotational axis is required. Both the size of the unit cell and the lattice constant are simultaneously obtained from observed three-dimensional points. The repetition trials of measurements of X-ray images for axis fixing are no longer necessary. In addition, the intensity of each diffraction spot is measured exactly due to the pulse counting capability of the MSGC.

The intensity of the diffraction spot I_{hkl} is proportional to the square of the structure amplitude $|F_{hkl}|^2$, where the structure factor F_{hkl} is expressed using electron density $\rho(xyz)$ and infinitesimal volume $V dxdydz$ as follows,

$$F_{hkl} = V \int_0^1 \int_0^1 \int_0^1 \rho(xyz) e^{2\pi i(hx+ky+lz)} dxdydz. \tag{6.7}$$

This is a three-dimensional periodic function, and can be expanded in Fourier series,

$$\rho(xyz) = \frac{1}{V} \sum_{-\infty}^{\infty} \sum_{-\infty}^{\infty} \sum_{-\infty}^{\infty} F_{hkl} e^{-2\pi i(hx+ky+lz)}. \tag{6.8}$$

If F_{hkl} is obtained, the electron density structure function $\rho(xyz)$ is calculated, and the structure of the crystal is determined. Unfortunately, the F_{hkl} contains the imaginary part, then F_{hkl} cannot be obtained from I_{hkl} directly. However, the precise measurements of the $|F_{hkl}|$ enable us to calculate the phase term from the dependence on the relationships of

each structure factor [41]. With the new RCP method, the reciprocal space is observed immediately with precise values of $|F_{hkl}|$, and the structure of the crystal is determined in a short time.

6.2.3 The measurement of RCP method and results

The RCP measurement using the MSGC was carried out. The X-ray tube with the copper target and the nickel filter (K_α: 8.0keV) was used as the X-ray source. As a sample, a single crystal of Phenothiazine-Benzilic acid complex was used. The sample was placed on the rotatable goniometer. The rotation speed of crystal was 216 seconds/cycle, which corresponded to 5/3 degree/second. The MSGC was placed normal to the X-ray beam, and the center of the beam was pointed on one edge of the detection area. Figure 6.24 shows the schematic view for this experiment. The positions of diffracted X-rays and their timings were measured using the MSGC and the fast data acquisition system mentioned in chapter 5. The operating voltage and current of the X-ray tube were 40kV and 40mA, respectively, and the 1mmϕ collimated X-ray beam was irradiated to the sample. The size of sample was about $(0.5\text{mm})^3$. In this measurement, the counting rate was 2000 $\sim$ 10000 events/second. All of the time stamp of each X-ray events were recorded.

The two-dimensional image of diffraction pattern integrated during the several rotations of the crystal is presented in Fig. 6.25. This figure corresponds to the rotation photograph. A lot of diffraction spots and back ground X-ray noises can be seen, and note that the crystal axis is not parallel to the rotation axis exactly. Figure 6.26 shows the time resolved sequential images observed every 0.3 second exposure time. Each picture corresponds to 0.5 degree width of an oscillation X-ray picture. Diffraction points are found to be very clear as compared with integrated one shown in Fig. 6.25. The S/N ratio of diffraction spots in time (angle) resolved picture can be improved by a factor of 100 $\sim$ 300 in this measurement (see also [42]). The three-dimensional image of this measurement in which each spot is plotted according to its two-dimensional position (x, y) and the rotation angle of crystal (ϕ) dimension is shown in Fig. 6.27, and the projection of this figure into (y, ϕ) plane was shown in Fig. 6.28. Clear peaks concentrated over 0.5 degrees can be found, which indicates that the noise away from the peak can be removed easily using the angle information. Fig. 6.29 shows the same figure of Fig. 6.27 after applying this noise-reduction

method. There remains very little noise below the clear peak.

6.2.4 Analysis and Discussion

As described in subsections 6.2.1 and 6.2.2, the three dimensional points as shown in Fig. 6.29 can be transformed to the points on the reciprocal lattice space. When the origin of image is defined as the center of beam, and x, y are defined as the coordinates on the detector plane, a sine and a cosine of the diffraction angle 2θ are expressed as follows;

$$\sin 2\theta = \frac{\sqrt{x^2+y^2}}{\sqrt{x^2+y^2+d^2}}, \cos 2\theta = \frac{d}{\sqrt{x^2+y^2+d^2}}, \tag{6.9}$$

where, d is the distance from the sample to the detector plane. When the azimuth of the diffraction angle is defined as ψ, a sine and a cosine of ψ become,

$$\sin\psi = \frac{y}{\sqrt{x^2+y^2}}, \cos\psi = \frac{x}{\sqrt{x^2+y^2}}. \tag{6.10}$$

Since the diffraction image obtained by the imaging detector is the projection of lattice points on Ewald's sphere, it can be mapped on the sphere in the reciprocal lattice space of which coordinates are defined as (s,t,u), where s axis is defined as the rotation axis of the crystal, and t,u are defined as another two axes of the rectangular coordinates. Here the rotation angle ϕ is defined as the angle between the incident X-ray beam and the u axis. The rotation of the crystal corresponds to the rotation of the incident X-ray beam on the tu-plane. In the case of $\phi = 0$, the coordinates in reciprocal space s and t correspond to the coordinates of the two-dimensional plane on the detector (x,y). The center of Ewald's sphere A is $(0,0,\frac{1}{\lambda})$, and radius of the sphere is $\frac{1}{\lambda}$. The point $P(x,y)$ on the x,y coordinate corresponds to the point $Q_0 = (s_0,t_0,u_0)$ on the Ewald's sphere and both of these two expressions have the same diffraction angles of 2θ and azimuths ψ. The coordinates of Q_0 become

$$\begin{aligned}\begin{pmatrix} s_0 \\ t_0 \\ u_0 \end{pmatrix} &= \frac{1}{\lambda}\begin{pmatrix} \sin 2\theta\cos\psi \\ \sin 2\theta\sin\psi \\ \cos 2\theta - 1 \end{pmatrix} \\ &= \frac{1}{\lambda\sqrt{x^2+y^2+d^2}}\begin{pmatrix} x \\ y \\ d-\sqrt{x^2+y^2+d^2} \end{pmatrix}. \end{aligned} \tag{6.11}$$

The general case for the arbitrary ϕ is expressed by the rotation of Q_0 around the s axis. Therefore, the reciprocal space coordinates $Q = (s,t,u)$ can be written using the

parameters (x, y, ϕ) which are obtained from the image of the MSGC as follows;

$$\begin{aligned}\begin{pmatrix} s \\ t \\ u \end{pmatrix} &= \begin{pmatrix} 1 & 0 & 0 \\ 0 & -\sin\phi & \cos\phi \\ 0 & \cos\phi & \sin\phi \end{pmatrix} \begin{pmatrix} s_0 \\ t_0 \\ u_0 \end{pmatrix} \\ &= \frac{1}{\lambda\sqrt{x^2+y^2+d^2}} \begin{pmatrix} x \\ -y\sin\phi + (d - \sqrt{x^2+y^2+d^2})\cos\phi \\ y\cos\phi + (d - \sqrt{x^2+y^2+d^2})\sin\phi \end{pmatrix} .\end{aligned} \tag{6.12}$$

Using this equation, the data from MSGC is eventually transformed to the reciprocal space. To obtain the intensity of each diffraction spot, the counts of each spot should be compensated by the Lorentz factor. As the sample crystal is rotated, the crossing speed of Ewald's sphere on each diffraction spot is different. The compensation coefficient L for a diffraction spot, which has (s, t, u) coordinates in the reciprocal lattice space and appear at the rotation angle ϕ, is calculated as the following equation,

$$L(s,t,u,\phi) = \frac{\lambda\sqrt{s^2 + (t - \frac{1}{\lambda}\sin\phi)^2 + (u - \frac{1}{\lambda}\cos\phi)^2}}{t\cos\phi - u\sin\phi} \quad . \tag{6.13}$$

In order to obtain precise I_{hkl}, L should be multiplied by observed intensity of the each diffraction spot. Figure 6.30 shows the diffraction spots in the reciprocal space, in which the observed image of Fig. 6.29 is transformed using the equation (6.13). In this measurement, the MSGC did not work with expected performance, because the MSGC used in this measurement was the first made prototype having a 10cm×10cm large detection area, which has still inefficient region and broken electrodes. Therefore it is not fair to argue the precise quantity of the data all over the detection area. Since the precise measurement for the intensity of each diffraction spot is necessary for obtaining the structure factor F_{hkl}, the crystal structure analysis has not been possible from this set of data yet. However, an improved 10cm square MSGC is being constructed, and the full structure analysis will be soon possible.

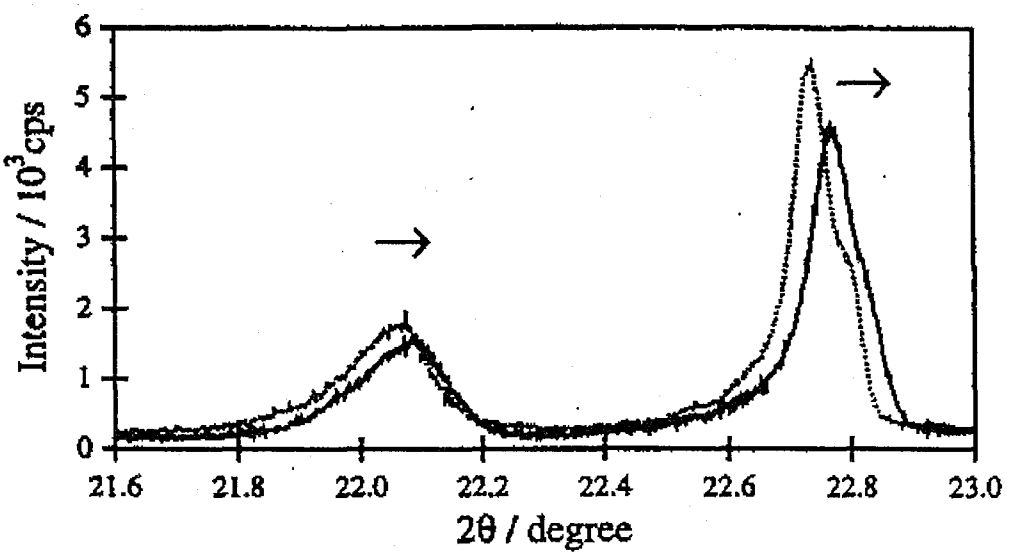

Figure 6.1: Powder X-ray diffraction of $[Bu_4N]_4[Pt_2(pop)_4]$ under light irradiation (solid line) and no light (dashed line). [40]

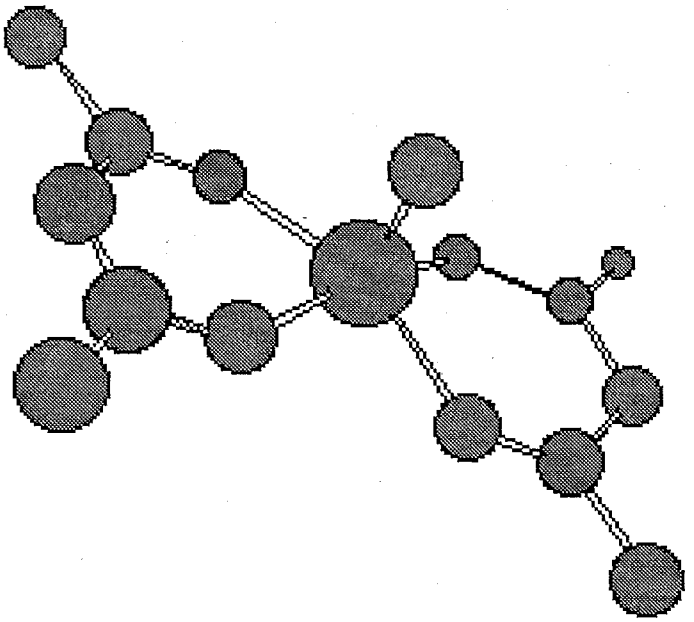

(a)

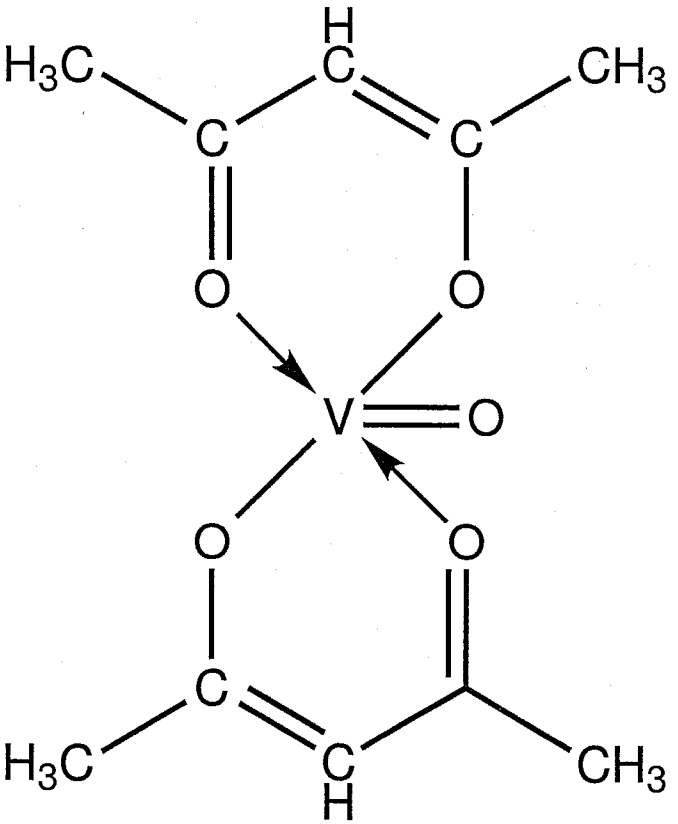

(b)

Figure 6.2: 3D-structure (a) and constitutional formula (b) of $VO(acac)_2$.

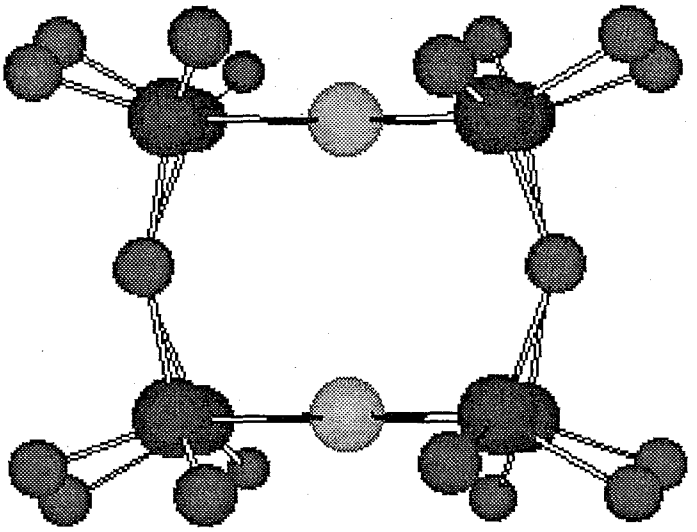

(a)

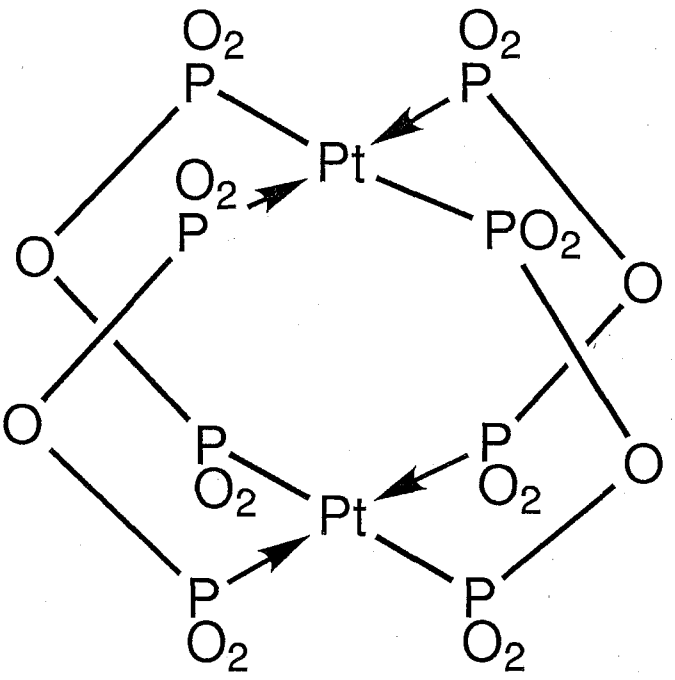

(b)

Figure 6.3: 3D-structure (a) and constitutional formula (b) of $[Bu_4N]_4[Pt_2(pop)_4]$

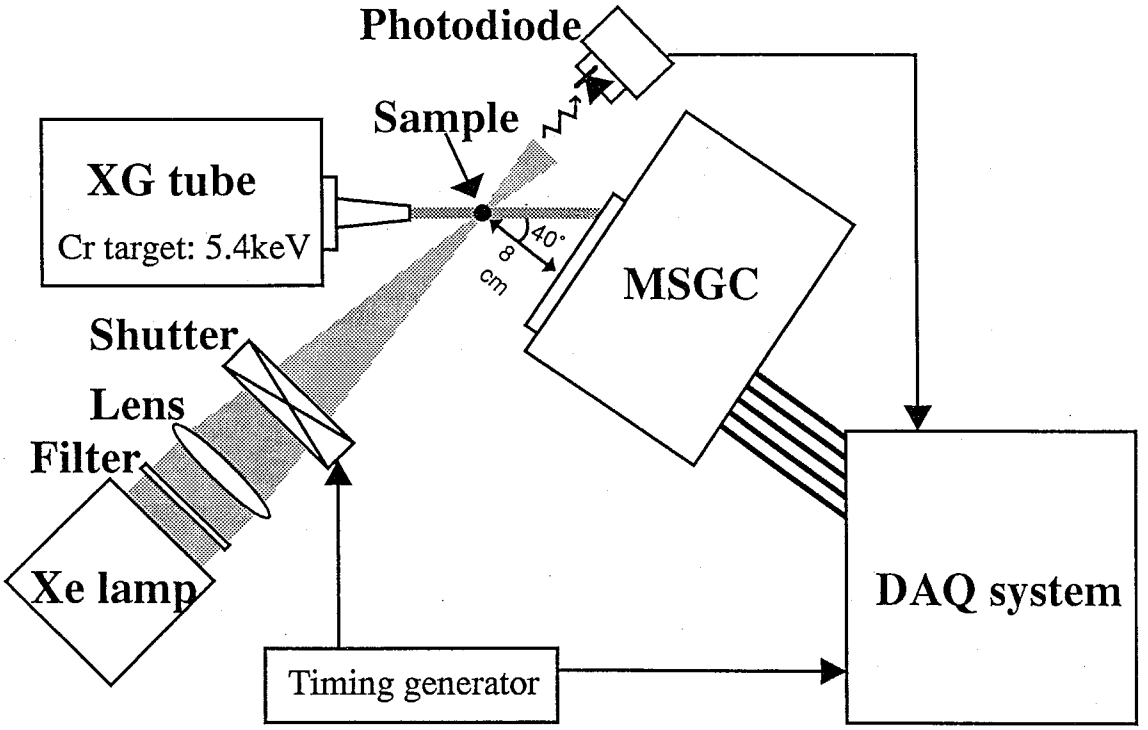

Figure 6.4: Experimental setup of the measurement for photo excitation.

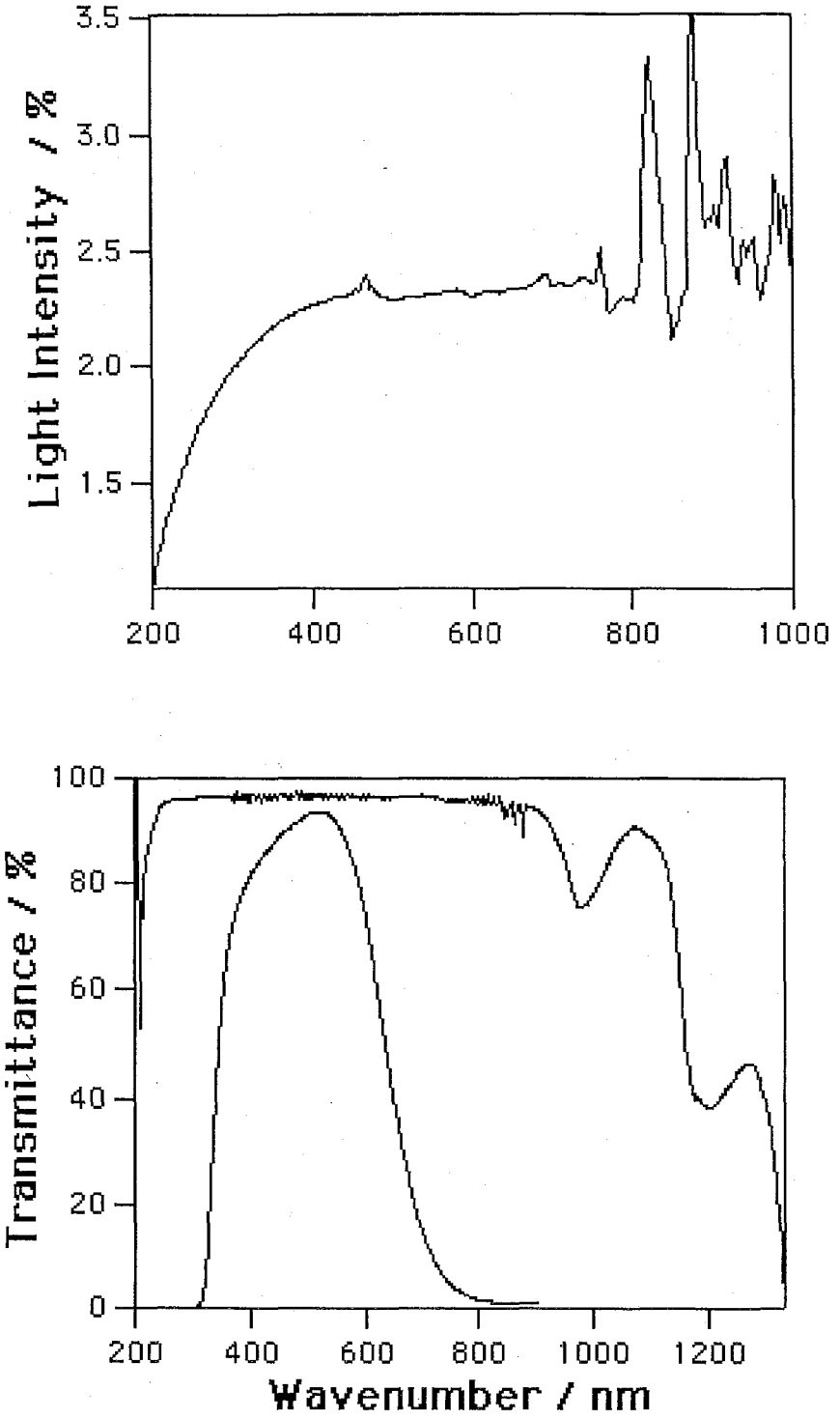

Figure 6.5: Spectra of xenon lamp and that with IR-cut filter.

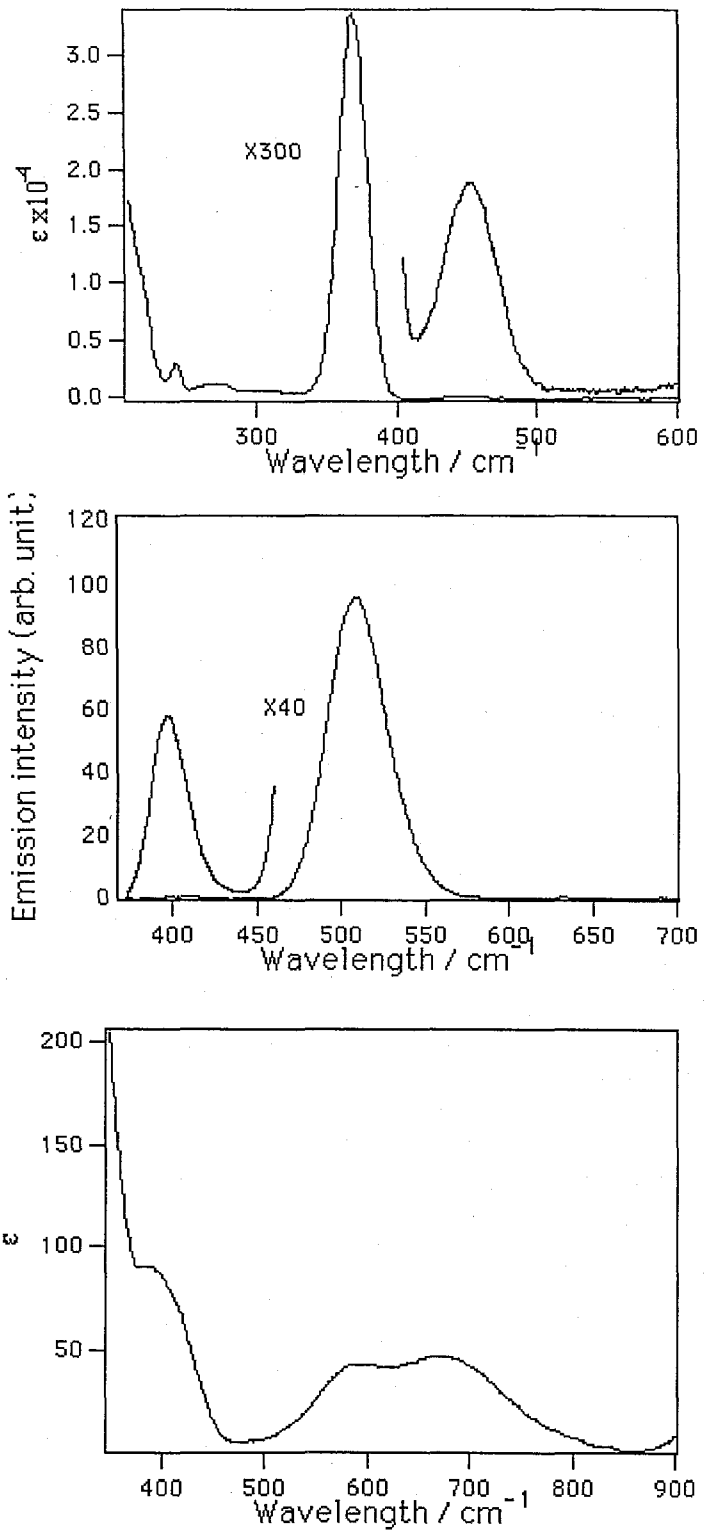

Figure 6.6: Absorption and emission spectra of $[Bu_4N]_4[Pt_2(pop)_4]$

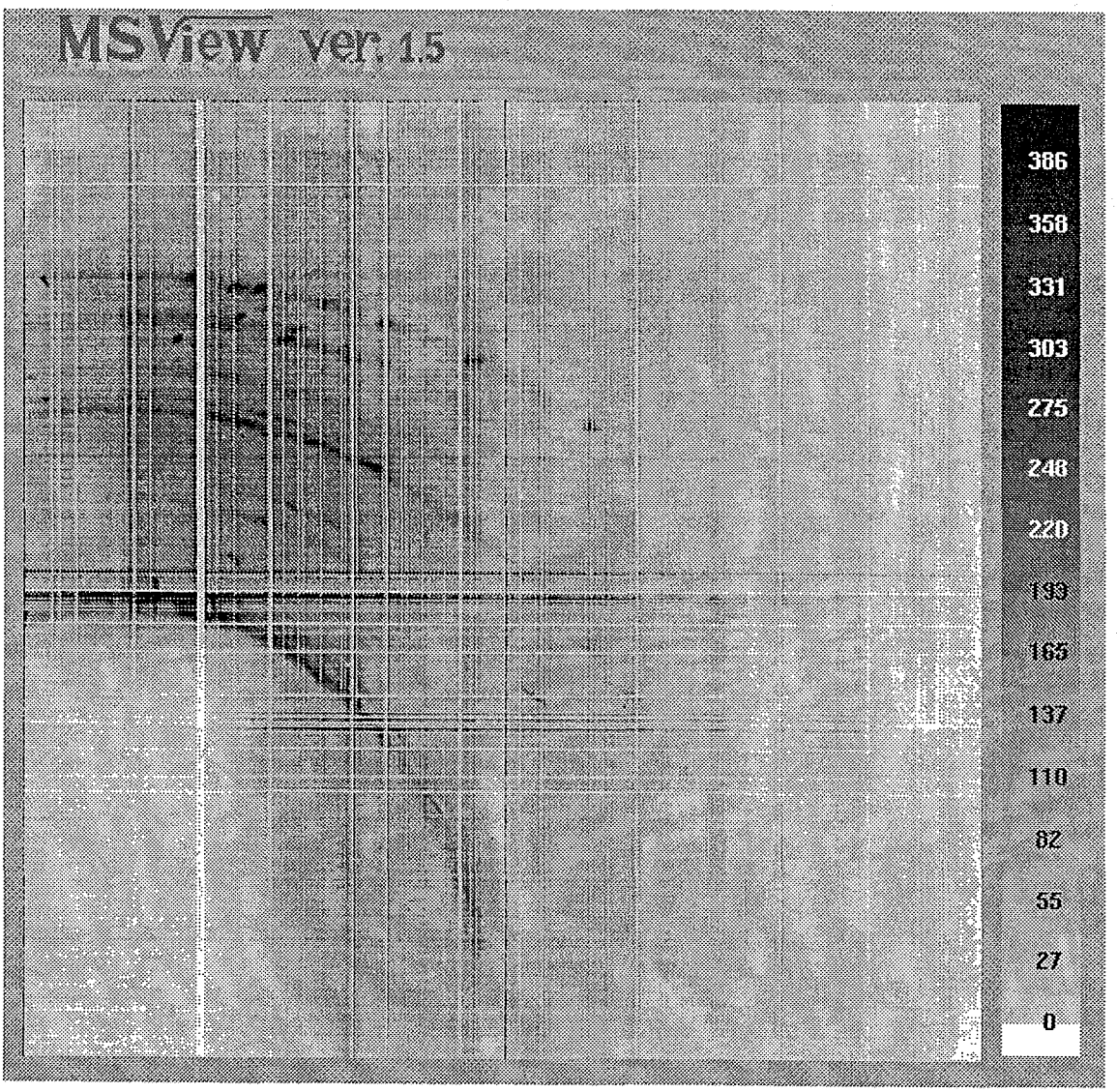

Figure 6.7: X-ray diffraction image of powder $VO(acac)_2$ with 10cm square MSGC. The vertical stripes are due to the discharged strips, and the horizontal stripes are due to the instabilities of the readout electronics.

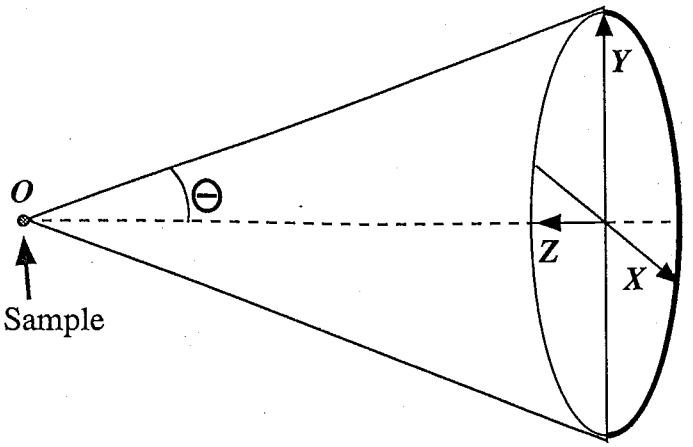

Figure 6.8: Diffraction cone and definition of XYZ systems.

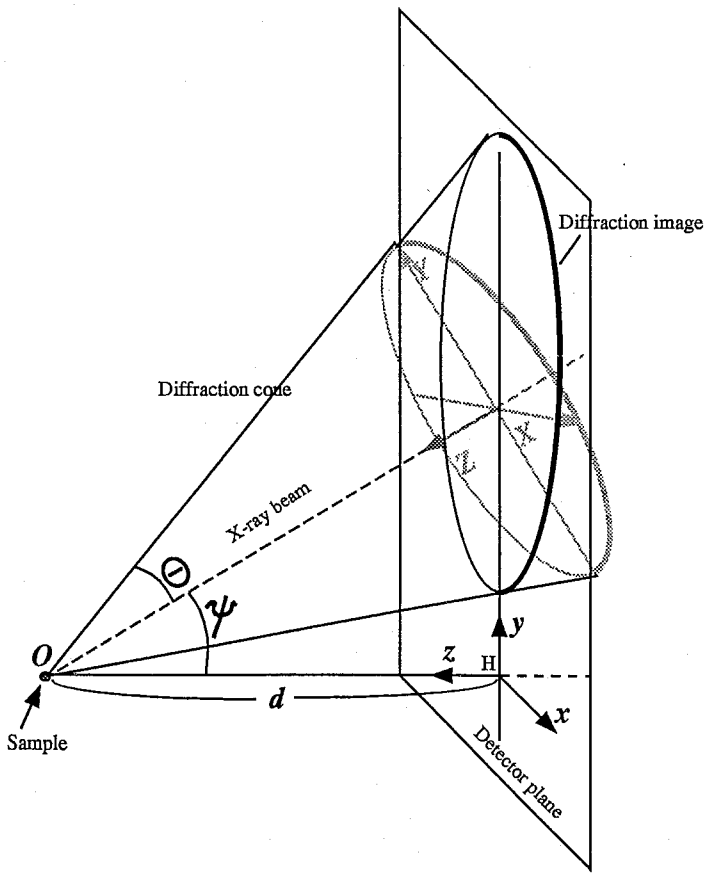

Figure 6.9: Slant diffraction cone and redefinition of the new xyz system.

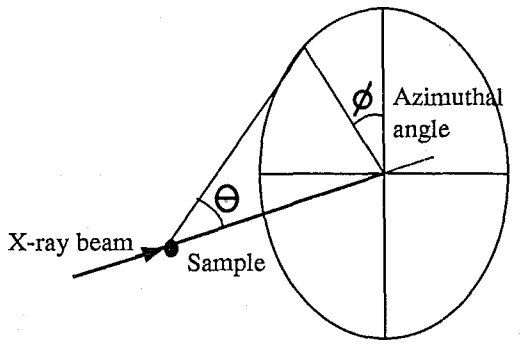

Figure 6.10: Definition of azimuthal angle on a diffraction pattern.

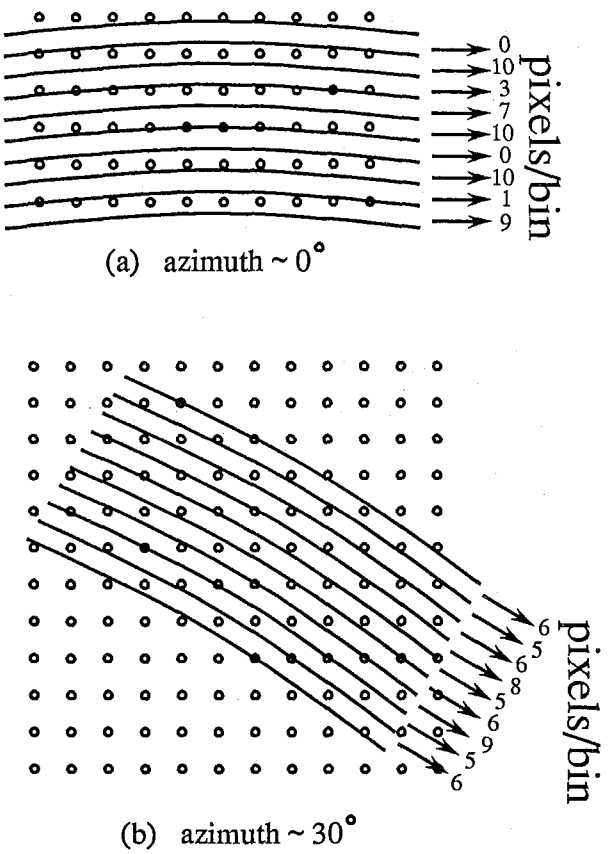

Figure 6.11: In this figure, dots mean the pixel of the MSGC, and lines mean the boundary of histograming bin corresponding to the diffraction angle. When azimuth is set near the $\frac{n\pi}{2}$, some bin will involve no pixels as shown in (a). For moderate azimuth, each bin contains almost the same number of pixels (b).

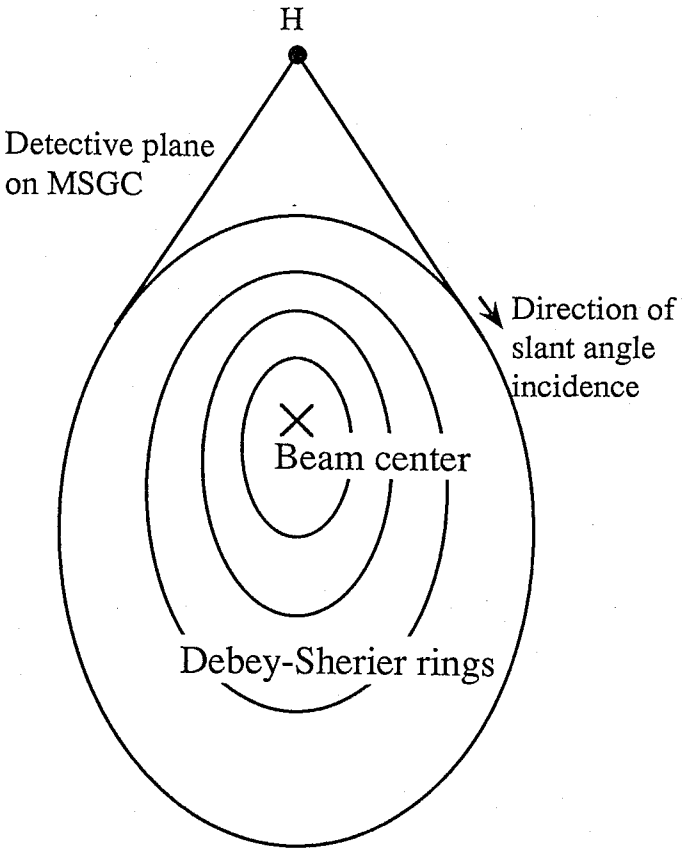

Figure 6.12: Effect of slant incidence limits the optimized azimuth angle on the MSGC.

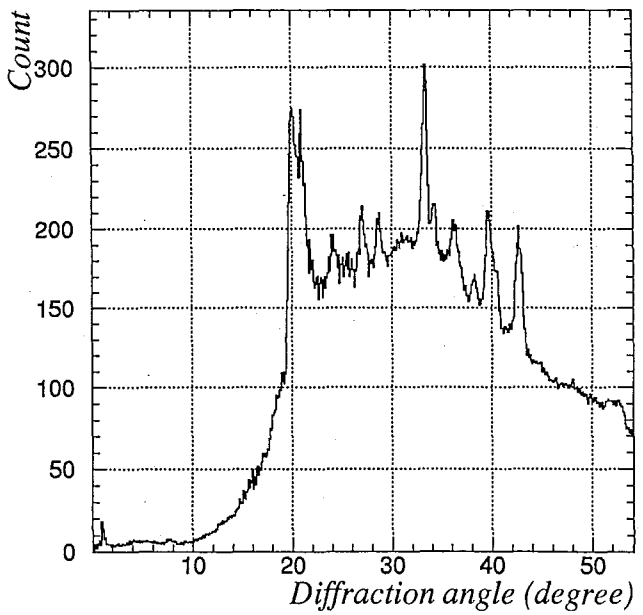

Figure 6.13: Powder X-ray diffraction pattern of $VO(acac)_2$ corresponding to the diffraction angle 2θ.

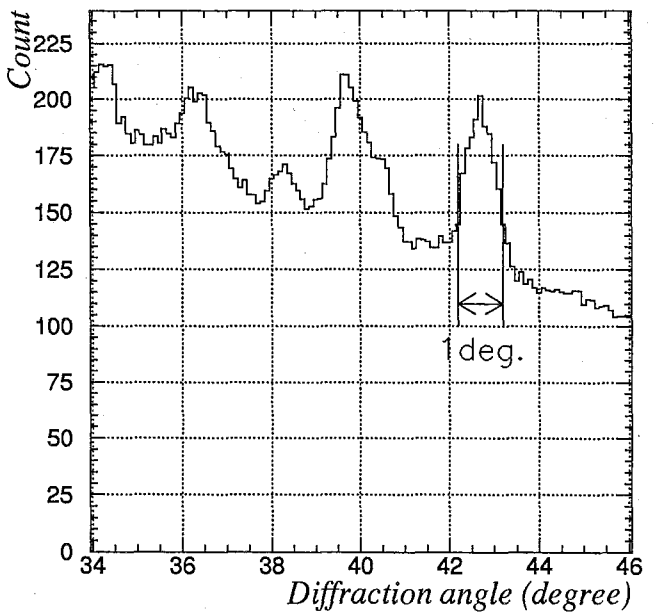

Figure 6.14: Part of powder X-ray diffraction pattern of $VO(acac)_2$ around $2\theta = 40°$.

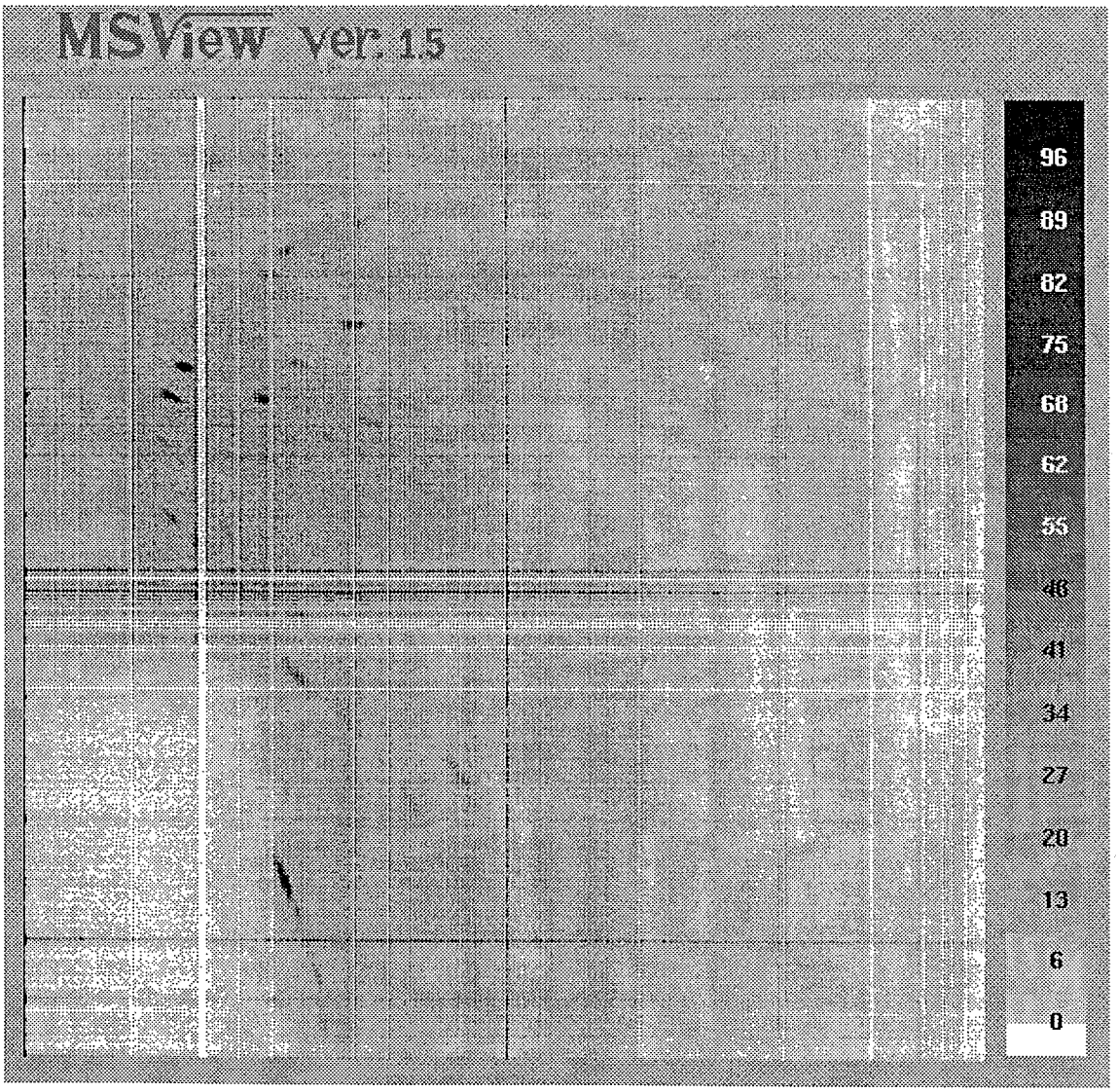

Figure 6.15: Rotation photograph of $[Bu_4N]_4[Pt_2(pop)_4]$ with 10cm square MSGC.

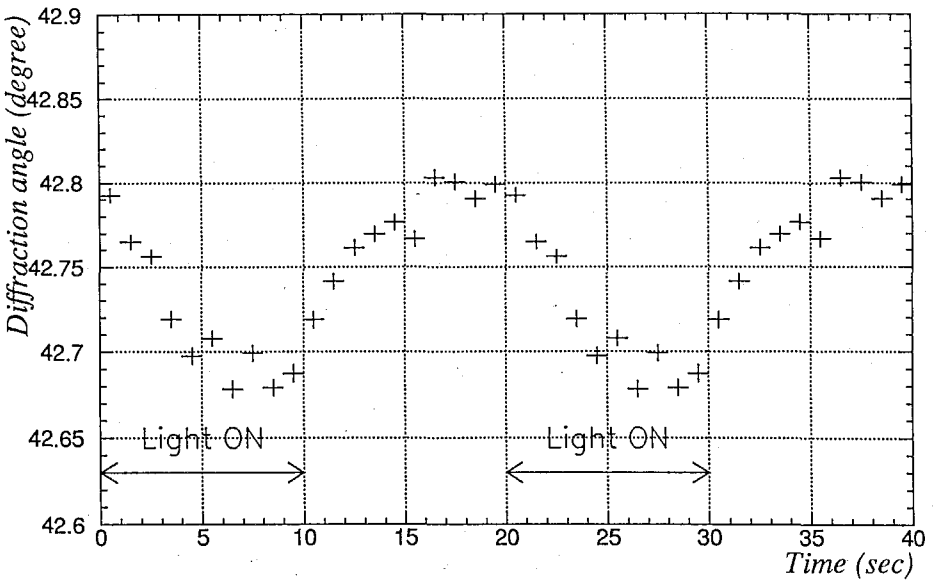

Figure 6.16: Diffraction peak movement in the photo excitation. One of the powder diffraction peaks of $VO(acac)_2$ was selected for the measurement. The data points folding in one cycle are plotted with 1 second bin after the photo irradiation. The peak shifted to small diffraction angle when the light was turned on.

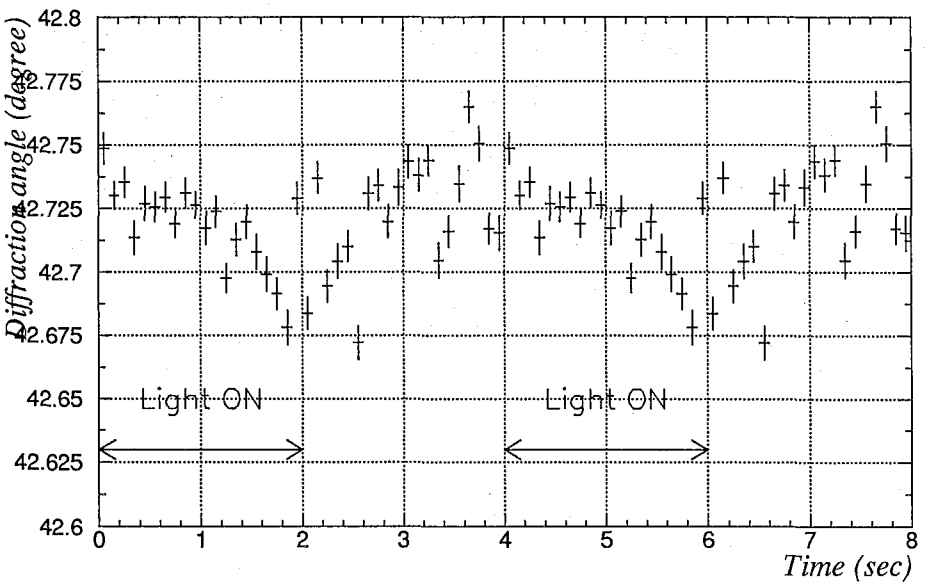

Figure 6.17: Diffraction peak movement in the photo excitation. One of powder diffraction peaks of $VO(acac)_2$ was selected for the measurement. The data points folding in one cycle are plotted with 100ms timing bin.

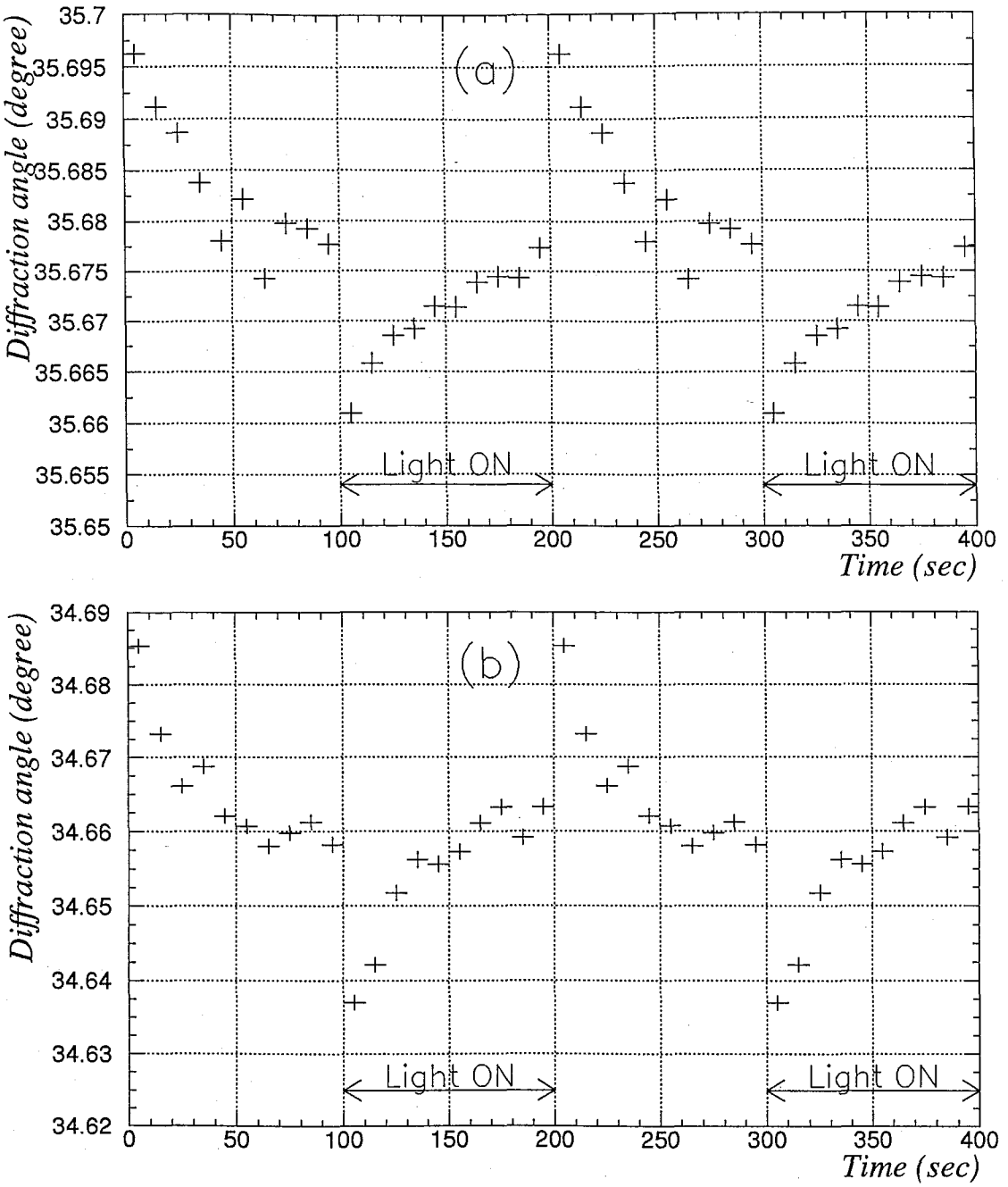

Figure 6.18: Periodical movement of the diffraction peaks in the photo excitation. Two of the diffraction spots ((a): $2\theta = 35.7°$, (b): $2\theta = 34.7°$) of a single crystal $[Bu_4N]_4[Pt_2(pop)_4]$ were selected for the measurements. The data points folding in one cycle are plotted where the 0 time means the end of the photo irradiation.

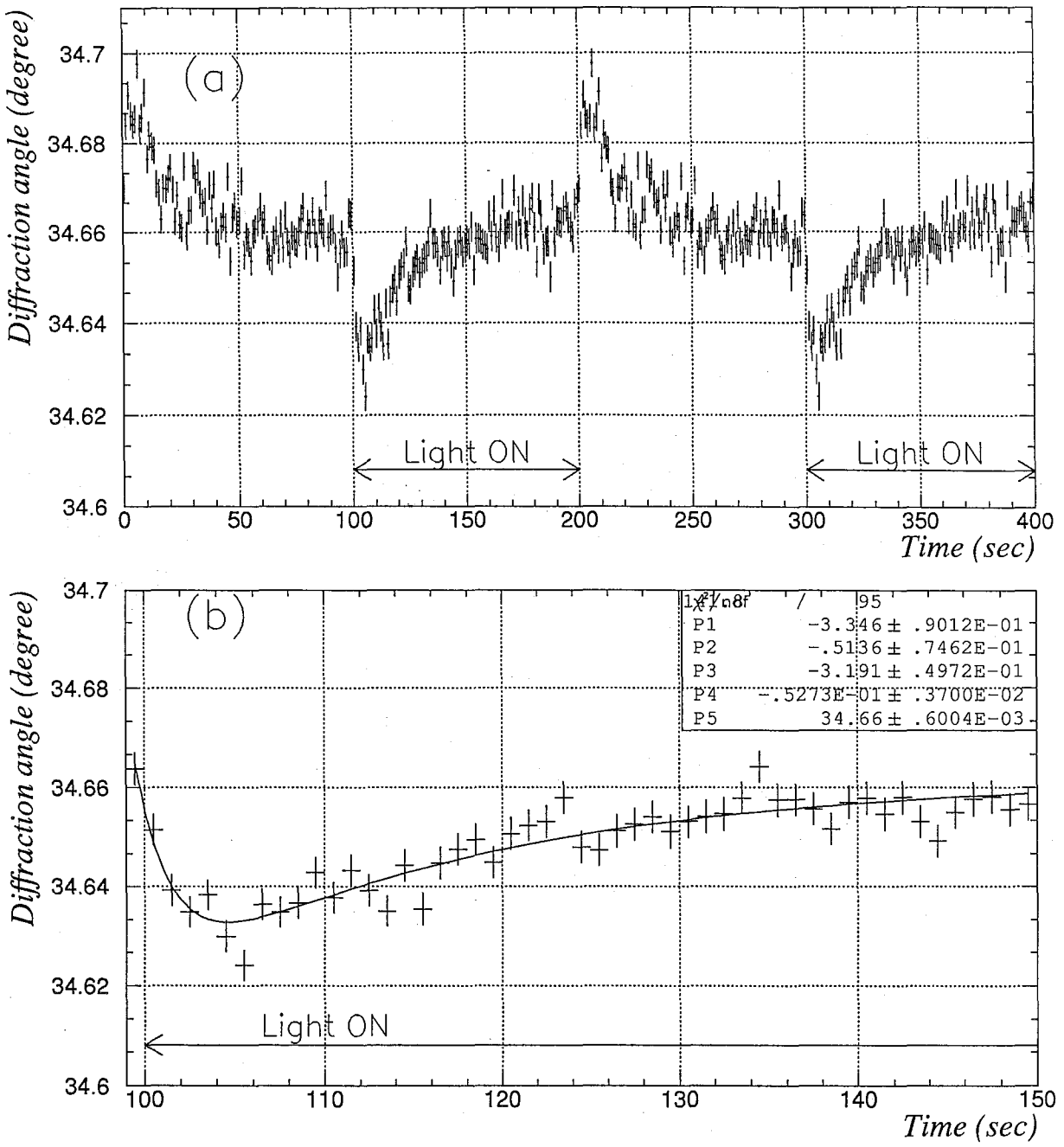

Figure 6.19: Movement of the diffraction peak in the photo excitation (0 $\sim$ 5s after the light on/off) and that in the thermal effect (5 $\sim$ 50s after the light on/off). Analyses were carried out in each 1 second after the photo irradiation using the diffraction spot of $2\theta = 34.7°$) of a single crystal $[Bu_4N]_4[Pt_2(pop)_4]$. (a) shows the data plots folding in whole one cycle, and (b) shows the enlarged plots and fitting line of (a) around the biginning of the photo irradiation.

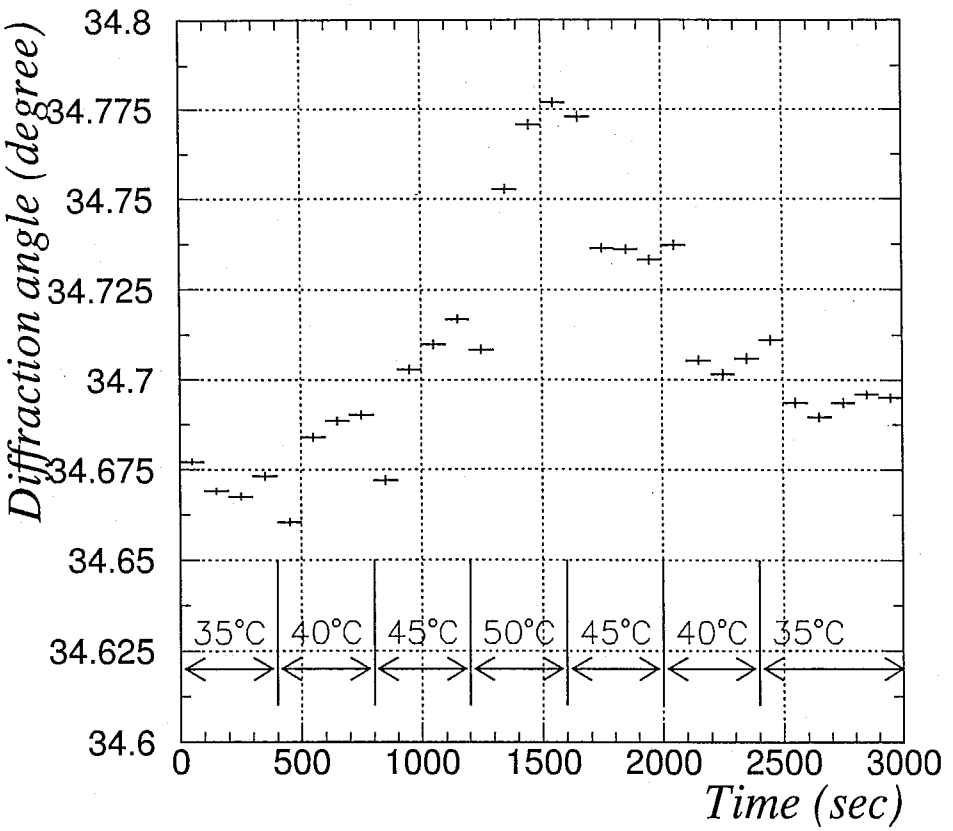

Figure 6.20: Movement of the diffraction peak by the temperature variation using the diffraction spot of $2\theta = 34.7°$ of the single crystal $[Bu_4N]_4[Pt_2(pop)_4]$.

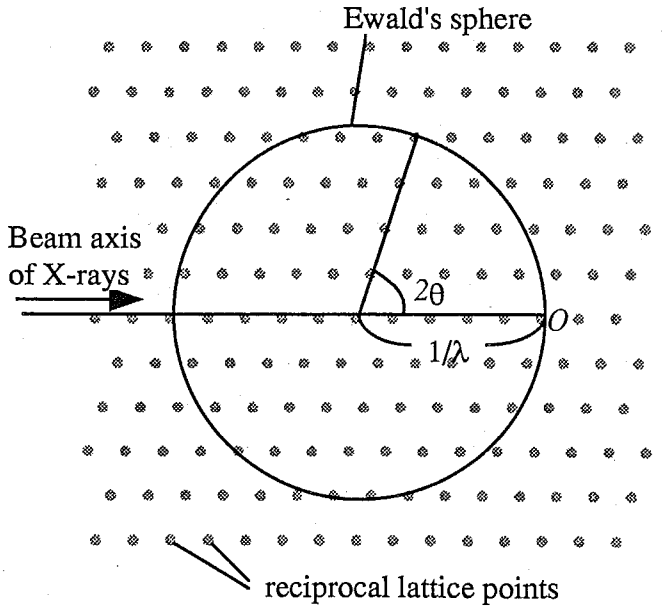

Figure 6.21: The reciprocal lattice and Ewald's sphere.

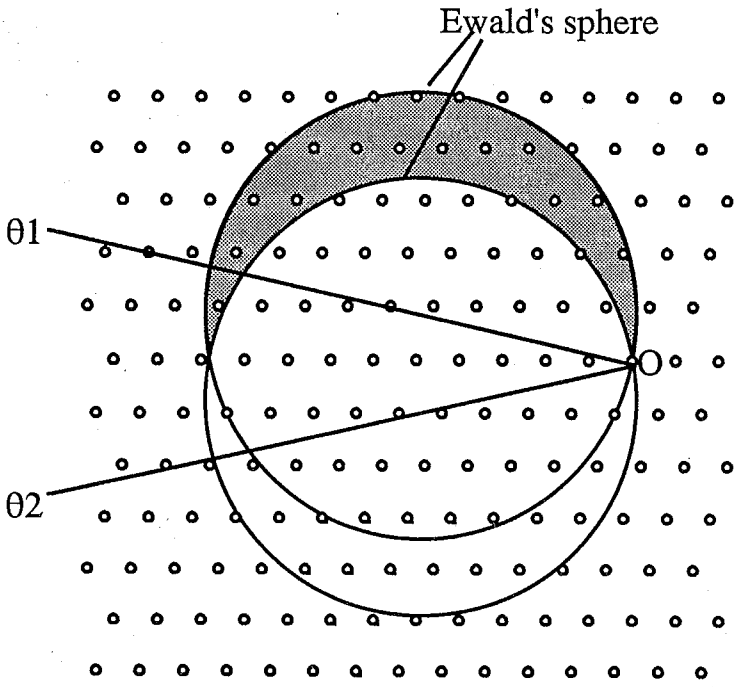

Figure 6.22: In the oscillation photograph, the image appearing on a film corresponds to the lattice points in the gray region in this figure.

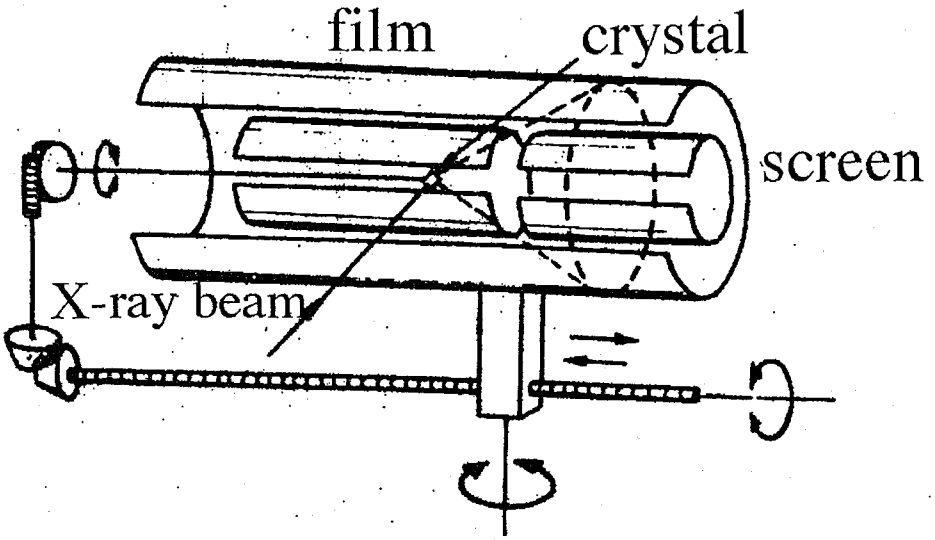

Figure 6.23: Schematic structure of Weissenberg camera. [43]

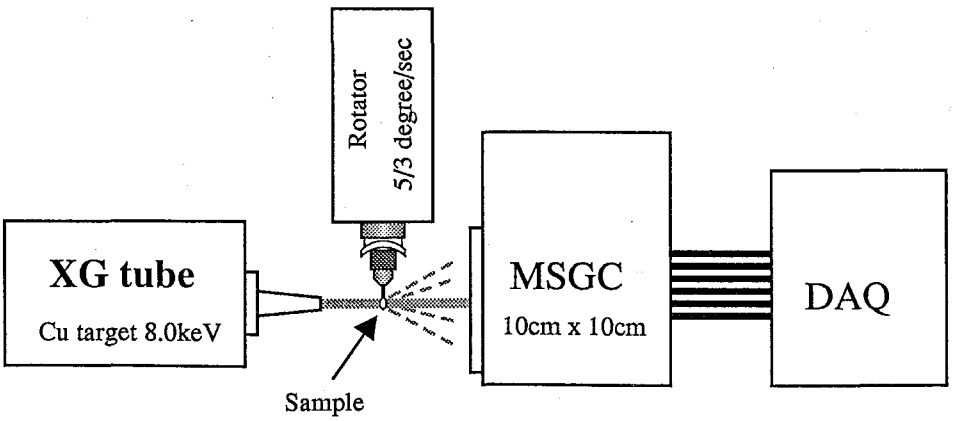

Figure 6.24: Experimental setup of the measurement with the RCP method.

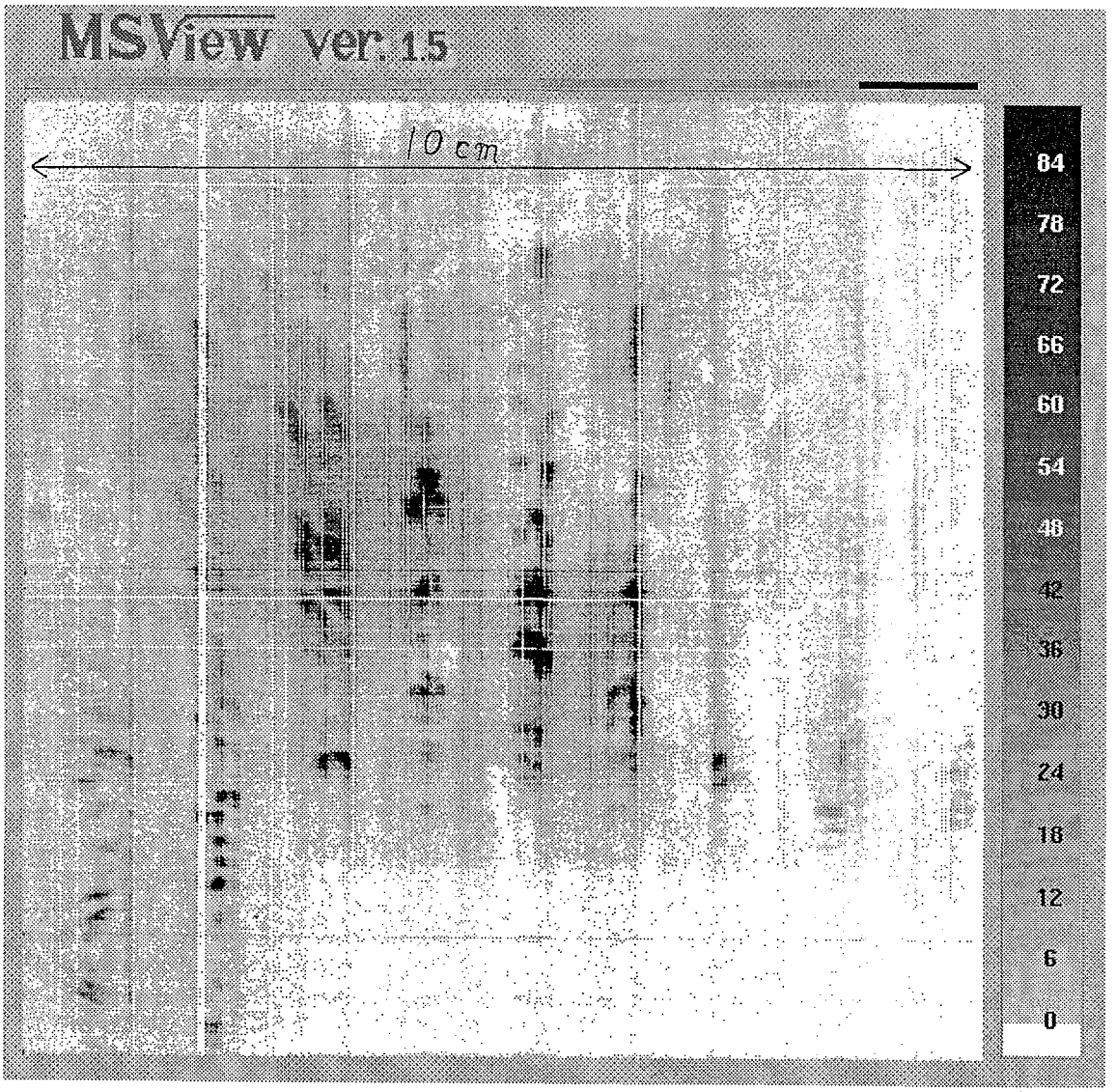

Figure 6.25: Rotational image of Phenothiazine-Benzilic acid complex obtained with the 10cm square MSGC.

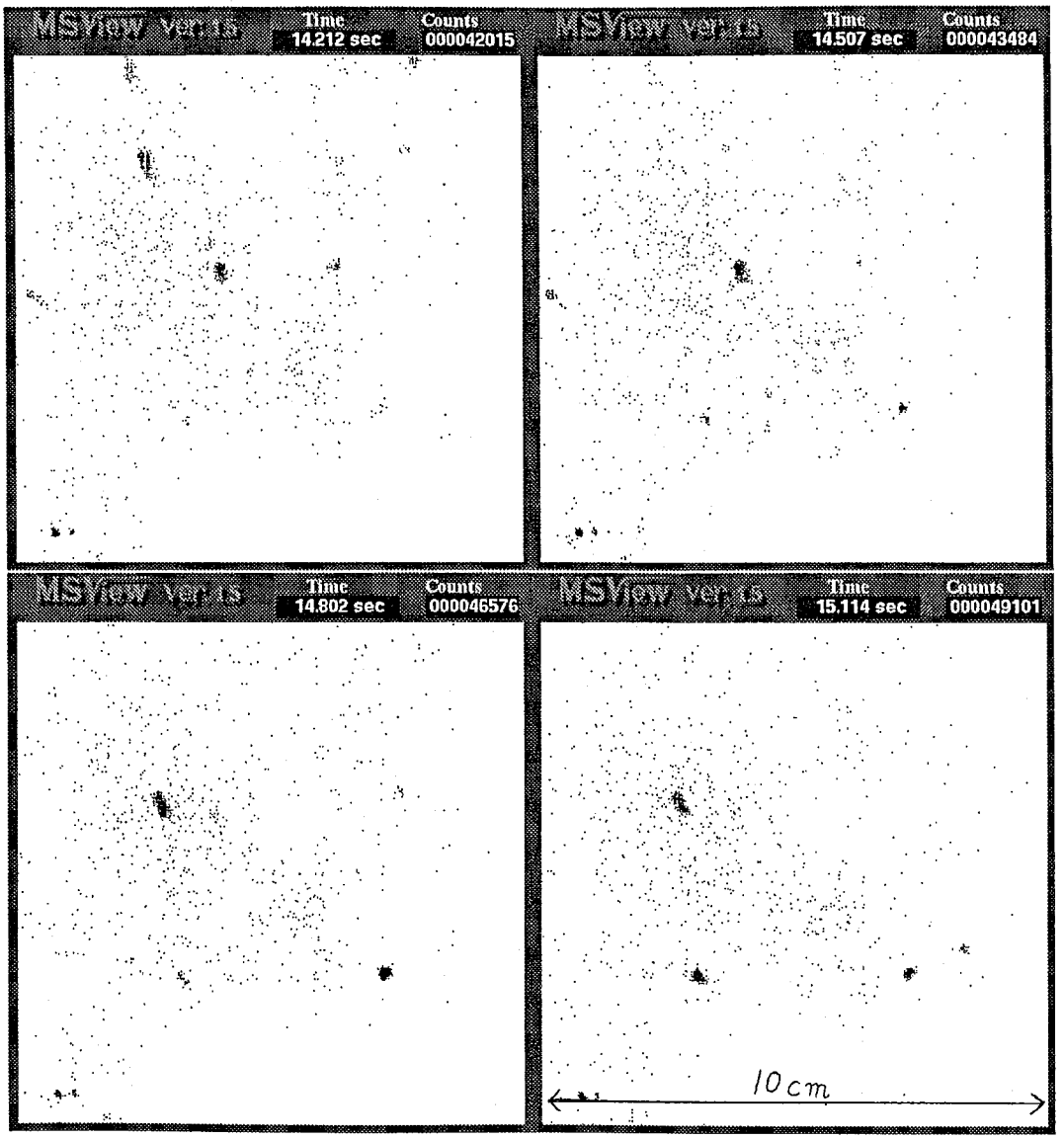

Figure 6.26: Time resolved sequential images observed every 0.3 second exposure time.

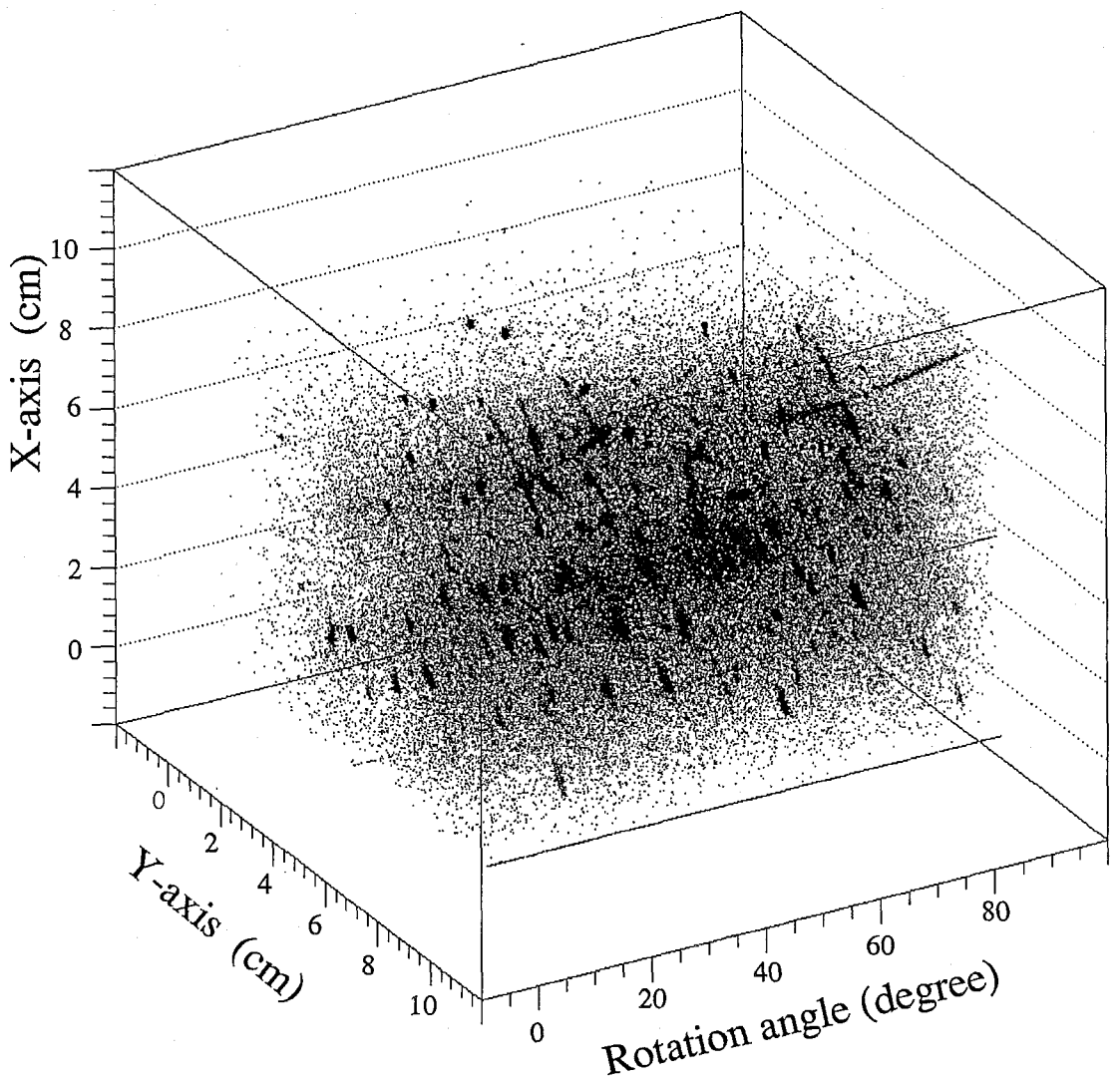

Figure 6.27: Three-dimensional image of diffraction spots in which each spot is plotted according to its two dimensional position (x, y) and the rotation angle of the crystal (ϕ) dimension.

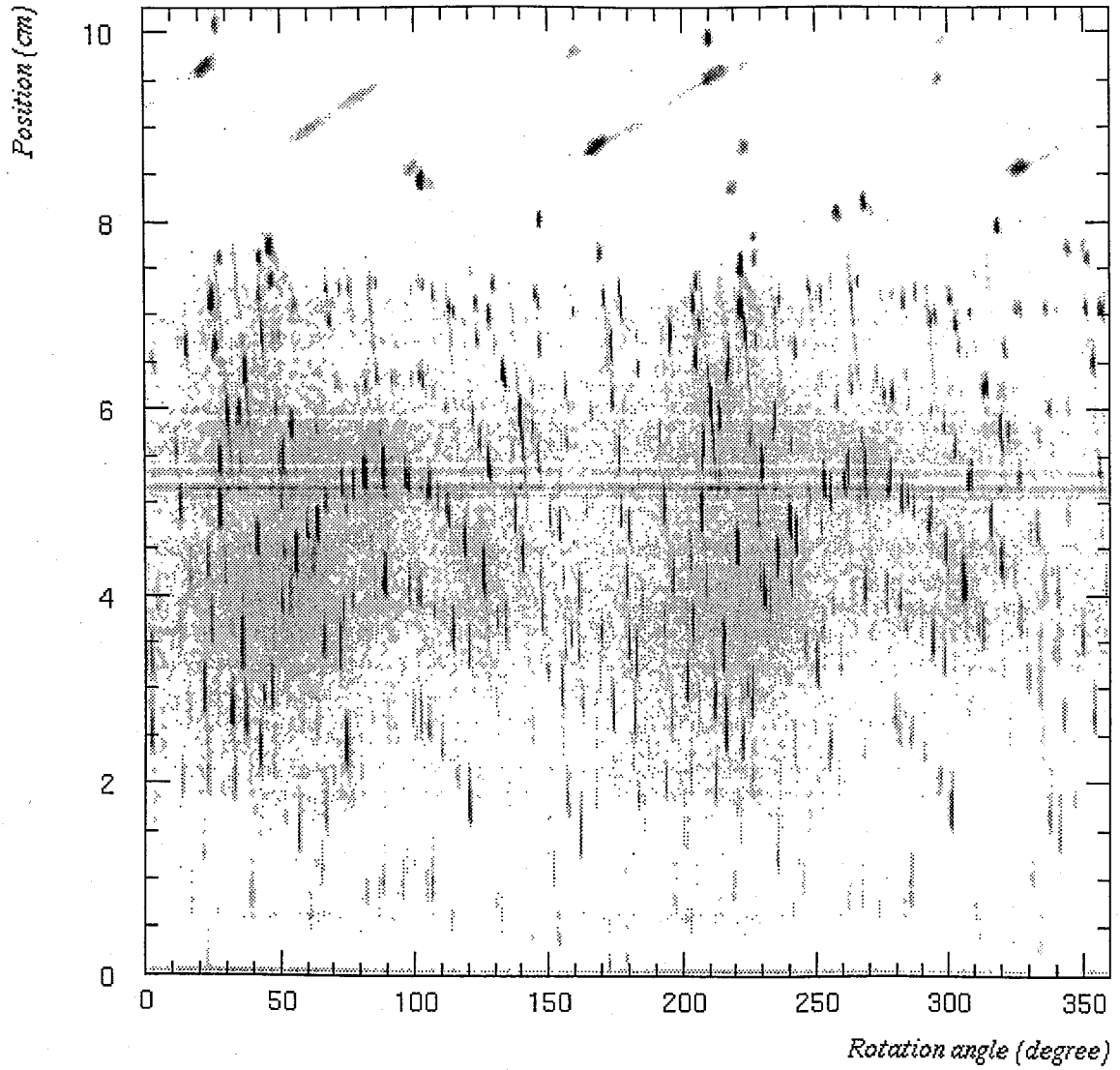

Figure 6.28: Projection of the 3-dimensional image to the $y - \phi$ plane.

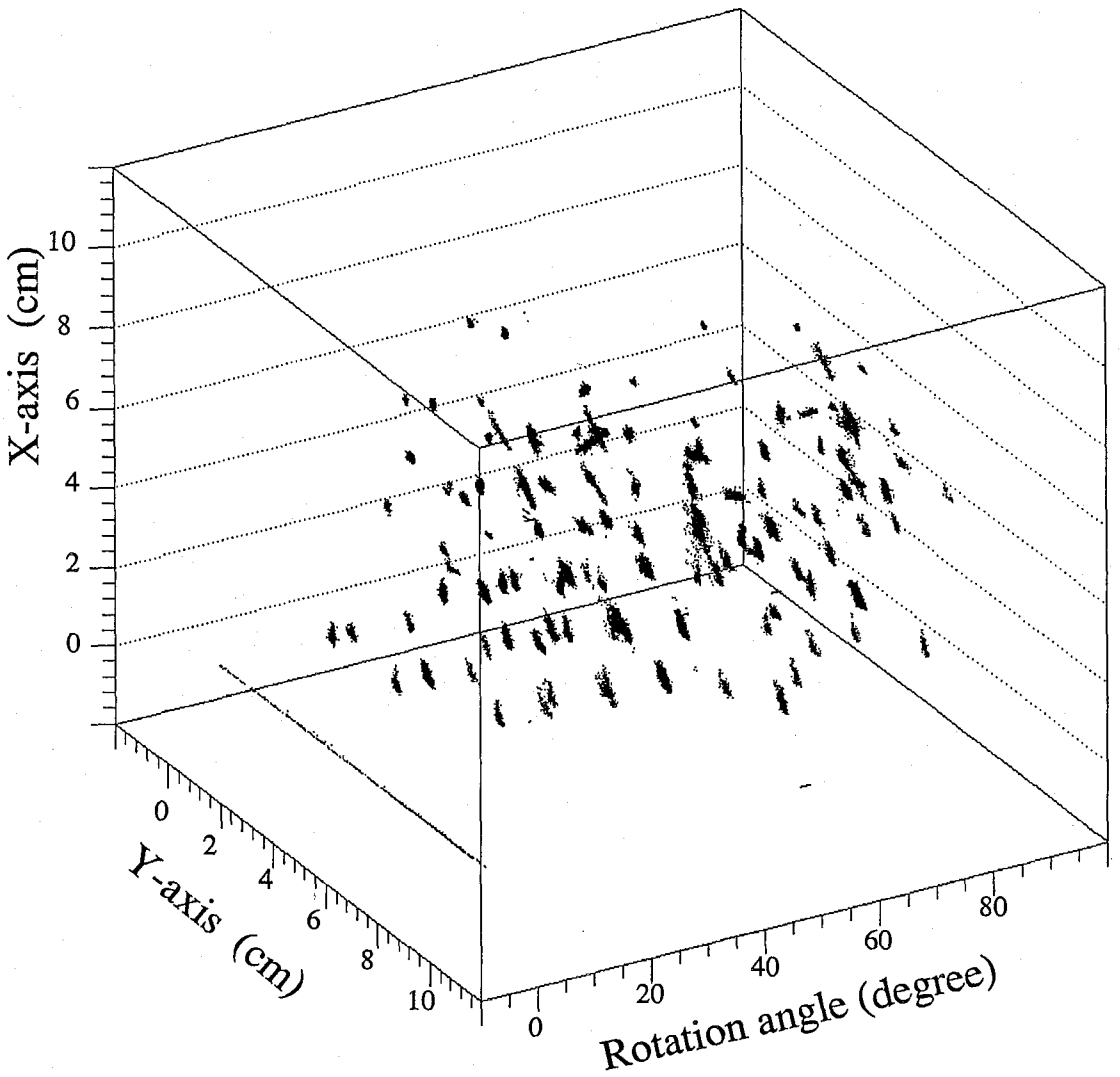

Figure 6.29: Three-dimensional image with RCP method after applying the noise reduction using the timing (ϕ axis) information.

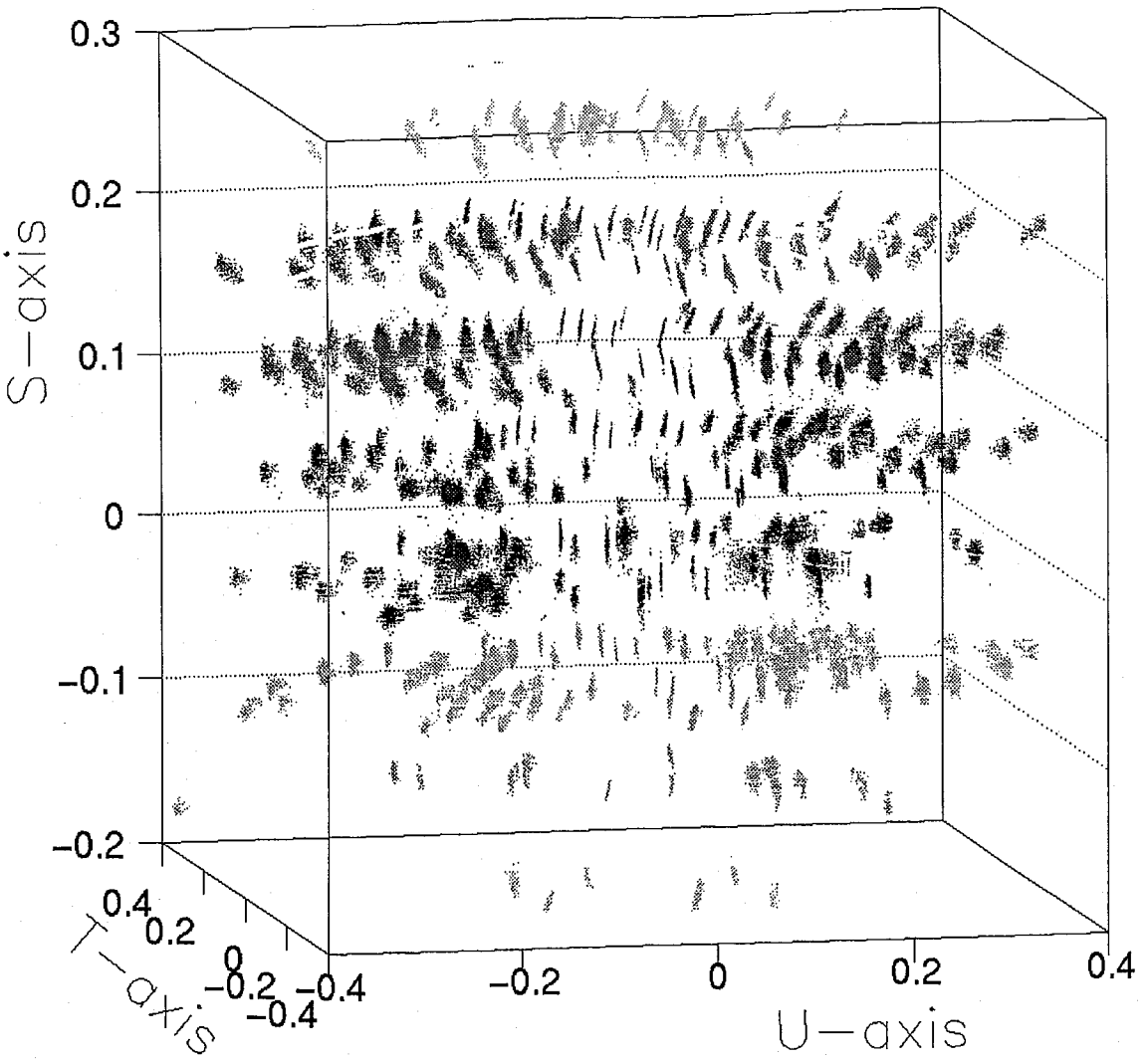

Figure 6.30: Directly reconstructed reciprocal lattice using the RCP method. The s, t, u axes are defined in the text.

Chapter 7

Conclusion

A two-dimensional MSGC and a fast data acquisition system have been developed, and using this MSGC system, we have successfully carried out time resolved X-ray imaging experiments. The narrow strip spacing of 200μm between anode electrodes has given rise to the fine position resolution of 100μm, and the capability for high counting rate of 2×10^7 were realized. Our MSGCs have a thin substrate made of polyimide which is realized by the MCM technology, and this organic substrate has made it possible to make a large area MSGC having 10cm×10cm detection area. Since the MSGC is a differential type detector, it can provide not only time resolved image with fine position resolution and a large dynamic range, but also a fairly new type of imaging analysis method utilizing other information such as fine-timing and energy. These new type of imaging would give a new approach in an X-ray imaging analysis.

There have been two serious problems for MSGC to be overcome. One of them is the gain variation due to the charge up on the substrate, and the other is a discharge between electrodes. The former problem has been solved by the tuning of the operation voltage and the substrate thickness which were determined through simulation. The latter one has been improved by the passivation on the cathode. Although the discharge problems have not been overcome completely yet, several attempts are being carried out, such as the intermediate multiplier in the gas volume and the improving the material of electrodes with high melting point; the discharge problem will be solved soon.

In addition, we stress that this detector system is completely electrical controlled by computer, where an electrical system means not only that the data are completely electrically transferred to computers, but also that all the components of the MSGC system

are made using IC or LSI technology. MSGC itself is made using high density printed board technology developed for direct mounting of a bare LSI. All electrical elements of the MSGC readout system consists of commercially available LSI chips. Fast amplifiers and comparators attached to the MSGC amp-card (MQS104 and MVL407 of LeCroy respectively, both 4ch. in one chip), and the ECL-TTL transfer chips in the PEMs are the main elements of the readout system. The 1024 of signal lines are fully processed by the CPLDs which have a lot of I/O pins and customizable logical circuits. The newly developed data synchronizing and encoding system has made it possible to process X-ray events up to 3.2Mcps.

In order to study the performance of time resolved property, two experiments on X-ray crystallography was carried out. The first one is the measurement on the light excitation of crystal using time resolved X-ray diffraction method. The variation of the structure of crystal was measured by observing some typical diffraction spot, and the influence from thermal effect was rejected by timing analysis for $[Bu_4N]_4[Pt_2(pop)_4]$ sample. Then the timing constant for light excitation of $[Bu_4N]_4[Pt_2(pop)_4]$ was obtained to be 1.9 seconds, which maybe the first measurement of the time constant.

Second is the first attempt to the crystal rotation continuous photograph (RCP) method. The three dimensions of data (two of them are positions in the image, the other is the timing) allow us to distinguish the diffraction peaks from the noises very clearly, and to construct the three-dimensional reciprocal lattice image by a simple transformation of coordinate systems as mentioned in section 6.2. The RCP method will provide a new analysis method for the crystallography, reducing the experimental time dramatically. Only a few minutes will be required for a crystal structure analysis while the existing methods take about one day.

MSGC will provide new innovative approaches to imaging analysis methods using X-ray, charged particles, and neutrons, opening versatile fields of application.

Bibliography

[1] A. Oed. Position-sensitive detector with microstrip anode for electron multiplication with gases. *Nucl. Instrum. Meth.*, Vol. A263, p. 351, 1988.

[2] A. Barr, B. Boimska, R. Bouclier, M. Capeáns, W. Dominik, G. Manzin, G. Millon, M. Hoch, L. Ropelewski, F. Sauli, and A. Sharma. Operation of the high rate microstrip gas chambers. CERN-PPE/96-200, October 1996.

[3] F. Sauli. Development of high rate msgcs: Overview of results from rd-28. CERN-PPE/97-19, January 1997.

[4] B.D. Ramsey, J.A. Apple, R.A. Austin, K.L. Dietz, T. Minamitani, J.J. Kolodziejczak, and M.C. Weisskopf. A large-area microstrip-gas-counter for x-ray astronomy. *Nucl. Instrum. Meth.*, Vol. A383, p. 424, 1996.

[5] N. Vellettaz, J.E. Assaf, and A. Oed. Two-dimensional gaseous microstrip detector for thermal neutrons. *Nucl. Instrum. Meth.*, Vol. A392, p. 73, 1997.

[6] A. Barr, R. Bouclier, M. Capeáns, G. Della Mea M. Hoch, G. Millon, G. Manzin, L. Ropelewski, and F. Sauli. Recent advances in the construction and testing of msgcs. *Nucl. Instrum. Meth.*, Vol. A392, p. 99, 1997.

[7] F. Angelini, R. Bellazzini, B. Bozzo, A. Brez, M.M. Massai, R. Raffo, G. Spandre, M. Spezziga, and A. Toropin. Development of a very large area microstrip gas chamber for the cms central tracking system, 1994. INFN-Pisa/AE94/011.

[8] O. Bouhali, F. Udo, W. Van Dooninck, L. Van Lancker, C. Vander Velde, P. Vanlaer, and V. Zhoukov. Operation of micro strip gas counters with ne-dme gas mixtures. *Nucl. Instrum. Meth.*, Vol. A378, p. 432, 1996.

[9] T. Tamura, H. Sugeno, H. Sakurai, M. Noma, S. Gunji, and P. Gertenbort. An application of microstrip gas proportional counter for a x-ray polarimeter. In *Proceedings of IEEE Nuclear Science Symposium and Medical Imaging Conference, Sanfrancisco*, 1995.

[10] E.K.E. Gerndt, B.A. Knapp, I.P.J. Shipsey, and P. Geltenbort. Properties of a moscow glass micro strip gas chamber. *Nucl. Instrum. Meth.*, Vol. A388, p. 42, 1997.

[11] N. Amos, L. Cremaldi, G. Finocchiaro, B. Gobbi, K.K. Ng, V. Manzella, V. Peskov, S. Rajagopalan, P. Rubinov, D. Schamberger, G. Sellberg, J. Steffens, R. Tilden, P. Wang, and Y. Yu. Position resolution of msgcs with cathode readout. *Nucl. Instrum. Meth.*, Vol. A384, p. 342, 1997.

[12] A. Oed, P. Convert, M. Berneron, H. Junk, C. Budtz-Jørgensen, M.M. Madsen, P. Jonasson, and H.W. Schnopper. A new position-sensitive proportional counter with microstrip anode for neutron detection. *Nucl. Instrum. Meth.*, Vol. A284, p. 223, 1989.

[13] A. Oed and P. Geltenbort. Substratum and layout parameters for microstrip anodes in gas detectors. *Nucl. Instrum. Meth.*, Vol. A310, p. 95, 1991.

[14] F. Hartjes, B. Hendeiksen, and D. Udo. A prototype microstrip gas detector. *Nucl. Instrum. Meth.*, Vol. A289, p. 384, 1990.

[15] F. Angelini, R. Bellazzini, A. Brez, M.M. Massai, G. Spandre, and M.R. Torquati. A microstrip gas avalanche chamber with two-dimensional readout. *Nucl. Instrum. Meth.*, Vol. A283, p. 755, 1989.

[16] H. Stahl, U. Werthenbach, and G. Zech. First steps towards a foil microstrip chamber. *Nucl. Instrum. Meth.*, Vol. 297, p. 95, 1990.

[17] R. Bouclier, JJ. Florent, J. Gaudaen, F. Sauli, and L. Shekhman. Development of microstrip gas chambers on thin plastic supports. *Nucl. Instrum. Meth.*, Vol. A315, p. 521, 1992.

[18] T. Nagae, T. Tanimori, T. Kobayashi, and T. Miyagi. Development of microstrip gas chambers with multi-chip technology. *Nucl. Instrum. Meth.*, Vol. A323, p. 236, 1992.

[19] T. Tanimori, S. Minami, T. Nagae, T. Takahashi, and T. Miyagi. Development of microstrip gas chamber and application to imaging gamma-ray detector. INS-939, Jul 1992. 10pp Presented at SPIE 1992 Int. Symp. on Optical Applied Science and Engineering Gamma Ray Detectors.

[20] F. Angelini, R. Bellazzini, A. Brez, M.M. Massai, A. Perret, G. Spandre, and M.R. Torquati. A microstrip gas chamber with true two-dimensional and pixel readout. *Nucl. Instrum. Meth.*, Vol. A323, p. 229, 1992.

[21] Toru Tanimori, Atsuhiko Ochi, Seiji Minami, and Tomofumi Nagae. Development of an imaging microstrip gas chamber with a 5cm $\times$ 5cm area based on multi-chip module technology. *Nucl. Instrum. Meth.*, Vol. A381, p. 280, 1996.

[22] R. Bouclier, JJ. Florent, J. Gaudaen, G. Millon, A. Pasta, L. Ropelewski, and F. Sauli. High flux operation of microstrip gas chambers on glass and plastic supports. *Nucl. Instrum. Meth.*, Vol. A323, p. 240, 1992.

[23] F. Angelini, R. Bellazzini, L. Bosisio, A. BREZ, M.M. Massai, G. Spandre, and M.R. Torquati. A microstrip gas chamber on a silicon substrate. *Nucl. Instrum. Meth.*, Vol. A314, p. 450, 1989.

[24] R. Fang, W. Geist, J.M. Brom, A. Bergdolt, and J.L. Riester. Gain stability of microstrip gas chambers with high resistivity substrates. *Nucl. Instrum. Meth.*, Vol. A378, p. 439, 1996.

[25] R. Bellazzini, A. Brez, L. Latronico, N. Lumb, M.M. Massai, R. Raffo, G. Spandre, and M.A. Spezziga. Substrate-less, spark-free micro-strip gas counters. In *Proceedings of the VII Pisa Meeting on Advance Detectors 'Frontier Detectors for Frontier Physics' Isola d'Elba, Italy*, 1997.

[26] V. Peskov, B.D. Ramsey, and P. Fonte. Surface streamer breakdown mechanisms in microstrip gas counters. *Nucl. Instrum. Meth.*, Vol. A392, p. 89, 1997.

[27] R. Bouclier, M. Capeáns, W. Dominik, M. Hoch, J-C. Labbé, G. Millon, L. Ropelewski, F. Sauli, and A. Sharma. The gas electron multiplier (gem). CERN-PPE/96-177, November 1996.

[28] S. Aoki. Development of the msgc using capillary plate as a intermediate gas multiplier. Master's thesis, Tokyo Institute of Technology, 1998.

[29] H. Sakurai, T. Tamura, S. Gunji, and M. Noma. A new type of proportional counter using a capillary plate. *Nucl. Instrum. Meth.*, Vol. A, , 1995.

[30] A. Ochi, S. Aoki, Y. Nishi, and T. Tanimori. Development of imaging microstrip gas chambers and measurement of the polarization of x-rays. *Nucl. Instrum. Meth.*, Vol. A392, p. 124, 1997.

[31] G. Charpak, R. Bouclier, T. Bressani, J. Favier, and Č. Zupančič. The use of multiwire propotional counters to select and localize charged particles. *Nucl. Instrum. Meth.*, Vol. 62, p. 235, 1968.

[32] G.A. Erskine. 0. *Nucl. Instrum. Meth.*, Vol. 105, p. 565, 1972.

[33] S.A. Korff. Electrons and nuclear counters, 1946. Van Nostrand, New York.

[34] G. Schultz, G. Charpak, and F. Sauli. Mobilities of positive ions in some gas mixtures used in proportional and drift chambers. *Rev. Physique Appliquée*, Vol. 12, p. 67, 1977.

[35] F.Sauli. Principles of operation of multiwire proportional and drift chambers, 1977. CERN Report 77-09.

[36] G.D. Minakov, Yu.N. Pestov, V.S. Prokopenko, and L.I. Shekhtman. Performance of gas microstrip chambers on glass with ionic and electronic conductivity. *Nucl. Instrum. Meth.*, Vol. A326, p. 566, 1993.

[37] G. Cicognani, B. Guerard, and A. Oed. Performance of msgc on diamond-coated glass. *Nucl. Instrum. Meth.*, Vol. A392, p. 115, 1997.

[38] F. Angelini, R. Bellazzini, A. Brez, M.M. Massai, R. Raffo, G. Spandre, and M.A. Spezziga. Operation of msgcs with gold strips built on surface-treated thin glasses. *Nucl. Instrum. Meth.*, Vol. A382, p. 461, 1996.

[39] A. Ochi. X-ray area detecting with two dimensional msgc. Master's thesis, Tokyo Institute of Technology, 1995.

[40] Takashi Ikagawa, Toshihiko Okumura, Takuhiro Otsuka, and Youkoh Kaizu. Distortion of the unit cell of platinum(ii) complexes under light irradiation. *Chem. Let.*, p. 829, 1997.

[41] H. Hauptman and J. Karie. A geometric approach to the crystal structure problem. *Acta Cryst.*, Vol. 3, p. 478, 1950.

[42] Toru Tanimori, Shunsuke Aoki, Yuji Nishi, and Atsuhiko Ochi. Development of microstrip gas chamber as a time-resolved area detector. to be published in J. Synchrotron Radiation.

[43] Masanori Katoh. X線で何がわかるか (Japanese). Uchida Rokakuho CO., LTD., 1990.

Acknowledgments

First of all, I am most grateful to Professor Toru Tanimori who is my supervisor. He started a development of this microstrip detector, and continued to lead our project vigorously. He often showed appropriate solutions to overcome difficulties which help me out of confusion. I truly appreciate his continuous support for me to write this thesis.

I am really grateful to Professor Yasushi Watanabe for the guidance and encouragement in this work. I sincerely thank to Dr. Kenji Kaneyuki and all the members of high-energy physics group in Tokyo Institute of technology for kind support of this experiment. Especially, I wish to thank Messrs. Yuji Nishi, Yasuro Nishi, Shunsuke Aoki and Daisuke Toya. They are the members of detector subgroup and have been always together to do experiments. I also thank Seiji Minami who collaborated in this project in early development and showed many useful suggestions.

I sincerely thank the members of Ohashi group and Kaizu group in department of chemistry in Tokyo Inst. of Tech. I express my appreciation to Professor Yuji Ohashi for giving us the very interesting theme in chemistry using our detector, and provided us the facilities and experimental space. I also wish to thank Dr. H. Uekusa and K. Sawada for their suggestions and discussions on the crystallography and contribution in our experiment at the KEK-PF. I appreciate Dr. T. Ikagawa for giving me his sample crystal and for his special knowledge on the crystallography.

I also thank to the all the member of Structural Biophysics Laboratory in RIKEN. I show my gratitude to Dr. T. Ueki for giving me opportunities of using the synchrotron radiation beam-line at SPring-8 and for supporting many facilities. I am grateful to Dr. T. Fujisawa for experimental support in synchrotron radiation beam-line and for providing me interesting subjects in structural biophysics.

I appreciate all the members of the detector group in SPring-8. I wish to thank to

Dr. M. Suzuki for his suggestions on the gas selection, and I am greatly obliged to Dr. H. Toyokawa and K. Satoh for their technical support, many discussions and contribution to our collaborated experiments.

I wish to express appreciation to Professor T. Takahashi, Dr. Y. Ueda, and Dr. K. Okada in the ISAS X-ray astronomy group for contribution to our experiment.

I appreciate Dr. P. Gertenbort in ILL for helpful discussions, and Dr. K. Itoh in KEK-PF for experimental support. I also thank to Dr. A. Kawachi and Dr. M. Aoki for helpful suggestion about writing this thesis.

I am also grateful to all the staff in VLSI center in Tokyo Inst. of Tech. for providing me many of circuit design tools and for introducing me how to use them. The design of fast data acquisition system was successively completed by the help of this center.

I am indebted to the staff of Toshiba Co. Ltd., Amsc Co. Ltd., Rin-ei Seiki K.K., and other companies for responding our hard requirements.

This work was supported by CREST (Core Research for Evolutional Science and Technology on Japan Science and Technology Corp.), RIKEN (The Institute of Physical and Chemical Research) and JSPS Research Fellowships for Young Scientists, to which I am very grateful.